Fluid Flow Effects on Micro Cryogenic Coolers with Mixed Refrigerant

by

Ryan Lewis

B.A. Physics, Whitman College

M.S. Mechanical Engineering, University of Colorado at Boulder

A thesis submitted to the

Faculty of the Graduate School of the

University of Colorado in partial fulfillment

of the requirements for the degree of

Doctor of Philosophy

Department of Mechanical Engineering

2012

This thesis entitled:

Testing and Analysis of Mirco Cryogenic Coolers with Mixed Refrigerant

written by Ryan Lewis

has been approved for the Department of Mechanical Engineering

_____

Y.C. Lee

_____

Ray Radebaugh

Date_____

The final copy of this thesis has been examined by the signatories, and we find that both the content and the form meet acceptable presentation standards of scholarly work in the above mentioned discipline.

Ryan Lewis (Ph.D., Mechanical Engineering, 2012)

Fluid Flow Effects on Micro Cryogenic Coolers with Mixed Refrigerant

Thesis directed by Professor Y.C. Lee

Abstract

A number of small electronic devices benefit from micro-scale low temperature operation. Recently at the University of Colorado at Boulder and the National Institute of Standards and Technology, we have developed micro cryogenic coolers that a low-pressure, mixed-refrigerant Joule-Thomson cycle. Our devices utilize pressures that are a factor of 4 lower than the current state-of-the-art, and these low pressures allow us to use a miniature compressor. However we found that the mixed refrigerant does not perform as one would expect for larger cryocooler, due to the mini- and micro-channel flow regimes experienced by the micro cryocooler. In particular, the refrigerant experiences poor cooling with steady flow followed by enhanced cooling with pulsating flow.

This dissertation covers the development of the mixed-refrigerant Joule-Thomson micro cryocooler and associated micro compressor, an analysis of the steady flow regime, an analysis of the pulsing flow regime, and the development of a model both regimes which can be used to optimize refrigerant composition and performance in micro coolers. It is found that the steady flow regime corresponds to hold-up of the liquid components of the mix along the channel wall. It can be modeled according to a solution of the Navier-Stokes equations for annular flow in a mini-channel. The pulsing flow regime corresponds to the development of liquid slugs in high-pressure mini-channels that completely fill the micro-channels. Furthermore, a model of

refrigerant cooling power has been derived and verified for mixed refrigerants undergoing pulsating flow. Using this model, refrigerant mixture designs have been modified to improve cooling power and thermodynamic efficiency: a refrigerant mix designed to cool to 160 K using macro-scale mixture design rules has a specific cooling power of 237 J/mol and a thermodynamic efficiency of 8.4 % under pulsing flow, but these can be increased to 831 J/mol and 32.8 % respectively when the mix is re-designed according to the pulsating model.

The steady flow model will be valid when a refrigerant mixture experiences a laminar, annular two-phase flow pattern in mini-channels. The steady flow model will fail if the liquid phase in the mini-channel fills too much of the volume, and the flow is no longer annular; in that case the pulsating flow may apply. The pulsating flow model will apply in multi-phase multi-component systems when liquid slugs form in mini-scale channels before passing into micro-channels. The limitation of this model is the assumption that 2-phase flow can be modeled as two single-phase flows, which will not be valid if volume of the liquid slugs is not greater than the volume of the micro-channels—such as in fully integrated micro-compressor/micro-cooler systems that have no mini-scale coupling channels.

This pulsating flow regime represents a new flow regime to the field of cryogenics. Novel contributions from this work to the field of cryogenics include the experimental and theoretical analysis of heat and mass transport of mixed refrigerants at the interface of micro- and mini-channels. Such transport is a fundamental problem in the heat transfer community, and novel contributions of this work to that community include the study of refrigerant mixtures which experience two-phase flow over very large temperature ranges.

Dedication

To my parents and my wife.

Acknowledgements

First and foremost I would like to thank my wife Katie for always stay by my side through all my years in school, for providing a sounding board for all of my ideas, and for always bringing out the best in me.

I would like to express my gratitude to my advisor Professor Y.C. Lee whose guidance and support has been invaluable to my time at Colorado. And I would also like to express my thanks to Dr. Ray Radebaugh whose insights and knowledge in cryogenics have been instrumental to this process. Special thanks as well to my dissertation committee members: Professor Victor Bright, Professor Ronggui Yang, and Professor John Daily.

I would also like to thank my colleagues, collaborators, and present and past group members for their inputs, support, and discussions. From NIST, Peter Bradley, Dr. Marcia Huber, and Dr. Dan Ladner. From CU, Dr. Mu-Hong Lin, Hsin-Jui Wu, Chris DeLuca, Jill Cooper, Yunda Wang, Ben Britton, Peter Davis, Hayley Schneider, Collin Coolidge, Paul Schroeder, Miles Abar, Omar Siddiqi, Greg Rossin, Dr. Chris Oshman, Dr. Ming Kong, Dr. Li-Anne Liew.

Finally, I would like to thank the Defense Advanced Research Projects Agency (DARPA) as well as DRS Systems for providing funding for this research.

Contents

Tables

Figures

CHAPTER 1: INTRODUCTION

This chapter introduces the history of cryogenics and highlights applications that benefit from micro cryogenics. Three techniques for micro-scale cryogenic cooling are presented: Stirling coolers, thermoelectric coolers (TECs), and mixed-refrigerant Joule-Thomson (MRJT) coolers. These three coolers are compared showing that MRJT coolers have potential to be more efficient than TECs and smaller than Stirling coolers. Small MRJT coolers will experience mini- and micro-channel flow, which is discussed. Finally, previous work at the University of Colorado at boulder on MRJT microcoolers is reviewed. The chapter ends with goals of the dissertation in order to solve many issues that arise from the previous CU studies, as well as a summary of the major accomplishments of this work.

1.1 Cryogenics Introduction

Cryogenics first developed as a field in the late 19th century competition to liquefy gasses. The trend started in 1887 when Pictet and Cailletet liquefied oxygen, was advanced again when James Dewar liquefied hydrogen in 1898, and culminated with the liquefaction of helium in 1908 by Heike Kamerlingh Onnes. Using liquid helium, Onnes discovered superconductivity in pure mercury in 1911, and industrial cryogenics received a major boost. Today cryogenics are used in numerous applications, including liquefying natural gas for transport; water cryo-traps for vacuum in the 100-200 K range; vacuum cryo-pumps in the 10-20 K range, to produce ultra clean vacuum for semiconductor fabrication; superconducting magnets for levitation; liquefying oxygen and hydrogen for rocket fuel; cryosurgery; and radiation detectors, to name a few [1]. Figure 1.1 shows various applications mapped according to refrigeration power and temperature. Conventional scale cryogenic coolers typically are large in mass (kg scale), and produce cooling power on the order of 1 W. Systems which require low temperature and <100 mW in cooling

power lend themselves to micro cryogenics.

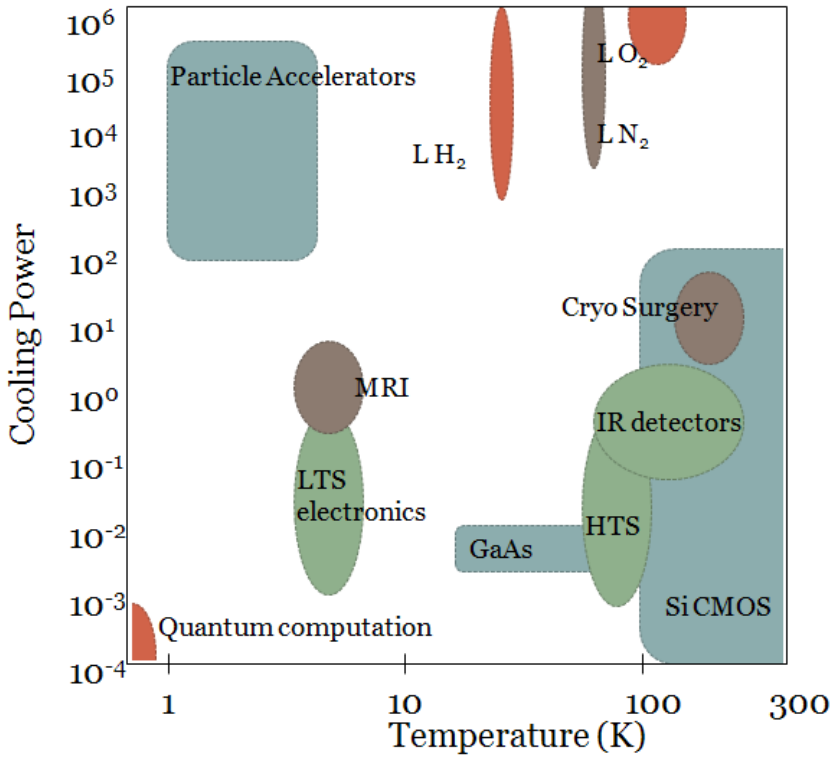

Figure 1.1: Applications of cryocoolers mapped to a refrigeration power-versus-temperature plane, adapted from [1].

1.2 Applications of Micro Cryogenics

Numerous small systems benefit from low-temperature and cryogenic application. Mechanical resonators have been shown to have increased resonance quality [2]. Small samples of biological specimens can be preserved with low temperatures [3]. At temperatures below 85 K, $YB_2Cu_3O_{7-x}$ (YBCO) experiences a superconducting state, and numerous small scale electronics devices have been developed with that material, including superconducting quantum interference devices (SQIDS) [4]. Terrahertz detectors built from YBCO are used in spectroscopic and security applications [5]. Recently such cooled millimeter wave detectors have become common-place in airport security. Another application for small-scale superconductors is in front-end filters in cellular phone towers, as in Figure 1.2 [6].

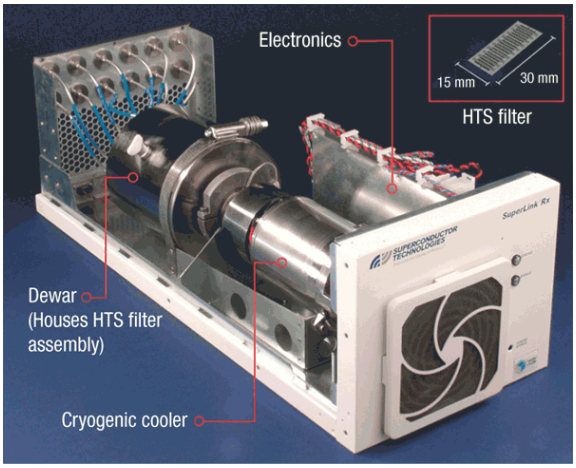

Figure 1.2: Cryogenically cooled front-end filter for use in cellular phone towers, from [6], reproduced with permission from Macmillian Publishers Ltd: Nature Physics, copyright © 2006.

One of the largest areas of applications for small low-temperature and cryogenic coolers is in cooled infrared detectors. The materials HgCdTl and InSb can detect photo-convert infrared photons, but at temperatures above 160 K, internal thermal noise will overwhelm the external thermal-infrared signal. Such infrared detectors were developed by the late 1950s and 1960s for military applications, and have been used for military applications continuously ever sense. One of the largest uses of military infrared sensors is for night-vision equipment, and several small-scale Stirling coolers have been developed to cool such equipment. It has been reported that over 140,000 Stirling coolers had been produced by 1998 for night-vision technologies [1].

1.3 Small-scale Refrigeration Techniques

1.3.1 Stirling Coolers

Small-scale Stirling microcoolers have been the refrigeration system of choice for many small cooled devices. The Stirling cycle was first devised as a heat engine by Robert Stirling in 1815 [7]. In 1832, Robert Herschel proposed reversing the cycle to produce refrigeration [8], and by 1861 Alexander Kirk realized demonstrated cooling based on Stirling cooling [9]. In 1946, the Dutch company Phillips Technology ran a Stirling cooler with a motor until they observed the

liquification of air on the cold-tip, thus demonstrating a Stirling cryo-cooler [10].

An ideal Stirling cycle is illustrated in Figure 1.3a. Two pistons labeled compressor and displacer hold an ideal gas in a volume that also includes a regenerator. The ideal Stirling cycle is a four step process. At the start of the cycle, all of the gas is at a warm temperature and the compressor piston is fully retracted (state 1). During the first step, the compressor extends and does work to isothermally compresses the gas at the warm temperature (states 1-2). In the next step, both pistons move the gas from the warm-side to the cold side of the regenerator in an isochoric (constant-volume) step; in order to maintain constant volume as the temperature decreases through heat exchange with the regenerator, the pressure must decrease (2-3). In the third step, the displacer-piston retracts, removing work from the gas during isothermal expansion at the cold-temperature (3-4). Finally, both pistons move the gas to the warm end in an isochoric step. These steps are plotted in P-V space in Figure 1.3b and temperature-entropy (T-S) space in Figure 1.3c.

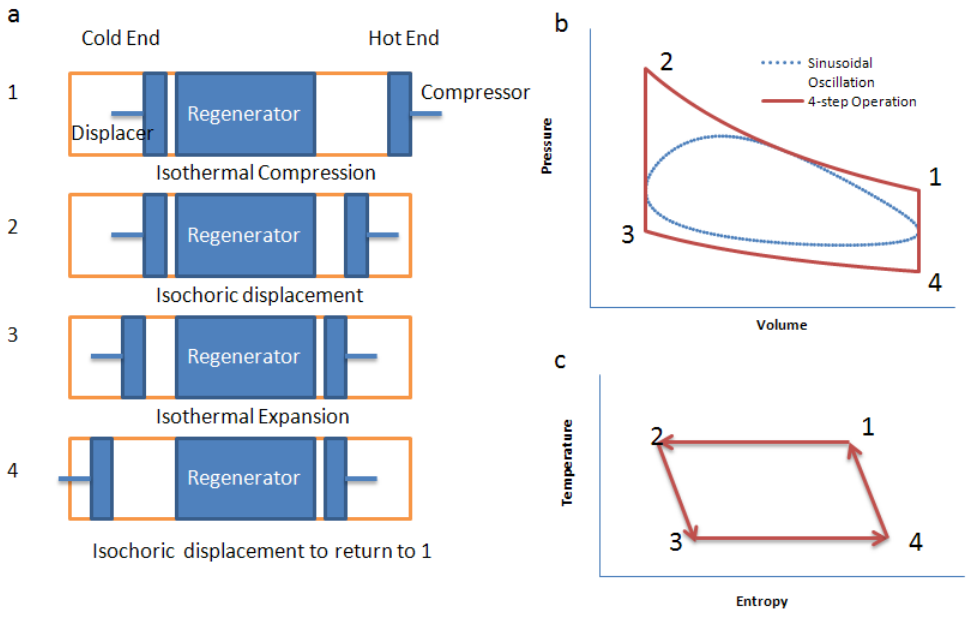

Figure 1.3: a) Schematic of an ideal Stirling cycle refrigerator, b) Stirling cooling cycle in P-V space, shown for a 4-step process (solid red line) and a sinusoidal process (dotted blue line), and

c) the cycle in T-S space.

The work performed by the compressor during reversible compression (from state 1 to 2) will also be the heat rejected by the gas to maintain a constant temperature. Similarly, the work absorbed during reversible expansion by the displacer will be the heat absorbed by the gas (state 3-4):

$$\text{Compression: } Q_{1\text{-}2}=W_{1\text{-}2}=nRT_{hot}\ln(V_{max}/V_{min}).$$

$$\text{Expansion: } Q_{3\text{-}4}=W_{3\text{-}4}=nRT_{cold}\ln(V_{max}/V_{min}).$$

The coefficient of performance (COP) will then be

$$COP=Q_{3\text{-}4}/W_{tot}=Q_{3\text{-}4}/(W_{1\text{-}2}-W_{3\text{-}4})=T_{cold}/(T_{hot}-T_{cold})\ . \qquad (1.1)$$

This is the COP of an ideal (Carnot) cooler. Furthermore, all that is required of the refrigerant is that it acts as an ideal gas. Typically helium is used as a refrigerant, at pressures often of 1 MPa. This is above the critical point of helium, so phase change will not occur for any temperature. However, typically the oscillation of the pistons is sinusoidal, rather than moving in steps. Such a cycle is shown in a P-V plane in Figure 1.3b as the dotted line, which results in a lower heat lift per cycle. One feature of the Stirling cooler is that the oscillation must be slow enough that the refrigerant comes into thermal equilibrium with the regenerator. Deviations from thermal equilibrium will reduce cooling effectiveness considerably. As a practical rule, this prevents Stirling coolers from operating faster than 100 Hz. The cooling power is proportional to frequency. Thus, for a given heat load requirement, there will be a size minimum for the Stirling cooler.

1.3.2 Thermoelectric Coolers

A second method to reach low temperatures with compact systems is with thermoelectric coolers (TECs), which use the thermoelectric effect. In a TEC electrons flow from a metal with some

Fermi Energy (E_f) to a semiconductor with some higher conduction energy (E_c), shown schematically in Figure 1.4. In actual TECs, electrons will flow through p-type and n-type semiconductors, to increase the energy difference compared to a metal-semiconductor system. As electrons flow from an area of high electron density to low electron density, the electron entropy increases and heat is absorbed. This cooling power is expressed in terms of the Seebeck coefficient α. TECs will also experience thermal losses through Joule heating (expressed by resistivity ρ) and heat conduction (expressed with conductivity k). A figure-of-merit is expressed for TEC material as $Z= \alpha^2/\rho k$. The maximum temperature drop of a TEC will be $\Delta T=ZT_L^2/2$. Typical Z values are 0.002/K [11].

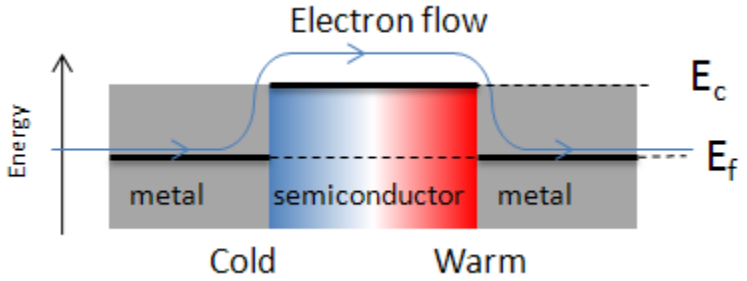

Figure 1.4: schematic of a TEC: as electrons move from a metal at the Fermi energy (Ef) to a semiconductor at the conduction energy (Ec), the electron energy increases and heat is absorbed. As they move back into the metal at E_f, they release heat.

Because of inherent losses, the COP is limited roughly 5%. Additionally, the temperature difference between the warm-end and cold-end is limited, typically to 60 K when cooling from ambient. In order to reach larger temperature differences, multiple TECs can be stacked, which results in much lower efficiencies.

1.3.3 Joule-Thomson Coolers

The third approach for small-scale low-temperature cooling is a mixed-refrigerant Joule-Thomson cycle. This cycle will be covered in much greater detail in the next chapter, but briefly,

a refrigerant is compressed, passes through a heat exchanger where it is chilled, expands through an expansion valve where it cools further, lifts heat on an evaporator, and returns through the heat exchanger. The gross cooling power is the product of the flow-rate of the refrigerant and its enthalpy change as it expands from the high-pressure to the low-pressure. For a well-designed refrigerant, the efficiency can be up to 50% of the Carnot efficiency.

The refrigerant will always travel one direction in such a recuperative cycle. The compressor in this system consists of an oscillating volume and a pair of check valves which rectify the oscillating flow into a direct-current flow. In such a configuration, there is no thermodynamic limit to the maximum frequency at which the compressor can oscillate, and the compressor volume can be minimized. Figure 1.5 compares Stirling coolers, TECs, and Joule-Thomson coolers in terms of power input requirements and overall volumes, showing that Joule-Thomson coolers can achieve the low power-input requirements of Stirling coolers while also achieving the small size of thermoelectric coolers.

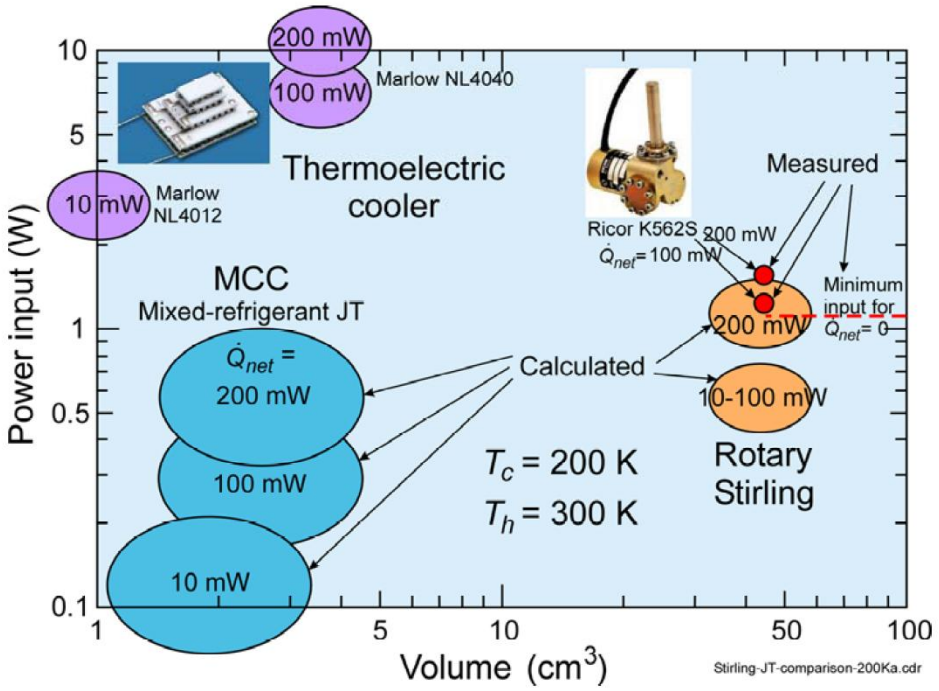

Figure 1.5: comparison of Stirling, TEC, and mixed-refrigerant Joule-Thomson coolers for cooling to 200 K, adapted from [12].

1.4: Micro Fluidics Introduction

When miniaturizing the channels of a J-T refrigeration system, aspects of micro-fluidics must be considered, particularly for refrigerant mixtures undergoing 2-phase liquid and vapor flows. In conventional scale flows, gravity and turbulent mixing are dominant forces. With mixed refrigerants in conventional scale channels, the most common flow regime is "annular with mist," in which a thin film of liquid adheres to the walls of the channel, and a large number of small droplets of liquid are entrained in the vapor core [13]. Turbulent mixing ensures that the composition of the refrigerant mixture is homogenous across the channel. This is shown schematically in Figure 1.6a.

As refrigerant channels shrink, the surface-to-volume ratio increases, and the influence of body forces, such as gravity, give way to surface forces, such as surface tension. The influence of gravity relative to surface tension is characterized by the Eötvös number, defined as $Eo=\Delta\rho a L^2/(4\pi^2\sigma)$, where L is the characteristic length, which is the diameter in channel flow; $\Delta\rho$ is the difference in the density of the liquid and vapor phases; a is a body-force acceleration, in this case due to gravity; and σ the surface tension [14]. For $Eo>1$, gravity dominates. In the context of this dissertation, channels with $Eo>1$ are referred to as macro-channels. For $Eo<1$, surface tension dominates, and in the context of this dissertation, such channels are referred to as mini-channels. For water, the critical diameter for the macro-to-mini transition is 2 mm, and for hydrocarbon refrigerant mixtures, the critical diameter is 1.65 mm.

With mini-channel flow, with refrigerant mixtures, the two most common 2-phase flow regimes are annular flow and slug flow [15]. In annular flow, all of the liquid is held by surface tension along the side-walls of the channel, and vapor flows along the central core. Compared to

macro-channels, the vapor core does not contain liquid droplets. This is shown schematically in Figure 1.6b. In slug flow, the surface tension in the axial direction overcomes the surface tension in the radial direction, and slugs of liquid bridge across the vapor core. This is shown schematically in Figure 1.6c. The transition between annular flow and slug flow is studied in reference [15]. The transition from annular flow to slug flow is found to occur when the vapor fraction is less than a critical value, given by $X_c=a/(G+b)$, where G is the mass flux and a and b are functions of the hydraulic diameter.

In this dissertation, micro-channels are also introduced. In the context of this dissertation, these are channels which hydraulic diameters in the range of 1-100 μm, reserving the term "mini-channel" for those with hydraulic diameters in the range of 0.1-1.65 mm. It will be shown in Chapters 3-5 that the interface of the mini-channel to micro-channel is crucial in determining the cooling power of refrigerant mixtures. Figure 1.6 b and c schematically show the interface of a mini-channel to a micro-channel, in comparison to the interface of a macro-channel to a smaller macro-channel. For the 3 refrigerant flow regimes, the method to calculate the specific cooling power is listed. The models for specific cooling power for the mini and micro-channels are derived and verified in Chapter 4 and 5 respectively.

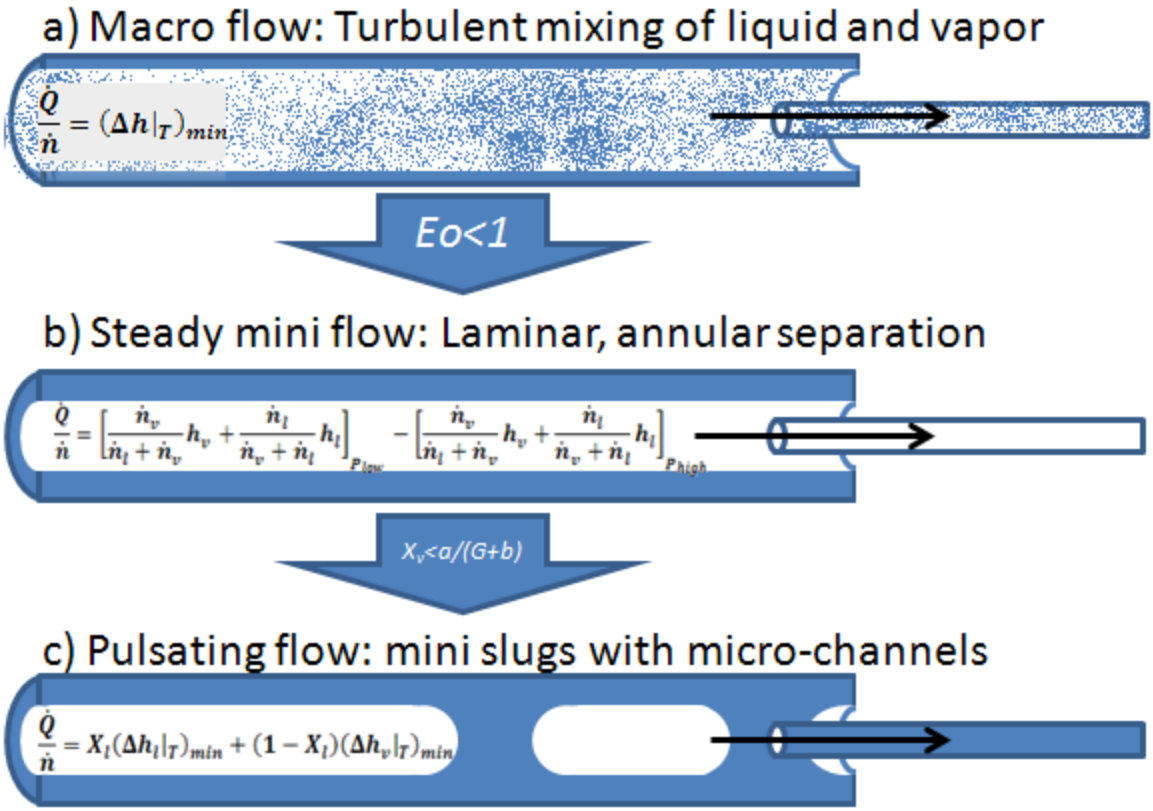

Figure 1.6: Schematic of 3 different flow regimes encountered with mixed refrigerant cryogenic coolers, and expressions for their corresponding specific cooling powers. a) Macro-scale flow in which turbulent mixing ensures an even distribution of refrigerant composition. A thorough review of refrigerant mix design for this situation will be given in Chapter 2. b) Steady, laminar mini-channel occurs when the Bond number is less than 1. In this flow regime, an annular separation between the liquid and vapor phases causes the cooling power to be given by a "cup-mixing" average. This is discussed in Chapter 4. c) Pulsating flow occurs when the mini-channel vapor fraction is less than a critical value. Here slugs of liquid form in mini-channels and have a larger volume than the downstream micro-channels. This allows a complex 2-phase flow phenomenon to be treated as 2 sequential 1-phase flows, as is discussed in Chapter 5.

1.5: Previous work on Micro J-T Cryogenic Coolers at the University of Colorado at Boulder

Previously in our group, a MCC was developed by Mu-Hong Lin with a glass-fiber based heat exchanger and silicon micro-machined expansion valve [16]. The goal of that project was to develop a MCC for cooling 3 mW at 77 K with as small of a flow-rate as possible to enable the

use of micro-scale compressors. The J-T valve on these MCCs is formed by a gap between a silicon chip and a glass chip measuring 2 mm x 2 mm x 0.3 mm. The gap in these studies was 0.705 μm in height. Refrigerant expands radially outward, from a radius of 0.3 to 0.8 mm. The height was determined experimentally to allow a flow-rate of roughly 10 standard cubic centimeters per minute (sccm) through the MCC under a high pressure of 1.6 MPa and low pressure of 0.1 MPa. The fibers were metal-coated at the ends such that they could be soldered to the silicon JT valve chip on the cold-end, and to a larger silicon macro-coupler at the warm-end. In the test set-up, the macro-coupler was fastened to a copper base which was pre-cooled to 240 K by an external cooler.

The compressor used in these studies was a macro-scale non-lubricated 2-stage piston compressor capable of a maximum outlet pressure of 1.6 MPa, with suction pressures as low as 0.06 MPa. Two refrigerant mixtures were studied with this test setup. The first was a 5-component mixture composed of 6% Neon, 42% Nitrogen, 22% Methane, 16% Ethane, and 14% propane. This mixture was designed according to a $(\Delta h|_T)_{min}$ maximization process to cool to 77 K with a high pressure of 1.6 MPa and low pressure of 0.1 MPa, with pre-cooling to 240 K. The thermodynamic background of this type of refrigerant design will be discussed in Chapter 2. The actual performance curve is shown in Figure 1.6. Under a pressure of 1.4:0.07 MPa, the MCC experienced slow cooling to 140 K, where it remained steady for 50 min before a compressor shut-down caused the temperature to raise. However once the compressor was operating again, the cooler temperature dropped back to 140 K rather quickly. A second compressor re-start occurred after another 50 min. Finally, after 5 hours of total operation, the temperature rapidly dropped to 76 K, but this low-temperature cooling was unstable, and wild temperature

oscillations followed. This behavior of 140 K steady cooling and <80 K unsteady cooling was repeated several times with this refrigerant.

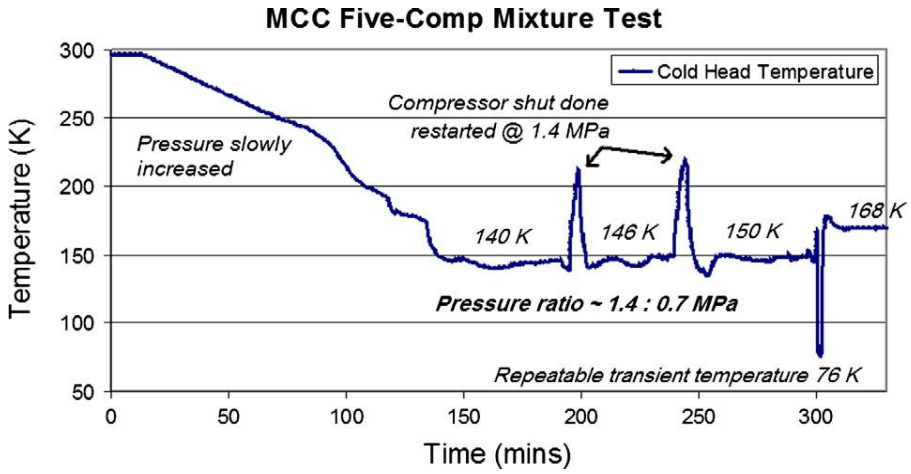

Figure 1.7: Cool-down performance of Lin's MCC operating with a 5-component refrigerant mixture, from [16].

The second refrigerant mixture tested with this set-up was a 3-component mixture, composed of 62% Methane, 14% Ethane, and 24% Propane. This mixture was designed to cool from 240 K to 140 K under the same pressures of 1.6 MPa to 0.1 MPa. The actual cooling response is shown in Figure 1.7. The refrigerant experiences slow cooling at first, with brief periods of rapid cooling. Ultimately, a lowest temperature of 112 K was reached, and this temperature proved to be stable. The cooling to 112 K was repeated several times as well.

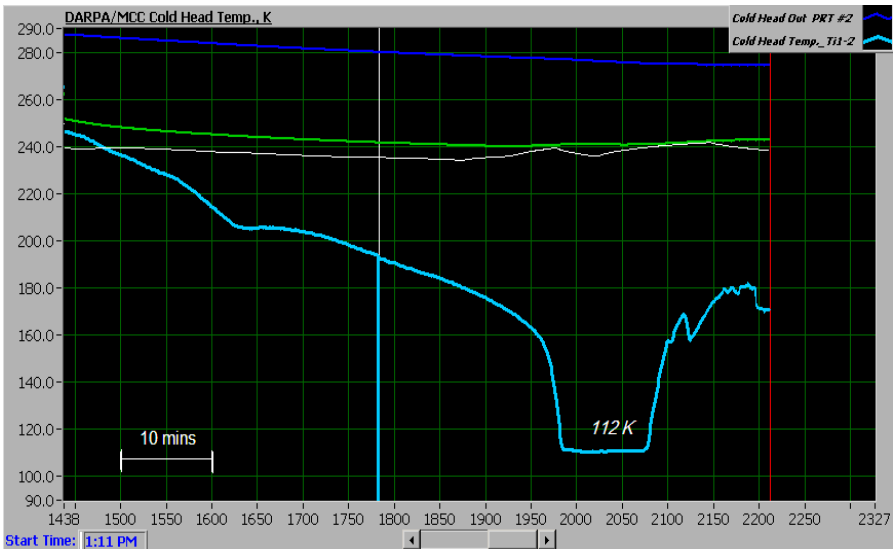

Figure 1.8: Cool-down curve of Lin's MCC with 3-component mixture.

The results of these tests left many questions which must be addressed before realizing a functional micro cryogenic cooler. Why could the 3-component mixture reach lower-than-designed temperatures under steady operation when the 5-component mixture was considerably warmer than the designed temperature during steady operation? What flow phenomena are responsible for the temperature oscillations of the 5-component mixture, and how can we design refrigeration systems to either compensate for or circumvent the temperature fluctuations? Both these issues will be addressed in Chapter 5.

Finally, the compressor used was a macro-scale device, shown in Figure 1.8. As far as the authors know, there are no miniature or micro-scale compressors which can generate the 16:1 pressure ratios seen in these experiments. Small oil-lubricated compressors produced for vapor compression refrigerators have been reported to reach 4:1 compression ratios, but oil lubrication can clog the micro-channels of MCCs. So mixed refrigerants must be designed for such lower pressures, and miniature oil-free compressors must be developed. This issue will be addressed in Chapter 3.

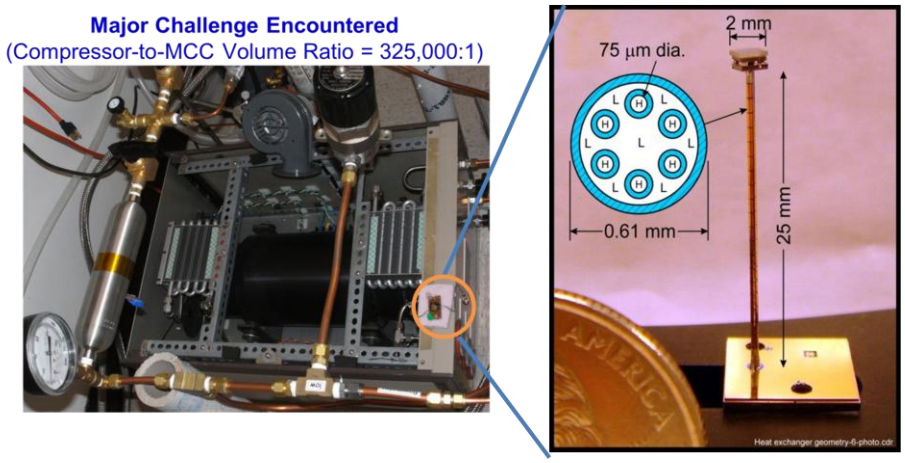

Figure 1.9: The compressor used to drive Lin's MCC, which has a 325,000:1 volume ratio with the MCC.

1.6 Goals of this Dissertation

The goals of this Dissertation are listed below:

- Develop a miniature compressor with a >4:1 compression ratio and demonstrate low-temperature cooling with a new low-pressure refrigerant mixture.
- Understand steady flow, including a model of refrigerant cooling power.
- Understand pulsating flow, including developing a model of refrigerant cooling power.

The understanding of both steady flow and pulsating flow, in comparison to homogenous flow, are represented schematically in Figure 1.6.

1.7 Summary of Dissertation:

1.7.1: Summary

This dissertation covers the development of the mixed-refrigerant Joule-Thomson micro cooler and associated micro compressor, an analysis of the steady flow regime, an analysis of the pulsing flow regime, and the development of a model both regimes which can be used to optimize refrigerant composition and performance in micro coolers. Chapter 2 covers a review of the thermodynamics of refrigerant mixtures and previous work in micro cryogenic coolers.

Chapter 3 covers the development of the micro cooler, miniature compressor, and the testing of refrigerant mixtures. In chapter 4, it is found that the steady flow regime corresponds to hold-up of the liquid components of the mix, which can be modeled according to a solution of the Navier-Stokes equations for annular flow in a mini-channel. In chapter 5, the pulsing flow regime is found to correspond to the development of liquid slugs in high-pressure mini-channels that completely fill the micro-channels. With this understanding, the complicated 2-phase refrigerant flow is modeled as two single-phase flows experienced sequentially by the micro cooler. Furthermore, a model of refrigerant cooling power is derived and verified for mixed refrigerants undergoing pulsating flow. Figure 1.6 summarizes the model of cooling power for (b) steady flow and (c) pulsating flow, in comparison to typical homogenous flow (a) experienced by macro-scale mixed refrigerant coolers.

The steady flow model will be valid when a non-azeotripic refrigerant mixture experiences an annular two-phase flow pattern in mini-channels. The steady flow model will fail if the liquid phase in the mini-channel fills too much of the volume, and the flow is no longer annular; in that case the pulsating flow may apply. The pulsating flow model will apply in mixed-refrigerant systems when liquid slugs form in mini-scale channels before passing into micro-channels. The limitation of this model is the assumption that 2-phase flow can be modeled as two single-phase flows, which will not be valid if volume of the liquid slugs is not greater than the volume of the micro-channels—such as in fully integrated micro-compressor/micro-cooler systems that have no mini-scale coupling channels.

Finally, Chapter 6 covers the development of a PZT-based, MEMS-enabled micro compressor. Chapter 7 provides a summary and conclusions, including the application of the model of pulsating flow in order to re-optimize the design of a refrigerant mixture for cooling to

160 K. Chapter 7 also includes future work in the context of this project.

1.7.2: Major contributions of this work

The major contributions of this work are highlighted as follows:

- The development of a non-lubricated miniature, capable of generating a high pressure of 0.75 MPa with a suction pressure of 0.1 MPa,
- Demonstration of low-temperature cooling with a refrigerant mixture at a high pressure of 0.4 MPa, which is 4x lower than the current state-of-the-art in J-T cooling, and enables the use of mini-scale compressors,
- The development of a model of steady flow in terms of liquid hold-up due to annular flow in high-pressure mini-channels. This model is verified with isothermal enthalpy difference measurements and refrigerant composition measurements.
- The development of a model of pulsating flow in terms of slugs of liquid in high-pressure mini-channels. This understanding allows the development and verification of a model of refrigerant cooling power. Furthermore, the model is used to re-optimize a refrigerant mixture designed to cool to 160 K using a 4:1 pressure ratio, increasing the specific cooling power and ideal J-T coefficient of performance from 276.6 J/mol and 8.36 % to 831 J/mol and 32.8 %.

CHAPTER 2: THERMODYNAMICS AND PREVIOUS WORK IN JOULE THOMSON-BASED MICRO CRYOGENIC COOLERS

This chapter covers the history and thermodynamics of Joule-Thomson coolers. The principles of heat transfer in Joule-Thomson coolers are used to optimize the length of the heat exchanger. History and thermodynamics of refrigerant mixtures are introduced as well and used for refrigerant mixture design optimization. Implicit in that design process was the assumption that the liquid and vapor components of the refrigerant move with the same flow-rate, such as encountered in large-scale systems. This chapter also gave a review of previous JT MCC development. All of the previously developed MCCs have used either a large high-pressure refrigerant supply bottle or a larger compressor to drive them. Work with refrigerant mixtures for low-pressure operation with a micro or miniature compressor has not been reported.

2.1: Ideal Refrigeration Thermodynamics.

The generalized refrigeration process is shown schematically in Figure 2.1. In general, work (W) is done to a system in order to move heat across a temperature gradient. Heat on the warm-side of the system (Q_w) is transferred to ambient temperature (T_A), while on the cold side heat (Q_c) is absorbed at some cold temperature (T_c). Carnot proved that no heat-engine cycle could be more efficient than one where no net entropy is produced, that is to say a reversible cycle [17]. The theorem applies as well to refrigeration cycles. The Carnot ideal refrigeration cycle is shown in Figure 2.1b. Section 1.3.1 showed that an ideal Stirling cycle is a reversible one, so it must have the maximum coefficient of performance (COP), and the COP of the Carnot cycle will be equivalent:

$$COP_{Carnot} = \frac{T_c}{T_h - T_c} \tag{2.1}$$

In Section 1.3.4, it was also argued that the Stirling cycle, although it has potentially high efficiencies, cannot be miniaturized as well as a Joule Thomson (J-T) cycle can. The remainder of the chapter will be concerned with J-T cooling

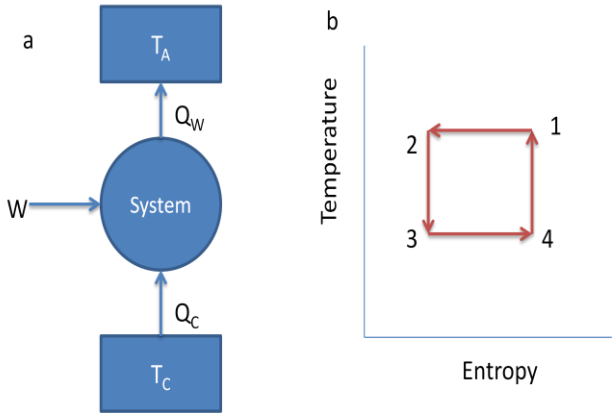

Figure 2.1: a) schematic of a refrigeration process. Heat on the warm-side of the system (Q_w) is transferred to ambient temperature (T_A), while on the cold side heat (Q_c) is absorbed at some cold temperature (T_c), and work (W) is done on the system to move the heat. b) idealized Carnot refrigeration cycle on a T-s plane. Each step is reversible; therefore this cycle has the highest coefficient of performance possible.

2.2 Joule Thomson Cooling

2.2.1 Thermodynamics

From 1852-1856, James Prescott Joule and William Thomson (Lord Kelvin) conducted a systematic study of the cooling experienced by gas as it expanded from some pressure into a lower pressure. Joule contributed experimental data by placing a flow restriction (typically a cotton ball) in an insulated tube filled with gas, and pulling a vacuum on the other side. As the gas dropped in pressure, it would subsequently cool. Thomson analyzed the experiments and showed that the process is isnthalpic. To move some mass (m) of gas from a high pressure (P_1) at a specific volume v_1 to a low pressure (P_2) at a new specific volume v_2 requires work given by $W=mP_2v_2-mP_1v_1$. In Joule's experiments the gas experienced neither heat transfer nor changes in

kinetic energy, so an application of the 1st Law of Thermodynamics states that the change in internal energy ($U=m\,u$) and work done by the system must sum to zero:

$$mu_2\text{-}mu_1+mP_2v_2\text{-}mP_1v_1=0 \quad (2.2).$$

Specific enthalpy is defined as $h=u\text{-}Pv$, so Equation 2.2 reduces to $h_2\text{-}h_1=\Delta h=0$. Thomson also defined a coefficient μ_{JT} as the partial derivative of temperature with respect to pressure at constant enthalpy:

$$\mu_{JT} \equiv \frac{\partial T}{\partial P}\Big|_H \quad (2.3).$$

This is now referred to as the Joule-Thomson coefficient. Refrigerants with a positive J-T coefficient will experience cooling upon expansion, whereas those with a negative J-T coefficient will warm, and those with a zero-valued J-T coefficient will not experience a temperature change accompanying any pressure change [18].

Applying Maxwell's Relations, the J-T coefficient can be re-written as $\mu_{JT} = 1/C_p(T \cdot \partial v/\partial T - v)$, where C_p is specific heat. For an ideal gas, $\partial v/\partial T = v/T$, and the J-T coefficient will be zero. The behavior of J-T cooling or heating of a *real* gas can be understood in terms of the intermolecular potential between the molecules. The potential energy between two molecules is subject to a short-range repulsive component, and a longer-range attractive component; these are often modeled according to the Leonard-Jones 6-12 potential. Such a potential curve is shown in Figure 2.2. As a gas expands to a lower pressure, the molecules will move further apart. In case 1, the gases will go up in potential energy. In Joule's experiments, no heat is transferred to the gas, nor any work done by the gas. The simple argument goes that as potential energy increases, thermal energy must necessarily decrease, which corresponds to a temperature drop in the gas. Thus the J-T coefficient will be positive. In case 2, the refrigerant will decrease in potential energy as it expands, causing higher thermal energy, heating, and a negative J-T

coefficient.

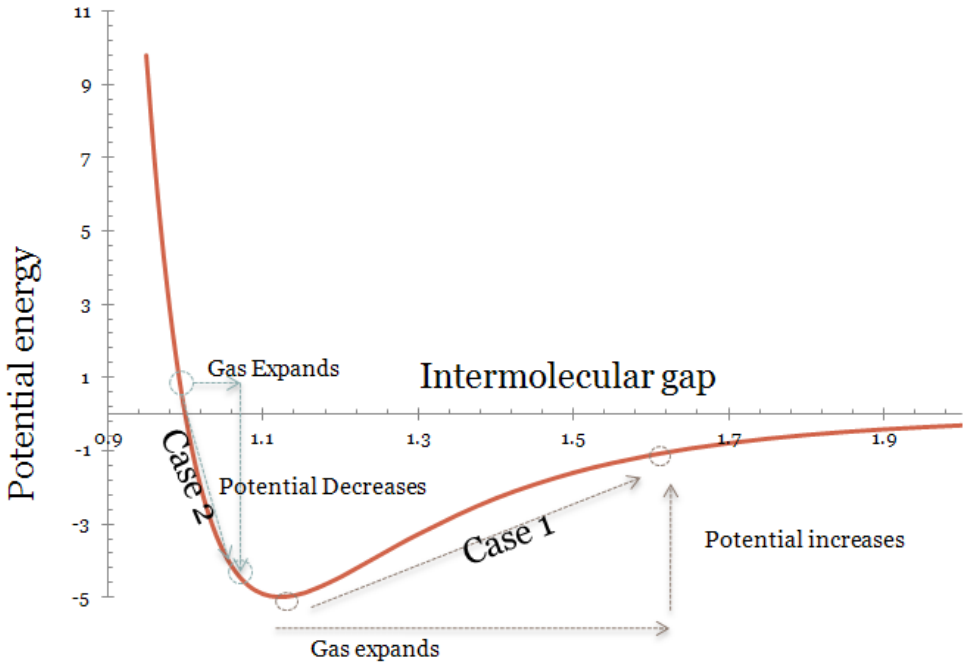

Figure 2.2: A Lenard-Jones 6-12 potential, plotting potential energy against intermolecular gap, with 2 cases of gas expansion. In Case 1, the gas expands, potential energy increases, and the gas cools; in Case 2, the gas expands, potential energy decreases, and the gas heats.

The point where the J-T coefficient changes in sign is known as the inversion point, and it can occur when the refrigerant is at an elevated temperature or pressure, such that the molecules start too closely together. The J-T coefficient for Helium and Nitrogen is plotted against temperature for different pressures in Figure 2.3a and b. Note that for pressures of 4 MPa, there is no inversion point for Helium, and the J-T coefficient is always negative. The maximum inversion temperature of Helium is 39 K, and therefore a system using helium undergoing J-T expansion must first pre-cool the helium to below that temperature in order to experience cooling with the He. Nitrogen, on the other hand, has a maximum inversion temperature of 621 K. Nitrogen is thus an acceptable refrigerant for J-T cooling from room temperature, as is air. For Nitrogen, the pressure which provides maximum cooling from 300 K is 40 MPa. Values are

calculated by the NIST thermophysical calculation software REFPROP [19].

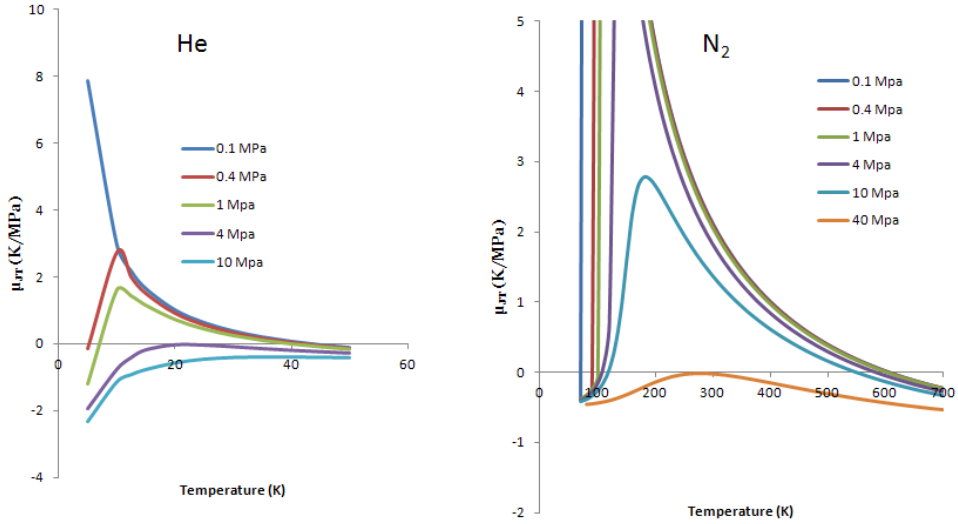

Figure 2.3: Joule-Thomson coefficient (μ_{JT}) of a) Helium and b) Nitrogen gas as a function of temperature for different pressures. In situations where (μ_{JT}) is negative, gas will experience heating as it expands. Note for Helium, (μ_{JT}) is always negative for pressures above 4 MPa. The maximum inversion temperature is 39 K. For Nitrogen, (μ_{JT}) is always negative above 40 MPa, and the maximum inversion temperature is 621 K.

The Joule-Thomson effect was put to use for liquefying air in a cycle invented independently by Carl von Linde and William Hampson in 1895. The cycle is shown in Figure 2.4a. The air starts at ambient conditions, is compressed to ~10 MPa, enters a heat exchanger (HX) where it cools down, then expands across some flow restriction valve (the J-T valve), where the air will cool to become a saturated liquid. The liquefied air is separated and collected in a phase-separator, and the vapor returns through low-pressure channel of the counter-flow heat exchanger to pre-cool the incoming high-pressure air. This cycle can be modified into a proper refrigerator by replacing the phase-separator with an evaporator, shown in Figure 2.4b. With that modification in place, the system is known as the Joule-Thomson refrigeration cycle, and can be run with any number of pure or multi-component refrigerants. The cycle is shown on a

Temperature-Enthalpy diagram in Figure 2.4c.

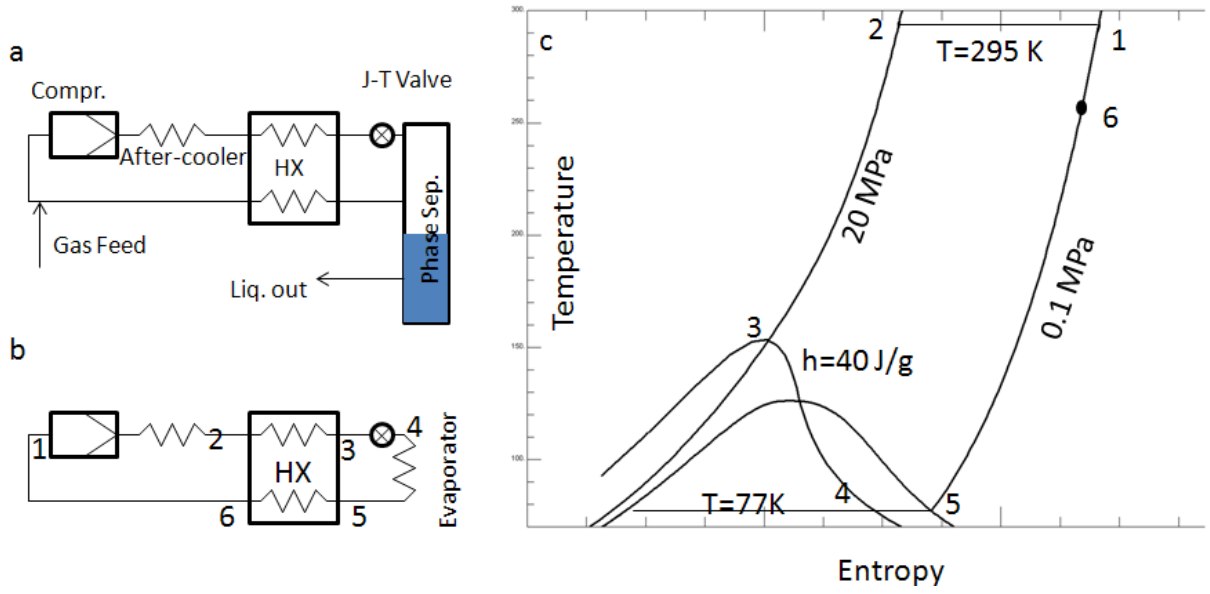

Figure 2.4: a) schematic of a Lind-Hampson Liquefier, b) the liquefier modified to become a J-T cooler, with 6 states labeled, and c) the 6 states on a T-s diagram, which also includes the isenthalpic line h=40 J/g. Values are calculated for N_2 with REFPROP.

The steps of J-T refrigeration are as follows: from state 1, the refrigerant is compressed to high pressure. This compression process can heat the refrigerant, and any excess heat is rejected to ambient, arriving at state 2. The refrigerant enters the heat exchanger, and is cooled to some much lower temperature by the outgoing refrigerant, to state 3. The refrigerant then enters the JT valve and undergoes isenthalpic expansion and crosses the saturation curve to reach the liquid boiling temperature at the low pressure at state 4. From there, the liquid will evaporate and absorb heat until it is all vapor at state 5. The cooled refrigerant returns through the HX, and exits at some temperature below ambient at state 6. The difference between the temperatures at states 6 and 1 is determined by the effectiveness of the heat exchanger.

The effectiveness of a heat exchanger is defined as the ratio of the heat transfer rate to the maximum possible heat transfer rate. In a classical heat exchanger, this is given by (See Eqn 1.48 of [15]):

$$\varepsilon = \frac{(\dot{n}c_p)_c(T_{h,in}-T_{h,out})}{(\dot{n}c_p)_{\min}(T_{h,in}-T_{c,in})} \tag{2.4}$$

Here, $\dot{n}$ refers to the molar flow-rate, c_p is the specific heat in J/mol, the subscripts h and c refer to hot and cold respectively, and the $(\dot{n}c_p)_{\min}$ term in the denominator implies using the minimum between the hot or cold-stream values. This expression assumes that the specific heat is constant in each refrigerant stream. However, the specific heat will change considerably with temperature in J-T cryo-coolers in both the high- and low-pressure streams. Furthermore, for a pure refrigerant such as nitrogen, the minimum enthalpy occurs in the cold low-pressure stream, so the effectiveness can be given by:

$$\varepsilon = \frac{h_6-h_5}{h_1-h_5} \tag{2.5}$$

Consider a control volume around the heat exchanger, J-T valve, and evaporator. A conservation of energy dictates that the heat load which will be lifted at the evaporator will be given by the difference between the enthalpy flow of the high-pressure inlet and the low-pressure outlet: $\dot{Q} = \dot{n}(h_6 - h_2)$. The cooling power will be zero when h_6=h_2, which will occur when the effectiveness of the heat exchanger is given by a critical value: $\varepsilon_{crit} = (h_2 - h_5)/(h_1 - h_5)$. The three states used to calculate critical effectiveness only depend on the temperature, pressure, and composition of the refrigerant, and not on the system geometry. For a nitrogen system at 10 MPa, the heat exchanger must be more than 95.1 % effective. Table 2.1 lists the critical effectiveness of several refrigerants at 1 MPa, 4 MPa, 10 MPa of high pressure and 0.1 MPa of low pressure.

	1 MPa	4 MPa	10 MPa
Nitrogen	99.5 %	97.9 %	95.1 %
Methane	97.6 %	89.8 %	73.6 %
Ethane	89.0 %	0	0
Propane	0	0	0

Table 2.1: Critical effectiveness of heat exchangers for 4 pure refrigerants at 3 high-side pressures. The low-side pressure was taken to be 0.1 MPa and the low temperature taken to be the boiling point of the refrigerant at 0.1 MPa.

Note that in several of these cases the critical effectiveness is zero. In those cases, the heat exchanger is not necessary for the cooler's operation. With the heat exchanger removed, the cooler becomes the familiar vapor-compression system, shown in Figure 2.5a. Although the heat exchanger is not required, its presence will still increase the efficiency of a vapor-compression system, as in Figure 2.5b.

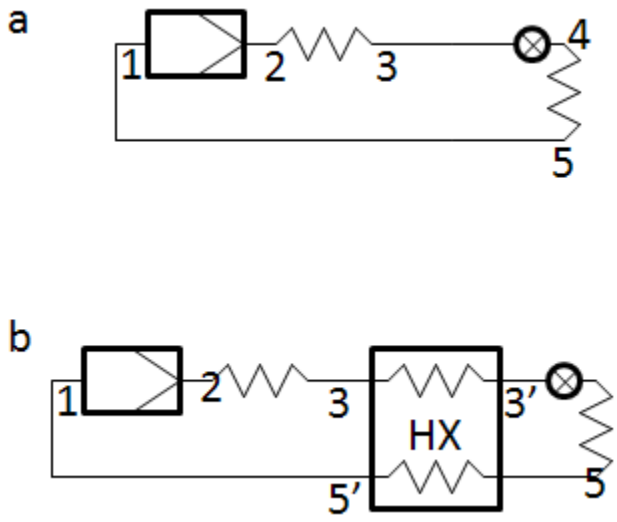

Figure 2.5: Vapor compression refrigerator a) with and b) without a heat exchanger.

2.2.2 Heat Exchanger Design

For systems which do require heat exchangers, care must be paid to ensure the heat exchanger is effective enough. Furthermore, real heat exchangers will create several parasitic heat loads [20]. Heat can be conducted axially (longitudinally) down the length of the heat exchanger, causing a conductive loss $\dot{Q}_{cond}$. Radiation from ambient conditions can be absorbed along the outer surface are of the heat exchanger $\dot{Q}_{rad}$. As refrigerant flows through the channels of the heat

exchanger, there will be some pressure drop due to friction, which will lower the enthalpy difference between the high-pressure and low-pressure streams. This can be thought of as a parasitic load due to pressure drop $\dot{Q}_{\Delta P}$. Finally, the heat exchanger ineffectiveness will decrease the cooling power, compared to a real system, $\dot{Q}_{HX}$. The radiative and pressure drop loads will increase with increasing length of the heat exchanger, whereas the conductive and the ineffectiveness loads will decrease with the length of the heat exchanger. This implies an optimization process can determine the length of heat exchanger which will minimize the parasitic loads: $\dot{Q}_{cond} + \dot{Q}_{rad} + \dot{Q}_{\Delta P} + \dot{Q}_{HX}$.

In an ideal Joule-Thomson cooler, the temperature of the high-pressure stream and the low pressure stream will be equal some the pinch point, which will occur at the warm-end for pure refrigerants. At that point, the difference between the enthalpies of the high-and low-pressure streams will be at a minimum. The ideal cooling power will be given by the product of the flow-rate and the specific enthalpy difference between the low and high pressure at that temperature: $\dot{Q}_{gross} = \dot{n}\Delta h_{\min}$. In real systems, it has been reported that cooling can occur when the sum of the parasitic loads is less than 60% of the ideal cooling power: $(\dot{Q}_{cond} + \dot{Q}_{rad} + \dot{Q}_{\Delta P} + \dot{Q}_{HX})/\dot{Q}_{gross}$<0.6 [20].

The conductive heat loads on the HX be calculated by Fourier's Law. If conduction is the dominant form of heat transfer, the temperature profile will be linear, and the conductive heat load expression will reduce to $\dot{Q}_{cond} = kA\Delta T/L$. Here T is temperature as a function of the length of the heat exchanger, k is the thermal conductivity of the heat exchanger, L is HX length, and A is the cross-sectional area.

The radiative heat loads can be calculated by the Stephan-Boltzmann Law: $\dot{Q}_{rad} = \int_0^L \sigma\epsilon P(T_{amb}^4 - T(l)^4)dl$. Here T_{amb} is the ambient temperature, σ the Stephan-

Boltzmann constant, *P* the perimeter of the HX along a cross-section, and ϵ the emissivity. If the temperature profile is linear between T_{amb} and T_{cold}, then the heat load would be: $\frac{\sigma\epsilon PL}{5}(T_{amb}-T_{cold})(4T_{amb}^3+3T_{amb}^2T_{cold}+2T_{amb}T_{cold}^2+T_{cold}^3)$.

The pressure drop heat load can be found from (see Eqn 25 in [20]):

$$\frac{\dot{Q}_{\Delta P}}{\dot{Q}_{gross}}=\frac{\Delta P}{h_{min}}\left(\frac{\partial h}{\partial P}\right)_T \tag{2.6}$$

The pressure drop as a function of length will be given by:

$$\Delta P=\frac{fRe}{2}\frac{\mu L\dot{n}}{\rho d_h^2 A} \tag{2.7}$$

Here, *f* is a friction factor, *Re* Reynolds number, μ viscosity, d_h hydraulic diameter, and *A* cross-sectional area of the fluid channel. In the small-scale cooling systems considered in this dissertation, the flow will be laminar, and the ratio of friction factor and Reynolds number will be constant. The value of $\left(\frac{\partial h}{\partial P}\right)_T$ can be found through an equation of state for the refrigerant.

The heat exchanger ineffectiveness load will be given as:

$$\frac{\dot{Q}_{HX}}{\dot{Q}_{gross}}=(1-\varepsilon)\cdot\frac{(h_h-h_c)_{\min}}{\Delta h_{\min}} \tag{2.8}$$

In the numerator, the minimum refers to the stream (high-pressure or low-pressure) which has the lowest difference between hot and cold enthalpies. The term ε is again the effectiveness of the heat exchanger. However, this is often difficult to calculate so for the present analysis, a "number of transfer units" (N_{tu}) approach is used, where $N_{tu}=1/(1-\varepsilon)$. The number of transfer units can be calculated as:

$$N_{tu}=\int_0^L\frac{h_{HX}(l)d_h}{\dot{n}\left(c_p(l)\right)_{min}}dl \tag{2.9}$$

where $h_{HX}(l)$ is the forced-convection heat transfer parameter (not to be confused with an enthalpy) as a function of length, and $\left(c_p(l)\right)_{min}$ refers to the stream (high or low-pressure)

which has the lowest specific heat, at each length. The heat transfer parameter between the low-pressure and high-pressure streams through a wall of thickness *t* will be given by:

$$h_{HX} = \left(\frac{1}{h_{HX,high}} + \frac{1}{h_{HX,low}} + \frac{t}{k_{wall}} \right)^{-1} \tag{2.10}$$

and the heat transfer parameter of each of the streams will, assuming the refrigerant is in a single phase, be given by the product of the Nusselt Number and thermal conductivity of the refrigerant in the stream, divided by the hydraulic diameter of the stream: $h_{HX,high}=k_{high}Nu/d_h$.

To illustrate this concept, the parasitic heat loads of the fiber-based MCC developed by Lin [21] are calculated with Nitrogen as a refrigerant. Two particular conditions are considered: first with the Nitrogen high-pressure at 40 MPa, and second with Nitrogen at a high-pressure of 2.5 MPa. The 40 MPa case gives Nitrogen's highest possible performance, but requires special multi-stage high-power compressors. The high-pressure of 2.5 MPa is chosen as this is the high pressure that common household refrigerator compressors can generate. The individual parasitic heat loads as well as their sums are plotted in Figure 2.6 a (40 MPa) and 2.6 b (2.5 MPa). Note that for the low-pressure case, the refrigerator will never be above the 60 % cutoff required to achieve cooling. In order to use Nitrogen as a refrigerant in these sorts of MCCs, very high pressures are required.

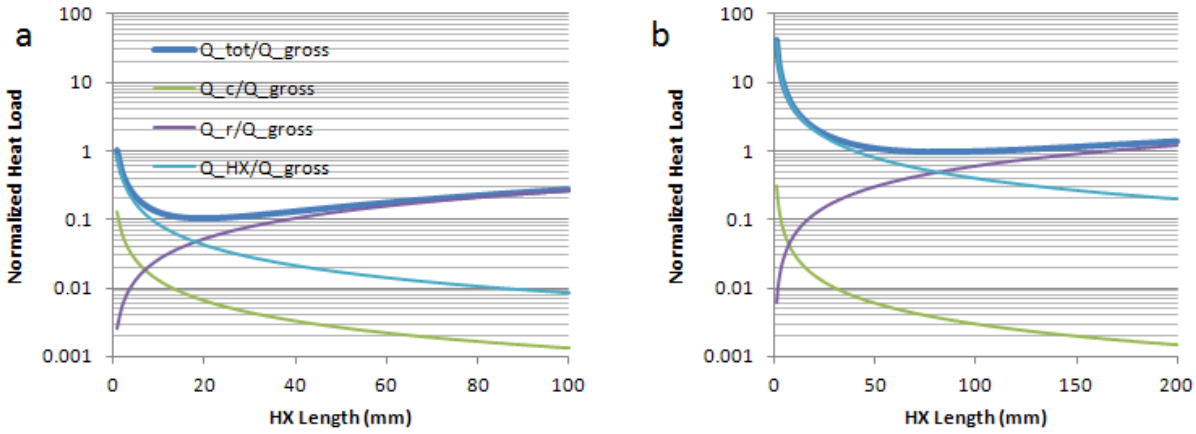

Figure 2.6: Parasitic heat loads of Lin's MCC operating with Nitrogen refrigerant with a high-side pressure of (a) 40 MPa, and (b) 2.5 MPa. The low-side pressure is 0.1 MPa for both of these calculations.

However, miniature-scale compressors are limited in the output pressure available, as will be discussed in greater detail in Chapter 3. A typical high-pressure that is possible to generate with a miniature compressor is in the range of 0.4-0.8 MPa. In order to provide a system which can operate with a shorter heat exchanger and low driving pressure, refrigerant mixtures can be used. Refrigerant mixtures are designed to have some fraction of the mixture in liquid-phase throughout most of the heat exchanger. This two-phase flow will result in higher heat transfer parameters. Furthermore, refrigerant mixtures can have substantially higher enthalpy differences between the high and low pressure streams at any temperature, as the high-pressure stream can have a higher liquid fraction than the low-pressure stream at the same temperature, and the evaporation of some of that liquid will yield large enthalpy changes. These concepts will be discussed in more detail in section 2.3.4.

2.3 Refrigerant Mixtures.

2.3.1 History of refrigerant mixtures for Joule-Thomson cryocoolers.

The earliest incarnation of Joule-Thomson cooling with refrigerant mixtures was used in natural gas liquefaction over 8 decades ago [22]. Natural gas typically is composed of methane, with some heavier hydrocarbons as well as nitrogen, oxygen, and carbon dioxide. Each of these components is a refrigerant in its own right, which makes natural gas a naturally occurring refrigerant mixture. However, the use of mixed refrigerants for general cryogenic cooling only emerged 3 decades later under classified programs in the Soviet Union [1]. By the 1980's, unclassified mixed refrigerant research began in other countries [23].

In the cryogenics field, multiple refrigerants were first used in separate cycles in which one refrigerant loop is used to pre-cool a second refrigerant loop, and the second loop can pre-cool a third loop, and so on. Each stage of the loop will use a refrigerant with a lower boiling point than the previous one. This type of cycle is known as a refrigeration cascade, and is shown schematically in Figure 2.7a. Each stage of the cascade requires its own compressor, but in the 1960's, the Soviet scientist Klemeenko pioneered the use of a single compressor to run a cascade cycle. The single compressor compresses a mixture of each refrigerant used in the cascade. The mixture enters a CFHX where it cools, and then is throttled to low pressure, and cools further to the point where the heaviest component liquefies. A phase separator removes the liquid, which returns through the low-pressure CFHX. The remaining vapor-phase refrigerant continues to a second heat exchanger and phase separator. This cycle is shown in Figure 2.7b, and is known as the auto-refrigeration cascade. Eventually, the phase separators were removed altogether such that the entire refrigerant mixture travelled through one heat exchanger. This cycle has been referred to as the Klemeenko cycle, the one-flow cascade, or simply the mixed-refrigeration Joule Thomson cycle (MRJT). The hardware is for a MRJT refrigerator is identical to that of a standard J-T cooler [18].

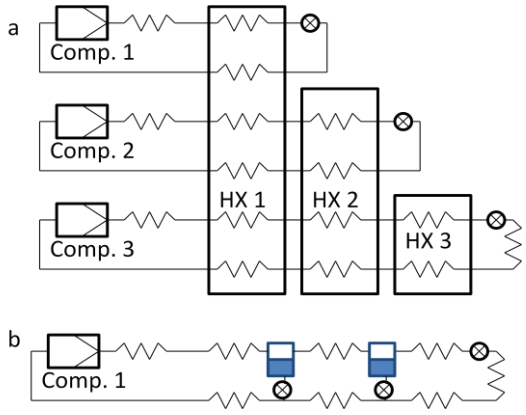

Figure 2.7: schematic of a) refrigerant cascade and b) auto-refrigerant cascade. In the refrigerant cascade, the first compressor uses a high boiling-point (BP) refrigerant such as propane which cools to 230 K, the second uses an intermediate BP refrigerant such as methane which cools to 112 K, and the third uses a low BP refrigerant such as N_2, which cools to 77 K. The Auto-refrigeration cascade uses a mixture of all 3 refrigerants.

2.3.2 Thermodynamics of Refrigerant Mixtures

Mixtures are different from their pure refrigerant counterparts in that the mixtures will not have a single boiling point at each temperature, but rather two points: the bubble-point and the dew-point. At temperatures below the bubble-point, the mixture will be a sub-cooled liquid; at temperatures above the dew-point, the mixture will be a super-heated vapor. Between the two saturation points, both a liquid and vapor phase will co-exist. The temperature difference between the dew-point and bubble-point is known in the refrigeration field as the temperature glide. The two saturation temperature curves are plotted as a function of mass fraction of ethane in an ethane-propane binary system, to illustrate this point.

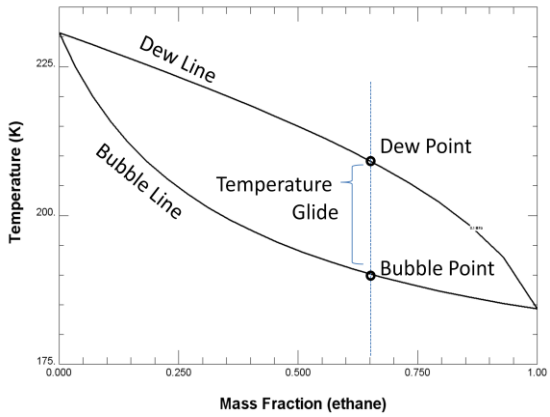

Figure 2.8: Bubble and dew saturation curves as a function of ethane fraction in an ethane-propane binary mixture. The dew-point, bubble-point, and temperature glide are all noted for a mixture of 65% ethane and 35% propane. Curves are calculated with REFPROP.

Note from Figure 2.8 that the bubble point of the mixture is higher than the boiling point of ethane. In general for a two-phase vapor-liquid equilibrium (VLE) system, the bubble point will be higher than the boiling point (BP) of the lowest boiling component. However, in some refrigerant mixtures, the lowest BP component can form a liquid that is immiscible with a liquid formed of the higher BP component, forming a vapor-liquid-liquid equilibrium. This is illustrated with a binary mixture of Nitrogen and Ethylene in Figure 2.9. The inflection point in the bubble saturation curve indicates the presence of a separated immiscible liquid, formed of nitrogen. The mixture's bubble point under that situation is governed by the Nitrogen. In general, Nitrogen can form an immiscible liquid with hydrocarbons heavier than methane, and highly polar hydrofluorocarbons will phase-separate from non-polar perfluorocarbons, hydrocarbons, and atomic refrigerants such as Argon and Xenon.

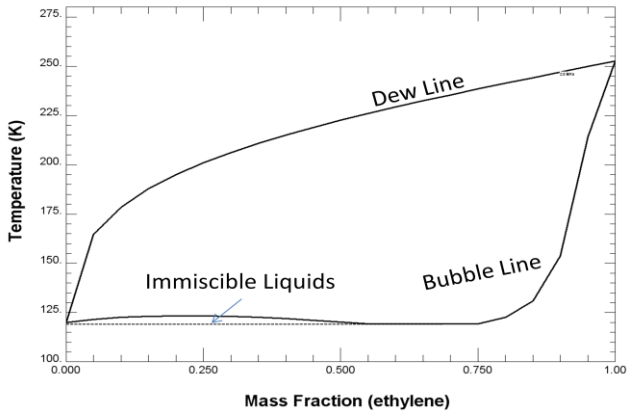

Figure 2.9: Dew and bubble lines of a nitrogen/ethylene mixture at 2.5 MPa. The inflection in the solid bubble line calculated for VLE indicates the existence of an immiscible liquid which would have a bubble line given by the dashed line.

In order to further lower the bubble point of such a system, the partial pressure of the lowest BP component can be reduced. This can be accomplished by using a lower compressor suction pressure, or by adding lighter components to the mixture which do not liquefy, such as Neon or Hydrogen.

The cooling power analysis of MRJT coolers is somewhat different than that of pure components, and was first derived by Radebaugh in 1995 [24]. Consider a control volume drawn about the J-T valve, evaporator, and some portion of the heat exchanger in an ideal J-T cooler, shown in Figure 2.10. This hypothetical J-T cooler has no heat losses due to radiation and convection. The cooling power that can be lifted at the evaporator will be given by the product of the flow-rate and the difference of the specific enthalpy between the inlet and outlet of the control volume: $\dot{Q} = \dot{n}(h_{out} - h_{in})$. Because the control volume is chosen at an arbitrary length, the specific cooling power will be given by the change in the enthalpy between the high and low pressure at any arbitrary location of the heat exchanger: $\dot{Q}/\dot{n} = \Delta h|_L$. But we wish to calculate these enthalpies from an equation of state, and location is clearly not a state function. Instead, we

can calculate the change in enthalpy at a constant temperature $\Delta h|_T$. For an ideal J-T cooler system, the constant temperature difference will correspond to a constant-location enthalpy difference at one single point. A second-law analysis shows that this location will occur at the temperature where $\Delta h|_T$ is at its minimum. (The second-law analysis is performed more rigorously in Appendix A.) This minimum can occur at the warm-end, the cold-end, or somewhere between the temperature extremes. One must be cautions however, when using a calculated $\Delta h|_T$ of a 2-phase mixture, because an inherent assumption is that a mass-averaging function will capture what is known in chemical engineering as "cup mixing." This is true for macro-scale coolers where turbulent mixing ensures that the composition of the fluid is constant across the cross-section of the channel. For micro- and mini-channel flow, will not be the case, so a special "cup mixing" specific cooling power derivation will be presented in Chapter 4.4.1 for steady flow and 5.4.4 for pulsating flow.

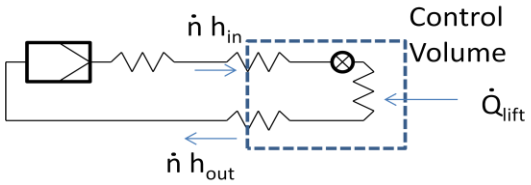

Figure 2.10: Control volume drawn about a portion of the heat exchanger, enclosing the J-T valve and evaporator.

In conventional-scale channels, the enthalpy of a refrigerant mixture will vary considerably as it is cooled. As components partially liquefy, the enthalpy will change in a non-linear fashion. The curves will be a function of both high and low pressure, and composition. Recall that the maximum high-side pressure that can be used to drive Nitrogen as a refrigerant is near 40 MPa. Expanding from that pressure to 0.1 MPa, Nitrogen has a specific cooling power of $(\Delta h|_T)_{min}$=1164 J/mol. A typical refrigerant mixture can achieve the same greater cooling power with a driving pressure of 2.5 MPa, shown in Figure 2.11. This mixture is one developed by

Gong, Luo, Wu, and Zhou [25]. This illustrates one of the major advantages of refrigerant mixtures over their pure refrigerant counterparts: mixtures can achieve equivalent cooling powers at much lower driving pressures.

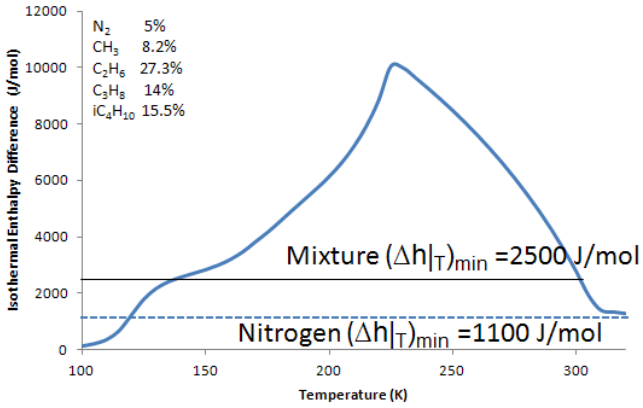

Figure 2.11: Isothermal enthalpy difference as a function of temperature of a refrigerant mixture of Nitrogen, methane, ethane, propane, and isobutane from [25], calculated between a pressure of 2.5 MPa and 0.1 MPa. The minimum isothermal enthalpy difference of the mixture between 300 and 140 K is 2500 J/mol, over twice that for Nitrogen.

2.3.3 Mixture Design

There are a number of methods to design a refrigerant mixture. One of the early methods patented by Alfeev *et al* [26], follows the following steps, as summarized by G. Venkatarathnam [18]:

- First, select the lowest BP component by choosing a refrigerant with a boiling point below the desired refrigeration temperature. This is often Nitrogen, for desired temperatures above 80 K.
- Select the second refrigerant such that its BP is 30 to 60 °C above the previous component, and ensure that its liquid form does not phase-separate from a liquid of the first component. For example, liquid methane (BP=112K) is miscible with nitrogen, and so can be used as a second refrigerant to nitrogen.

- Select the third refrigerant such that its BP is 30 °C above the second refrigerant, and such that it forms an immiscible liquid with the first refrigerant. As mentioned above, liquid ethylene will phase-separate with nitrogen.
- Select a fourth refrigerant that has a higher BP than the third refrigerant, which is also immiscible with the first refrigerant when both are in liquid phase. Propane and butane fit this example
- A fifth refrigerant with an even higher BP is optional.

This method can allow the selection of the components needed for a refrigerant mixture, but does not discuss their compositions. The compositions of several mixtures have been patented.

One method patented by Little [27] chooses refrigerant compositions to ensure the constant-pressure lines corresponding to the high- and low-side pressures of the cooler be parallel on a temperature-enthalpy diagram. Mixtures patented by Alexeev and Quack [28] use compositions that maximized the specific refrigeration effect described by Radebaugh [24] as ($\Delta h_{\min}$). A third method, reported by Gong [29] maximizes the exergy efficiency (η) of the refrigerator, which is given as:

$$\eta = \frac{\Delta h_{\min}}{\dot{W}_c}\left(\frac{T_0}{T} - 1\right) \tag{2.11}$$

Here, W_c is the specific work performed by the compressor. It must be known as a function of the operating pressures, and refrigerant flow-rate. This method is conceptually the same as maximizing the refrigerant's COP, which was discussed first in [24]. In these methods, the suction and discharge pressures of the compressor are assumed to be constant, and treated as a parameter for the mixture optimization. Venkatarathnam recommends allowing the suction and discharge pressures to be selected by the optimization process along with the molar fraction of the components. This process varies molar fraction z_i, P_{scut}, and P_{disch}, in order to maximize the

exergy efficiency (shown above), subject to the following constraints:

- The work by the compressor is less than the maximum compressor power limit: $W_c < W_{c\ max}$
- The discharge pressure is less than the compressor's maximum discharge pressure: $P_{disch} < P_{disch\ max}$
- The pressure loss in the heat exchanger channels is less than some specified amount: $\Delta P_{HX} < \Delta P_{HX,\ specified}$

For micro JT coolers, a refrigerant can be selected first which maximizes $(\Delta h|_T)_{min}$ and the heat exchanger design can be selected to minimize the parasitic losses.

2.3.4 Heat Exchangers with Refrigerant Mixtures

The heat transfer parameter (h_{HX}) governs how long a heat exchanger must be in order to achieve a given effectiveness. For single-phase flow, h can be expressed as $k \cdot Nu/d_h$, where Nu is the Nusselt number, relating the convective and conductive transfers of heat. For laminar single-phase flow, an analytic solution to the equations governing heat and mass flow yield Nu=48/11 for a constant heat flux in circular tubes, and Nu=3.66. In turbulent flow, the Dittus-Boelter equation is often used to find Nu as a function of Reynold's number and Prandtl's Number [30]:

$$Nu=0.023Re^{0.8}Pr^{0.4}$$

In two-phase flow, the heat transfer parameter ($h_{HX,tp}$) can be enhanced, due to the latent heat of evaporation and condensation which occurs within the heat exchanger. Different correlations for Nusselt number and heat transfer coefficient have been derived based on data from various two-phase experiments, and often these correlations differ substantially [31, 32].

One correlation that is often cited was developed by Chen in 1963 [33]. Chen's analysis showed

that a parameter developed by Lockheart and Martinelli for pressure drop in 2-phase systems can be applied to heat transfer in 2-phase systems. Lockheart and Martinelli defined the parameter X_t as the ratio of pressure drop of the liquid phase to the pressure drop of the vapor phase, with each pressure drop calculated by assuming the single phase occupies the entire channel [34]:

$$X_t = \left(\frac{1-x}{x}\right)^{0.9} \left(\frac{\rho_v}{\rho_l}\right)^{0.5} \left(\frac{\mu_l}{\mu_v}\right)^{0.1} \tag{2.12}$$

Here x refers to the mass fraction in the vapor phase. Chen then developed the expression for the heat transfer parameter of 2-phase flow (without nucleate boiling):

$$h_{HX,tp} = h_{HX,l} F(X_t) \tag{2.13}$$

in which $h_{HX,l}$ is the convection heat transfer parameter for the liquid found as $k_l Nu_l/d_h$, F is a multiplier which is a function of X_t, according to: $F=(X_t^{-1}+0.213)^{0.736}$. This functionality was developed as a correlation for experiments with water undergoing nucleate boiling.

There are a number of limitations to Chen's correlation, not least of which is that it does not include any information about the enthalpy change that corresponds to phase change. For mixed refrigerants, such enthalpy change can vary considerably, and will affect the heat transfer parameter. William Little derived an expression for the heat transfer coefficient of a two-phase multicomponent flow under an annular flow regime, which takes into account the enthalpy change of the refrigerant due to phase change [13]:

$$\frac{1}{h_{HX,tp}} = \frac{1}{h_{HX,l}} + \frac{1}{h_{HX,v}} \cdot \frac{x^2 \left(\frac{c_{p,v}}{c_{p,b}}\right)}{\left(\frac{\partial H}{\partial T}\right)_p \cdot \frac{1}{c_{p,v}}} \tag{2.14}$$

This expression for the heat transfer coefficient was compared to data measured by Nelllis, Hughes, and Pfotenhauer [35], and shown to give excellent agreement, when using the Dittus-Boelter expression to find the single-phase heat transfer coefficients, and when the test conditions described by Nellis Hughes and Pfotenhauer yield an annular 2-pahse flow pattern.

2.3.5 Composition Change of Refrigerant Mixtures.

One major concern with refrigerant mixtures is that the compositions can change. For example, oil-lubricated compressors are often used to compress the refrigerant mixture, and the different components will dissolve in the oil at different rates, as Gong et al reported in 2002 [36]. Furthermore, if the refrigeration system has any leaks which are due to chemical diffusion, the different components will diffuse at different rates, causing a composition change. Using non-lubricated compressors with no leaks can circumvent the problem of component dissolution and diffusion, but Gong and others reported in 2008 that a mixed refrigerant can still experience composition change along the length of the heat exchanger due to different amounts of liquid hold-up [35]. Because the mixtures have a different composition in the liquid and vapor phase, if the two phases travel at different flow-rates, the resulting mass flux of each component will not be the same. Gong's report compared the measured composition along the heat exchanger with one predicted with liquid hold-up model:

$$z_i'' = \frac{nz_i - \Delta n z_i'}{n - \Delta n} \tag{2.15}$$

$$\Delta n = \left(V_l + \frac{\dot{V}_l}{\dot{V}_{tot}} V_{tot}\right) \rho_n \tag{2.16}$$

where $\dot{V}$ refers to volumetric flow-rate, the subscript *tot* refers to the pipe volume or total 2-phase flow-rate, and ρ_n is the molar density of the liquid. The measured composition changes were up to a factor of 3 higher than those predicted with this model.

Reddy, Murthy, and Venkatarathnam developed a method to determine the optimal refrigerant composition when charging a MR-JT system, which will give the desired optimal refrigerant composition when the system is running [38]. They noted that their models require information about liquid holdup of multi-component refrigerant mixtures, which are generally not available for the geometries experienced by cryogenic heat exchangers. They therefore

suggest an iterative method to solve an inverse-problem with limited information.

2.4 Micro Joule-Thomson Cryogenic Coolers.

2.4.1 Previous work with Micro Joule-Thomson Cryogenic Coolers

The first MCC was developed by W. Little at Stanford University in 1980. He used photolithography to etch a serpentine heat exchanger and a J-T throttle in a glass wafer. The cooler measured 60mm x 14mm x 2mm and demonstrated cooling of 250 mW at 83K using N_2 as a refrigerant [39]. The cooler took a pressure of over 10 MPa to operate, supplied from a pressurized nitrogen bottle. The low-pressure Nitrogen was vented. Little went on to form the company Micro Miniature Refrigerator Technologies (MMR). In the 1980s and 1990s, MMR improved the design of Little's MCC and continued to shrink the coolers. One such cooler measured 15 mm x 3 mm, with a J-T restrictor 200μm, and had a cooling capacity of 25 mW at 88 K with 12.7 MPa of pure N_2 at a flow-rate of 100-200 sccm [40]. This cooler used serpentine channels with a depth of 20 μm and width 50 μm for the high-pressure side of the HX. The serpentine geometry allowed the high-pressure channel to be 4.8 cm in length, and maintain flow in a turbulent regime. A serpentine, turbulent-flow low pressure channel would cause a large pressure drop between the evaporator and vent, which would cause the evaporator to be at a pressure well above atmospheric, and increase the boiling point of the nitrogen refrigerant. In order to reduce this effect, the low-pressure channel was 1.5 mm wide and straight, and experienced laminar flow. MMR also used a mixture of gasses (composed of nitrogen, hydrocarbons, and 'Halon' CF_3Br) to increase the cooling capacity by a factor of 10 and decrease the cooling time required for their MCC also by a factor of 10, compared to pure Nitrogen [41]. Such coolers are available commercially, and one is shown in Figure 2.12a.

More recently, Ameel *et al*. at the University of Utah attempted to fabricate a MCC using a LIGA process and a polymethylmethacrylate (PMMA) mold to form a serpentine heat exchanger [42]. However, this work was never completed, demonstrating that micromachining of silicon and glass is more successful for MCC development than LIGA with PMMA.

The Micromechanical Transducers Groups at the University of Twente developed the next MCCs. In 2001, Burger *et al.* developed a thermoelectrically pre-cooled MCC which used coaxial capillaries as a heat exchanger. The capillaries are horizontally coupled into the J-T coldhead and held in place with epoxy. After one heat exchanger, the refrigerant is pre-cooled with a thermoelectric cooler. The refrigerant used in these studies was Ethylene, compressed to 2 MPa with a small-scale sorption compressor, or supplied by a high-pressure bottle. In the case of the sorption compressor, the suction pressure of the compressor is 0.1 MPa. The dimensions of the coldhead were 9mm x 9mm x1.1 mm, and the J-T restrictor was 1.1 μm wide [43, 45]. Temperature fluctuations in this device were noted when the refrigerant returning from the evaporator experienced unsteady two-phase flow. The MCC is shown in Figure 2.12 b.

The MCC currently being developed by the University of Twente is composed of 3 etched glass plates. Heat exchanger channels are etched into the plates which do not follow a serpentine pattern. The design of this heat exchanger was optimized to minimize net entropy generation rather than by considering the sum of refrigeration losses [45]. The J-T restrictor valve is 300nm. After the J-T restriction, there is an evaporator region. The refrigerant used with this MCC is pure nitrogen, compressed by a sorption compressor which has a 16:1 compression ratio. The suction pressure of the compressor was 0.5 MPa, which gave a compressor outlet pressure of 8 MPa. The low temperature of the MCC is governed by the evaporator, which for 0.5 MPa with Nitrogen is 93 K; however pressure losses in the low-pressure side of the heat

exchanger cause the pressure at the evaporator to be roughly 1.1 MPa, giving the Nitrogen a boiling temperature of 105 K. The MCC is shown in Figure 2.12c.

Due to the sub-micron J-T valve height, icing was noted as a problem in this MCC [46]. Although all of the coupling lines were evacuated prior to charging the MCC, the low pressure air that persists in the evacuated lines contains some amount of water vapor. After the lines were charged with pure nitrogen, some water vapor existed with some small partial pressure. When the MCC was running, solid ice would form at the cold-tip if the cold-tip temperature dropped below the deposition temperature of the water at its partial pressure. As the refrigerant flowed past the iced cold-tip, more water would fall out of solution from the refrigerant and deposit on the cold-tip. Eventually, the ice would fill the passage and drop the flow-rate. The depressed flow-rate caused the temperature of the cold-tip to rise, eventually melting some of the ice and allowing the flow-rate to increase. Eventually a partially-clogged J-T valve would allow steady flow-rates of less than half the initial value.

As was mentioned in Chapter 1.4, previous work by our group has demonstrated a fiber-based MCC with a 760 μm tall J-T valve for cooling to 77 K using refrigerant mixtures. This and the other previously developed MCCs are compared in Table 2.2, and Figure 2.12.

Reference	Year	High Pressure (bar)	Refrigerant	Cooling Power (mW)	Minimum Temperature (K)	Dimensions of heat exchanger and J-T valve (mm)
Garvey [2.25]	1983	100-200	N_2	25	88	0.25 x 45 x 45
Paugh [2.26]	1990	100-300	Mixture: N_2-hydrocarbon	370	70	0.25 x 45 x 45
Burger[2.28]	2001	20	Ethylene	200	168	1.1 x 9 x 77
Lerou [2.29]	2005	80	N_2	25	105	0.5 x 2.2 x 30
Lin [2.31]	2009	16	Mixture: N_2-hydrocarbon	3	77	2 x 2 x 25

Table 2.2: comparison of 5 previously developed MCCs.

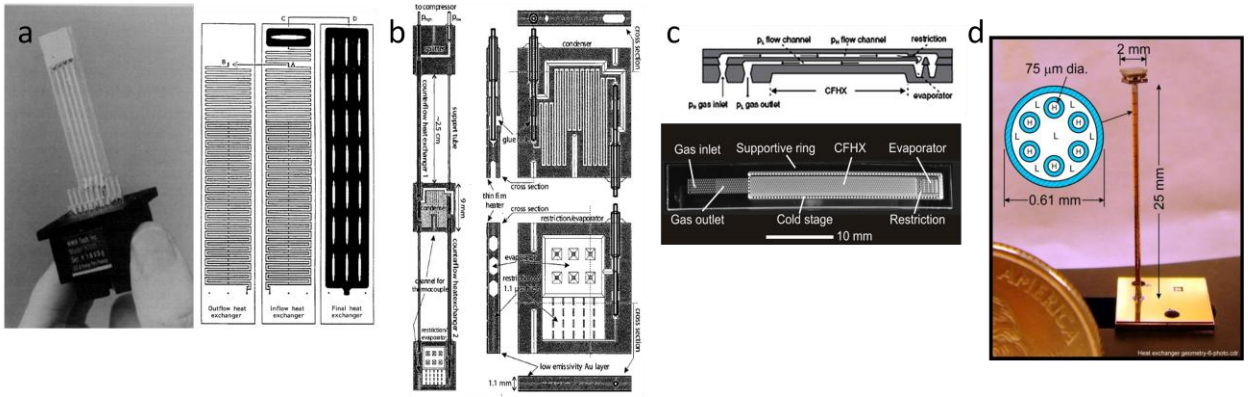

Figure 2.12: Review of previously developed J-T MCCs. a) The fully packaged and commercially available MCC by MMR and the etch-pattern of its serpentine HX, reprinted from [41], with permission by Elsevier. b) The 2-stage pre-cooled MCC developed by Burger, reprinted from [43] with kind permission from Springer. c) The 3-plate MCC developed by Lerou, reprinted from [45] with permission from Elsevier, and d) the fiber-based MCC developed by Lin [13].

2.5 Conclusions

This chapter covered the history and thermodynamics of Joule-Thomson coolers. The principles of heat transfer in Joule-Thomson coolers can be used to optimize the length of the heat exchanger. History and thermodynamics of refrigerant mixtures are introduced as well and used for refrigerant mixture design optimization. This chapter also gave a review of previous JT MCC development. All of the previously developed MCCs have used either a large high-pressure refrigerant supply bottle or a larger compressor to drive them. Work with refrigerant mixtures for low-pressure operation with a micro or miniature compressor has not been reported, but is necessary for the development of small scale complete systems. The development of such a small scale system will be the subject of the next chapter.

CHAPTER 3: EXPERIMENTAL SETUP AND DEMONSTRATION OF LOW-PRESSURE JOULE THOMSON MICRO COOLING

This chapter covers the experimental setup used to demonstrate cooling to low temperatures with a Joule Thomson Micro Cryogenic Cooler, coupled to a miniature compressor. The assembly of the micro cryogenic cooler will be discussed in detail in Section 1. Assembly and characterization of our miniature compressor will be presented in Section 2. Four refrigerant mixtures are designed and tested in this chapter. The mixtures will be discussed in Section 3. Section 4 will cover the test set-up when all of the components are combined, and Section 5 will show the results of the cool-down test for each refrigerant mixture. In addition to the four refrigerant mixtures, two pure hydrocarbon refrigerants are tested. The MCC behaves as expected when using pure hydrocarbon refrigerants, but each mix has less-than-calculated cooling performances. When cooling with a mixture, the refrigerant first experiences steady flow and low cooling power, then experiences pulsating flow which may accompany enhanced cooling power.

3.1 Micro Cryogenic Cooler

The MCCs used in these tests were designed by Lin [16], and shown in Figure 3.1. As in the previous tests with fiber-based MCCs [21], the counter-flow heat exchanger (CFHX) is composed of hollow-core glass fibers held within a glass capillary, and the J-T expansion valve was formed with etched silicon and borosilicate glass chips (see chapter 1.4). Compared to previous studies however, the current tests use considerably lower driving pressure. In order to maintain the same flow-rate with a 25% of the initial pressure drop across the J-T valve, the fluidic resistance of the J-T valve needs to decrease. This corresponds to increasing the gap

between the silicon and glass chips to from roughly 0.7 μm to 1.5-1.8 μm (determined experimentally).

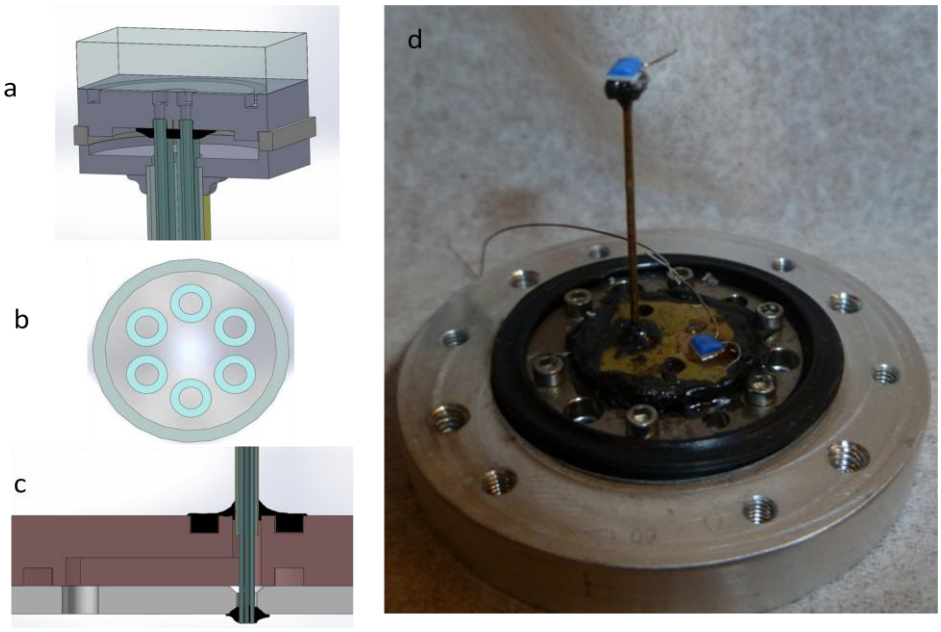

Figure 3.1: CAD and photograph of the MCC used in these studies. a) cut-section of the J-T valve; b) cross-section of the CFHX, with high-pressure refrigerant in the 6 fibers and low-pressure refrigerant in the interstitial space between the fibers within the capillary; c) cross-section of the macro-coupler where the high- and low-pressure streams are diverted, allowing the MCC to interface with the micro compressor; d) photograph of a completed MCC.

The micro-fabrication of the silicon J-T valve chip is summarized in Figure 3.2. It relies on growing and patterning SiO_2 layers on the chip, and using those SiO2 layers as masks for a deep reactive ion etching (DRIE) process to form channels in the silicon. Photo-resist (PR) is used as a mask for etching the SiO2 as well as for a lift-off process to pattern a metal-coating [21].

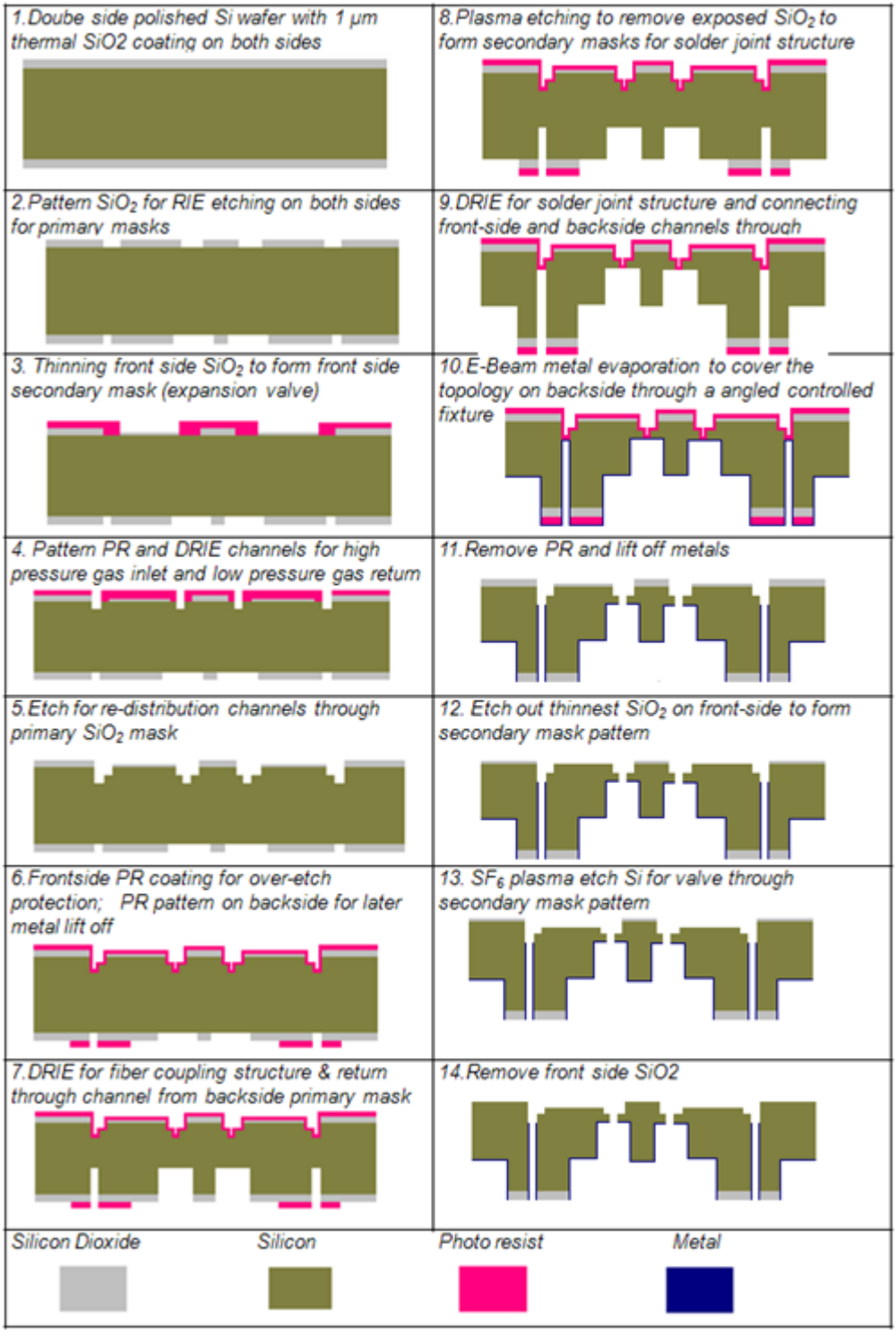

Figure 3.2: J-T valve fabrication process flow. From [21].

Only the last 2 steps define the J-T valve gap thickness, and they can occur after wafer

dicing. Therefore, a single wafer can supply J-T valve chips of varying thickness, both in the sub-micron range suitable for the previous studies, and the 1.5-1.8 µm range suitable for this study.

The silicon valve chip is anodic-bonded to a borosilicate glass chip to form the J-T valve. The procedure for anodic bonding is summarized in 4 steps: First, the silicon and glass chips are ultrasonically cleaned in an acetone bath followed by an alcohol bath. Second, the bonding faces of the two chips are cleaned in an oxygen plasma (at 1 Torr). Third, the two chips are aligned under a microscope and sandwiched between 2 electrodes on a hot-plate, which heats to 400 °C over the course of 25 minutes. Finally, a voltage of 550 V is applied to the silicon chip, while the glass chip is kept at ground, as in Figure 3.3a. This voltage is applied for 30 minutes. Anodic-bonding is often described as a hermetic sealing technique [48], but at these voltages, some surface roughness can induce a defect which can lead to a liquid leak in the bonded area between the glass and silicon, as in Figure 3.3 c. Epoxy is applied to the outer perimeter of the silicon-glass interface, to re-enforce the seal.

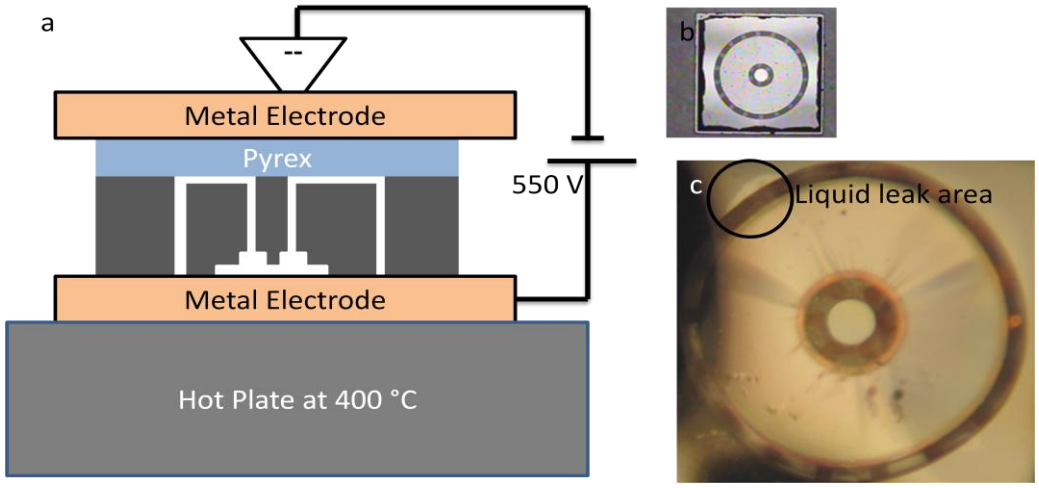

Figure 3.3: a) Anodic bonding of J-T silicon chip to Pyrex cap, b)completed valve, after bonding, c) J-T valve in operation, showing a leak of liquid into the bonded area.

The glass channels used to assemble these MCCs are Flexible Fused Silica Capillary Tubing

from Polymicro Technologies. Both fiber and capillary come as a long spooled tube. The glass is initially coated with a Kapton™ film roughly 25 μm thick, which prevents cracks from propagating in the spooled tubing. The fibers and capillary are cut to 30 mm in length, and then placed in an oven at 600 °C for 2 hours to bake off the polymer coating. The capillaries are subsequently placed into a segmented fixture, and exposed to an evaporated layer of Titanium (seed layer), Copper and Gold, as described in [16], and shown in Figure 3.4. The final gold layer acts as a radiation shield and helps reduce the parasitic heat loads associated with radiative heat transfer. Once coated, the capillaries are polished to a final length of 25 mm.

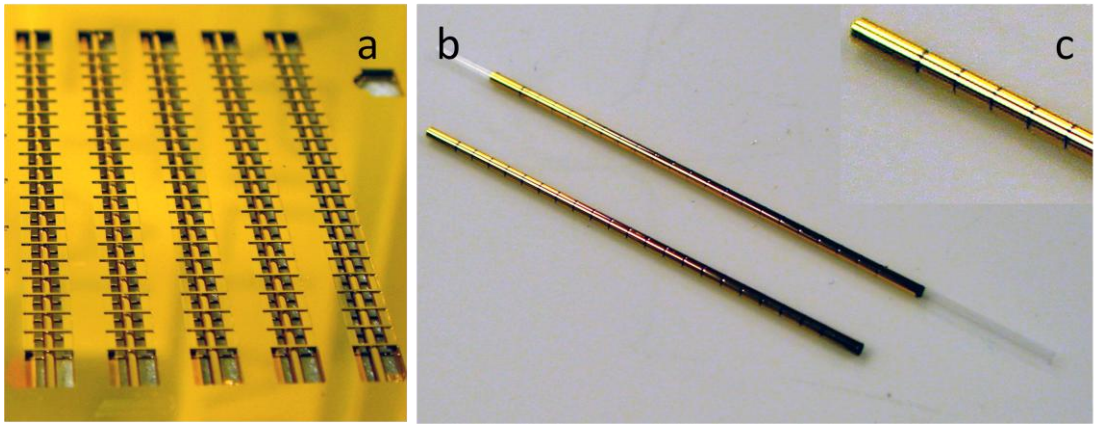

Figure 3.4: capillaries with segmental radiation shield. a) Fibers in shutter mask to evaporate metal in segments, b) capillary removed from shutter mask, and polished, c) close-up of capillary showing segments. Image from [16].

The MCCs of the previous studies were assembled using solder to couple the fibers and capillary to the J-T valve chip. In the present studies, which must withstand lower internal pressures, epoxy coupling is sufficient. A very thin layer (50-150 μm thick) of Stycast 2850 FT is coated by hand to each fiber at one end, taking care that no epoxy coats the internal channel of the fiber. The fibers are then placed into the 6 high-pressure channels in the J-T valve chip. The other ends of the fibers are held within a radius of 500 μm while the epoxy cures. Once cured, a micro-coupler chip is slid over the fibers and epoxy-bonded to the J-T valve chip, taking care

again not to fill the internal channels with epoxy. Finally, a capillary is polished to 25 mm in length, placed around the fibers, and epoxy-bonded to the micro-coupler chip. The assembly process is shown in Figure 3.5.

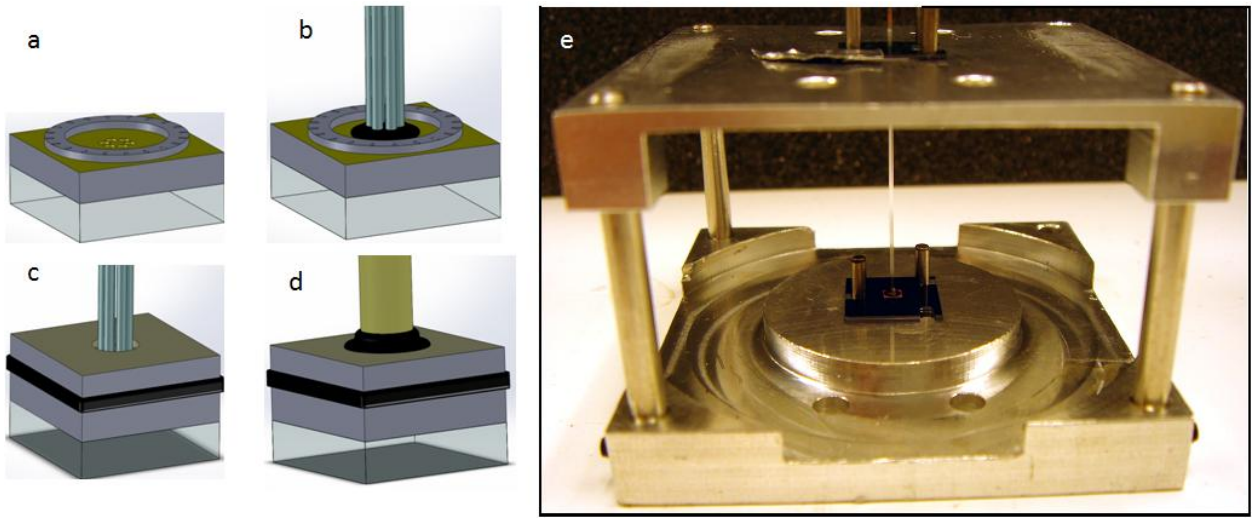

Figure 3.5: Assembly process for the CFHX: starting with the J-T valve chip and bonded glass cap (a), 6 epoxy-tipped fibers are inserted into the fiber-holes (b); after curing, a micro-coupling chip is epoxy-bonded to the J-T valve-chip (c); and a capillary is epoxy-bonded to the micro-coupling chip (d). A photograph of the fixture used to hold the fibers while curing is shown in (e). Modified from [16].

The high-pressure fiber and low-pressure capillary channels interface with the larger world through a macro-coupler, shown in Figure 3.6. The macro-coupler is composed of two thin disks of machined stainless steel. The bottom disk contains two through-channels, and a larger bolt-pattern around the outer perimeter. The top disk contains a low-pressure channel, and solder groove. Lead-Tin 63-37 solder is filled into the groove, which is soldered onto the bottom disk. Two pins are used to ensure the channels of both disk are aligned. Solder is then flown along the outer perimeter of the top disk to ensure sealing. The completed macro-coupler has one through-hole and one diverted channel. The fibers of the MCC are placed through the through-hole, and the outer diameter of the capillary is epoxied to the top disk. When cured, the perimeters of the fibers are sealed with epoxy as well. Finally, the alignment pin holes of the two disks are sealed

with epoxy.

The completed MCC is bolted onto a base-plate flange, shown in Figure 3.6 c. Sealing between the base-plate channels and the macro-coupler channels is facilitated with O-rings. The flange allows the MCC to be tested in a small vacuum package.

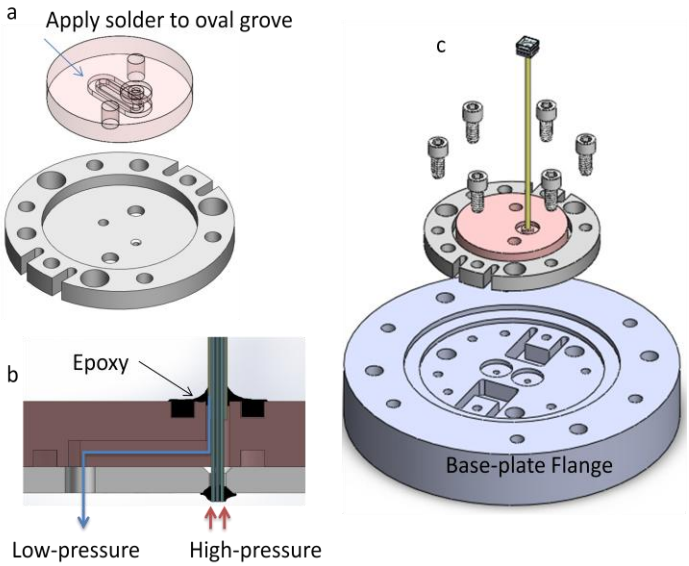

Figure 3.6: Drawings of the macro-coupler assembly process. a) Solder is applied to the oval grove on the bottom-side of the top-disk. The complete disk assembly contains 1 through-hole and 1 internal channel. b) The complete disk-assembly is epoxy-bonded to the capillary on top and fibers on bottom to isolate the high-and low-pressure streams. c) The complete MCC assembly is bolted to a base-plate flange.

Before testing with refrigerant, the MCC is checked for leaks and clogs. To check for leaks, the MCC is immersed in alcohol and both high- and low-pressure channels are charged with Nitrogen to some positive pressure. Any leaks will lead to bubbles in the alcohol. To check for clogging, the MCC is subjected to a blow-by test, where the high-side of the MCC is connected to Nitrogen at some pressure, and the low-side vented to atmosphere. The flow-rate through the MCC is monitored at different pressures.

3.2 Miniature and Micro Compressors

Miniature compressors have proved to be an ongoing problem for micro Joule-Thomson systems. Burger gives an excellent review of potential MEMS technologies that can be used for micro compressors [49]. The final compressor Burger developed a sorption-type compressor which utilized MEMS-based check valves (See chapter 6 of Ref [49]). Each sorption cell measures 10 cm in length and 2 cm in diameter, and several cells are used for a complete compressor. This is considerably smaller than the macro-scale piston compressor used in [16], but still not small enough for a micro or miniature scale system

Simon reported a MEMS-based micro/miniature compressor which used micro check valves, and a piezoelectric stack actuator to oscillate a membrane by 20-30 μm [50]. The maximum pressure ratio reported for this device was 7:1. However, the performance of this compressor relied heavily on the assembly of each component, and repeatability was a major issue. After the 7:1 performance, the highest pressure ratio reached was 1.2:1, shown in Figure 3.7.

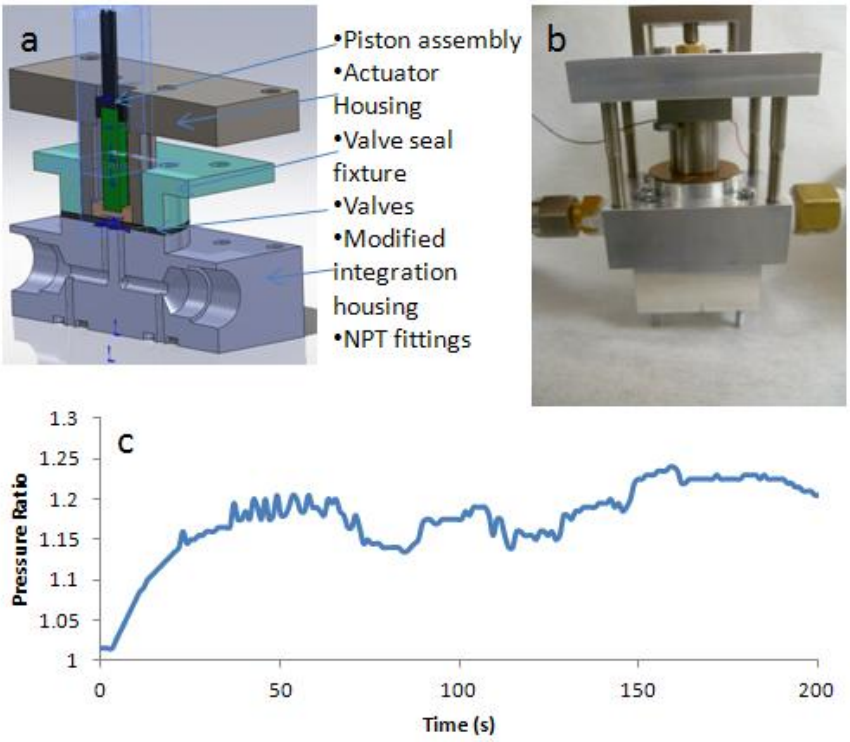

Figure 3.7: Performance using a micro-miniature compressor, using the design developed by Simon [50], but assembled by the author: a) CAD drawing of the design, b) photograph of the assembled micro-compressor, and c) performance. Although a 7:1 pressure ratio was reported in [50], the highest pressure ratio with repeatability was 1.25:1. Improvements to the design are discussed in Chapter 6.

Other micro compressors have been fabricated using MEMS technology [41-53]. For example, a piezoelectric bimorph was used as a membrane coupled to silicon micromachined check valves, to demonstrate a pressure ratio of 1.12:1 [53].

Companies which build small Stirling coolers must also build small piston oscillators for them. Two common methods are linear and rotary piston oscillators. In linear compressors, a piston head is coupled to a linear magnetic actuator. Friction between the sleeve and piston must be reduced, for example by coating the piston in a low-friction fluorinated polymer. Rotary compression oscillators use a small DC brushless motor to drive the piston.

3.2.1 Rotary Mini-Compressor

The compressor used in this study is based on a commercial rotary compression oscillator. The oscillator is made by FLIR Systems for their MC-3 Stirling cooler [54], and has been modified into a compressor by our group. The rotary oscillator drives a crank-shaft, which is connected via a flexure to the piston. The piston is coated in polytetrafluoroethane (PTFE) as a friction-reduction layer. Once the piston has been coated, a piston sleeve is fabricated such that the inner diameter of the sleeve matches the outer diameter of the coated piston to within 2.5 μm (1/10,000”). If the gap is too large, there will be a housing leak between the compression space and the backside of the piston. The piston sleeve also includes an internal channel which connects the piston oscillating volume with the Stirling regenerator. The stroke length of the piston is 2 mm, with a piston-head area of 1.5 cm^2, for a total volume of 0.3 mL per stroke. The electronics of the motor allowed it to operate at two frequencies: a “high” frequency of ~60 Hz and a “low” frequency of ~8 Hz.

To modify the piston oscillator into a compressor, first the connecting channel in the piston sleeve was filled with a silicone coated steel dowel, to eliminate the dead volume associated with that channel. Then the piston oscillating volume was connected to a pair of check valves, which rectify the oscillating pressure (analogous to electrical alternating current) to static pressure (analogous to electrical direct current). The check valves are formed micro-patterning an “L” tether design onto a 50 μm thick sheet of Kapton™ using an RIE process. UV laser cutting has also been employed for the micro-patterning. A second through-hole is also patterned into the Kapton film. A stainless steel substrate 1 mm thick is prepared with two through-holes (0.5 mm in diameter), one of which has a 7 μm tall ring around the perimeter. Electroplated Copper and SU-8 have both been used as the ring material. Two tape-based masks protect the

through-holes while a 10 μm adhesion layer of polyimide is spin-coated onto the disk. The patterned Kapton film is placed over substrate and adheres as the polyimide layer is cured. In this manner, the square in the center of the "L" pattern seals against the ring material.

The process is repeated with a second Kapton film on the other side of the substrate. The finished check valve is shown schematically in Figure 3.8 a and photographically in Figure 3.8 b. The sealing and open-flow characteristics of the valves were characterized with a blow-by test, in which flow-rate is measured as a function of pressure drop across the valve. In an "open" state, the flow-rate is 1500 sccm/bar, and in a "closed" state, the flow-rate is 30 sccm/kPa, as shown in Figure 3.8 c. Because these valves are fabricated to have a 3 μm gap between the sealing ring and the Kapton, some pressure will be required to seal the valve, but that pressure was smaller than could be resolved in these characterization tests.

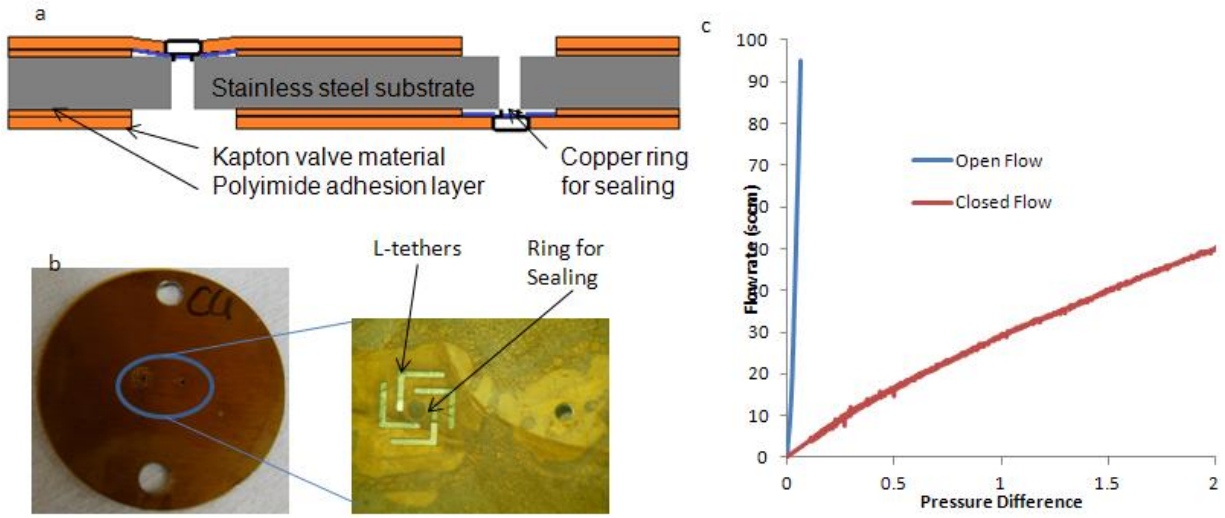

Figure 3.8: a)cross-sectional schematic of Kapton-based check valves, b) photograph of completed check valves, with zoom showing L-tethers and ring for sealing, c) flow-rate characterization of one of the check valves. Adapted from [56].

To couple the check valves to the piston oscillator, an aluminum mating fixture was fabricated with two through-holes. On the piston-coupling end, the fixture had a recess for the piston-sleeve and a sealing O-ring, and the center of the recess was raised by 50 μm such that the

piston would reach the end of the coupler at its maximum stroke. Any gap between the piston and fixture would constitute a dead volume and deteriorate the compressor performance. On the valve-coupling end of the fixture, the through-holes ended in groves for size 001-1/2 O-rings, which have inner diameters just large enough not to cover the “L” tether pattern. The assembled compressor is shown in Figure 3.9a and b. The valves interface with a valve housing to couple to the MCC and charge/purge lines to the compressor, shown in Figure 3.9c.

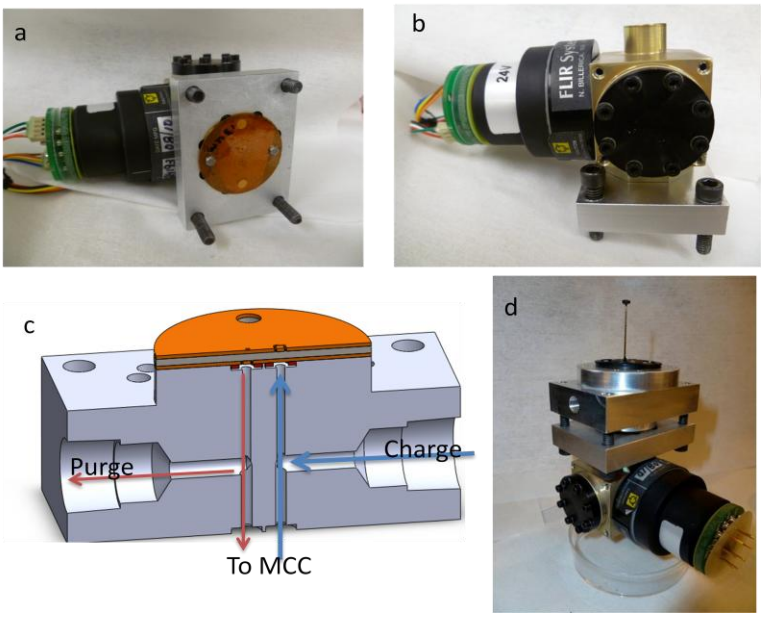

Figure 3.9: a) and b) Photograph of the piston oscillator and coupling fixture to the check valve assembly. c) Valve housing to couple the compressor to the MCC or purge and charge lines. d) photograph of a fully assembled MCC and compressor assembly.

The compressor performance was characterized in terms of pressure generated and flow-rate, using room-temperature Nitrogen regulated pressure of 0.100 MPa at the suction port of the compressor. The pressure-vs.-flow-rate curves are plotted in Figure 3.10 for both the high-frequency and low frequency. In refrigeration systems, the compression of a refrigerant will add heat to the system, which must be removed in an after-cooler. For flow-rates in the range of 10-30 sccm, that after-cooling will take place in the aluminum valve housing on the other side of the

valves, as modeled numerically for the first two points of pressure and flow-rate during high-frequency operation, in Figure 3.10c-d. The temperature of the nitrogen entering the after-cooler channel is calculated as the temperature achieved with isenthalpic compression from an initial pressure of 0.100 MPa to a final pressure of P_f. For an ideal gas, this is given by $T_2=T_1(P_2/P_1)^{(k-1)/k}$ where k is the ratio of specific heats: C_p/C_v (k=1.4 for Nitrogen in the temperature range of interest). This is an over-estimate of the temperature that the compression of gas will produce; in a real system some of the heat will transfer out of the compression volume and reduce the temperature.

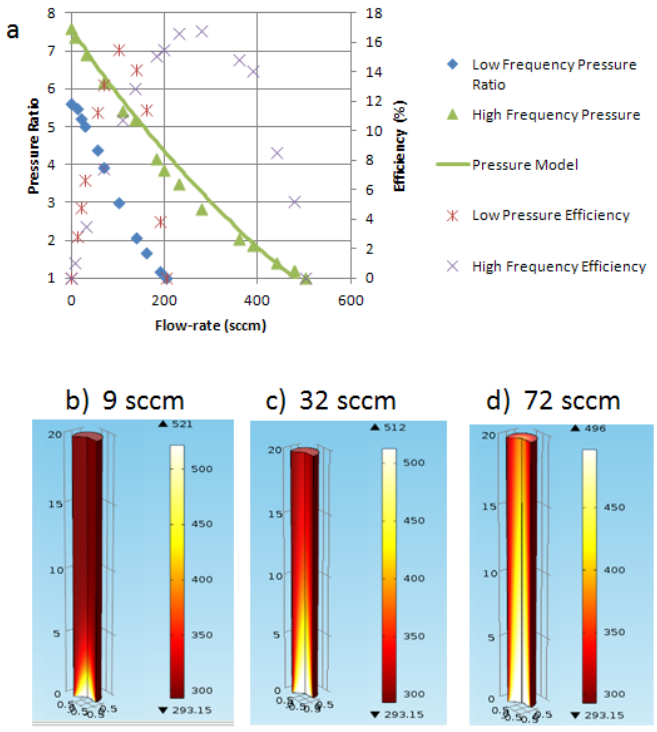

Figure 3.10: a) Measured values of pressure and flow-rate, as well as the corresponding efficiency of compression at low- and high-frequency. b-d) Contours of temperature in the 20 mm long Valve Housing channel, showing that sufficient after-cooling will occur there for flow-rates below 30 sccm. The temperatures and flow-rates correspond to isenthalpic heating of the first 3 non-zero data points of high-frequency operation.

The useful power that can be pulled from such a compressor and after-cooler system is the change in Gibb's free energy: $P_{flow} = \dot{n}\Delta g$. For an ideal gas, the change in Gibb's free

energy is given by: $RT \ln (P_{disch}/P_{suct})$. The compressor efficiency is then given by:

$$\eta = RT \ln\left(\frac{P_{disch}}{P_{suct}}\right) / Power \tag{3.1}$$

For this piston oscillator, power draw depends only on the suction pressure and oscillation frequency. At low-frequency with a suction pressure of 0.100 MPa, the power draw is 1.22 W, and at high-frequency with a suction pressure of 0.100 MPa the power draw is 3.12 W. The efficiency of the compressor at high- and low-frequency is plotted in Figure 3.10 as well.

It is found with this compressor that the power drawn is independent of pressure ratio, but strongly dependent on suction pressure, as shown in Figure 3.11 a. The pressure difference can therefore be changed by adjusting the suction pressure while maintaining a given pressure ratio. However, with the flexure-driven piston care must be taken to ensure that the pressure difference between the piston backside and compression area is below 0.7 MPa; otherwise the flexure will be overstressed and may fracture, as shown in Figure 3.11 b.

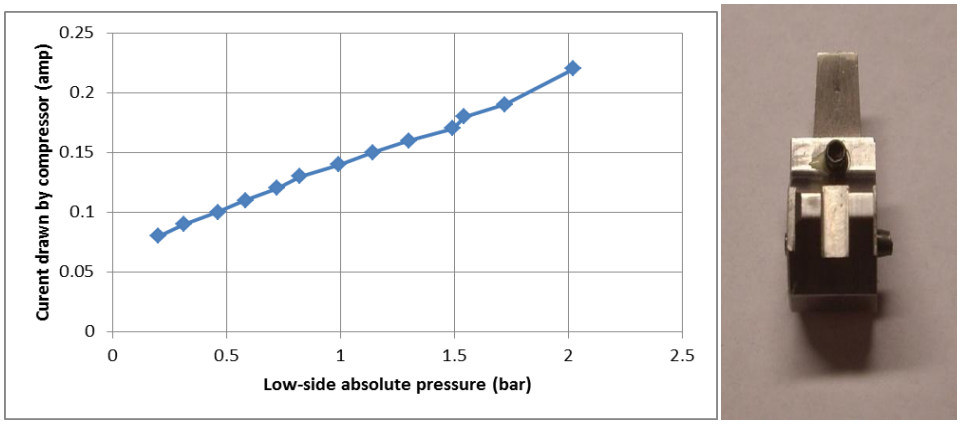

Fiugre 3.11: Current drawn by compressor as a function of low-side pressure, at a constant voltage of 24 V, and photograph of flexure that fractured along its top edge.

Such a compressor system can be modeled as well with a simple model of conservation of mass in the compression volume. One can consider the number of moles of gas in a control volume consisting of the compressible space. Gas can escape through the inlet valve, the outlet

valve, or as a leak past the piston, as shown in Figure 3.12a. These leak rates are functions of the pressure difference between internal pressure and low-side pressure, internal pressure and high-side pressure, and internal pressure and ambient pressure, respectively. This is represented mathematically in Equation 3.2.

$$\frac{\mathrm{d}n}{\mathrm{d}t} = \dot{n}_{out}\left(P - P_{high}\right) + \dot{n}_{in}(P - P_{low}) + \dot{n}_{leak}(P - P_{amb}) \tag{3.2}$$

The internal pressure can be found by invoking the ideal gas law *P(t)=n(t)R T/V(t).* In this model, the volume oscillates as a sinusoid between a minimum value of V_{dead} and a maximum volume of V_{dead}+0.3 mL, with a frequency of 60 Hz. The dead volume can therefore be a parameter used to allow the model to match the data. The dead volume will be minimized when the piston just touches the aluminum coupling fixture, where the value of V_{dead} will be given by the volume of the through-holes in the fixture: 0.0055 mL. A maximum dead volume will occur when the piston is poorly aligned with the fixture. The maximum misalignment we would expect is 150 μm, giving a dead volume of 0.0225 mL. We will therefore expect the dead volume to be between 0.006 and 0.028 mL.

The inlet and outlet leak rates are determined by the performance of the valves. The leak rates through the valves and across the piston are measured to be linear with pressure difference in the flow-rates of interest, with values as follows:

$$\dot{n}_{valve} = \begin{cases} 300\frac{sccm}{MPa} \cdot \Delta P & \text{for } \Delta P < 0 \; ie \text{ valve is closed} \\ 15000\frac{sccm}{MPa} \cdot \Delta P & \text{for } \Delta P > 0 \; ie \text{ valve is open} \end{cases} \tag{3.3}$$

$$\dot{n}_{leak} = 300\frac{sccm}{MPa} \cdot \Delta P \tag{3.4}$$

Equations 3.2-3.4, and the ideal gas law form a set of coupled ordinary differential equations, which can be integrated numerically to find the total flow-rate as a function of high-side pressure

when low-side pressure is kept at 0.100 MPa. With the measured leak rates, one arrives at the solid line in Figure 3.10a, which agrees well with the measured values with a dead volume of 0.025 mL.

One can use this model to investigate the effects of valve and piston leakages. The pressure vs. flow-rate curves for a hypothetical compressor with leak-free piston (but valves which experience back-flow leakages), and one with ideal valves (but a piston which experiences blow-by leaks), are plotted in Figure 3.12b. Their efficiencies are plotted as well in Figure 3.12c, under the assumption that the power input is 3.12 W. From this plot we can tell that although piston blow-by does hinder the performance, improving the valves can more drastically improve the compressor. With improved valves, compressor efficiencies of 23% are possible.

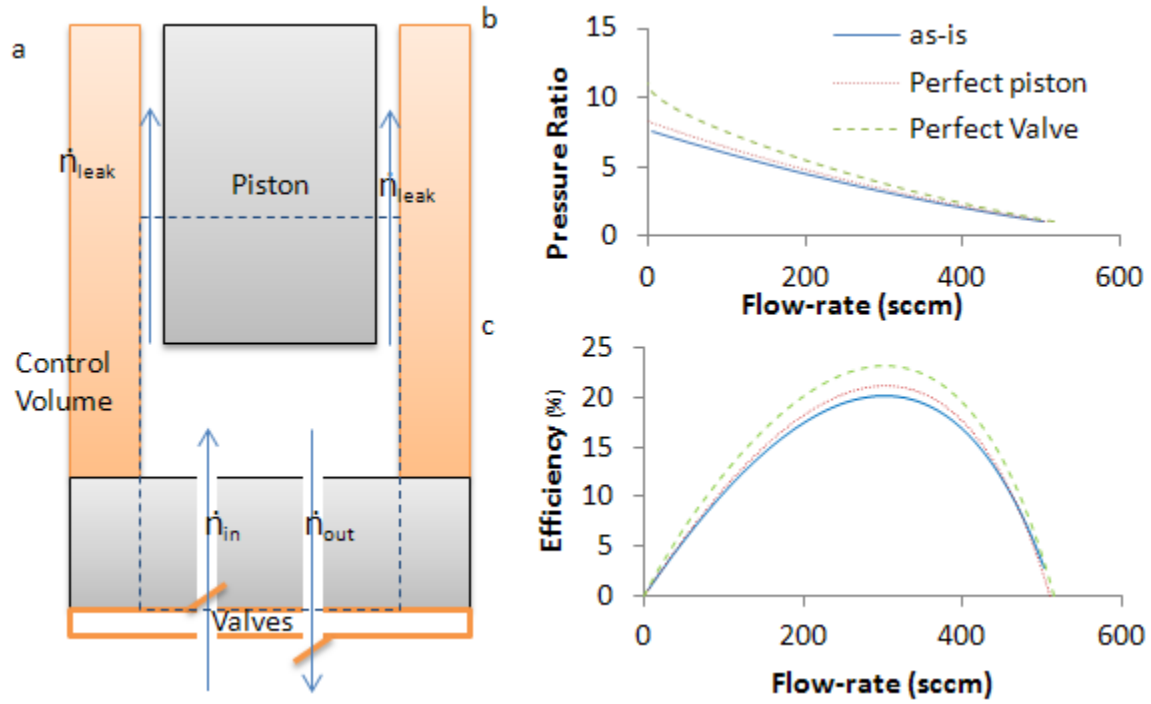

Figure 3.12: a) control volume used to analyze compressor performance with respect to valves and piston leakages. b) pressure ratio and c) efficiency as a function of flow-rate. Adapted from [53].

This model assumes isothermal operation of the compressor, which occurs when a

maximum amount of heat is transferred from the compressor to the environment. A second way to model the compressor assumes no heat is transferred to the environment during compression. In that situation, both a conservation of mass and conservation of energy must be applied to the control volume in Figure 3.10. Under such a formulation, the pressure can be expressed as [56]:

$$\frac{dP}{dt} = \frac{kP}{\rho V}(\dot{n}_{in} - \dot{n}_{out} - \dot{n}_{leak}) - \frac{kP}{V}\frac{dV}{dt} \tag{3.5}$$

Here, *P, k, V, ρ, t,* and $\dot{n}$ are the pressure, specific heat ratio, volume, molar density, time, and molar flow-rate, respectively. Using this model and the same measured values of valve and piston flow-rates, one can fit the model to the measured data with a dead volume of 0.056 mL. In actual operation, some heat will be transferred during a compression cycle, so the actual dead volume is between 0.025 mL and 0.056 mL. Using the isentropic model to find the effects of reducing piston and valve leak rates yields the same results.

Note from Figure 3.9 that the compressor can provide pressure ratios of up to 7:1 with flow-rates near 10 sccm. However, the efficiency of such operation is quite low. The maximum efficiency occurs when the pressure ratio is 3:1, with a flow-rate of 270 sccm.

It should also be noted that this model is developed and verified based on an ideal gas. The refrigerant mixtures in a J-T refrigerator are not ideal, and have some compressibility Z=nRT/PV less than one. This will decrease the performance of the compressor.

3.3 Refrigerant Mixtures

Four refrigerant mixtures were designed according to the method described in Chapter 2.3.3. These mixtures were designed to cool from 300 to 140 K (Mix 1), 275 to 140 K (Mix 2), 300 to 160 K (Mix 3), and 300 to 200 K (Mix 4), with a high-pressure of 0.4 MPa and a low-pressure of 0.1 MPa. The compositions of each of these mixtures are listed in Table 1. In addition, 2 pure

hydrocarbons (propane and iso-butane) are used to verify the operation of the MCC test set-up.

	Design Composition (mol fractions)	Actual composition (mol fractions)		Design Composition (mol fractions)	Actual composition (mol fractions)
Mix 1 "140K Mix"	34% methane 20% ethane 18% ethylene 16% isobutane 12% isohexane	34.2% methane 19.8% ethane 15.2% ethylene 14.9% isobutane 15.9% isohexane	Mix 3 "160K Mix"	24% methane 36% ethylene 14% propane 10% isopentane 16% pentane	24.1% methane 36.0% ethylene 14.0% propane 10.0% isopentane 15.9% pentane
Mix 2 "275K Mix"	34% methane 22% ethane 20% ethylene 12% isobutane 12% isopentane	33.9% methane 22.0% ethane 20.0% ethylene 12.0% isobutane 12.1% isopentane	Mix 4 "200K Mix"	8% methane 46% ethane 14% propane 4% butane 28% pentane	7.93% methane 45.88% ethane 14.0% propane 3.99% butane 28.2% pentane

Table 3.1: Composition of 4 refrigerant mixtures used in this test.

The parasitic losses of the 4 mixtures in the MCC fiber-based heat-exchanger is plotted in Figure 3.13, as calculated by the method described in Chapter 2.2.2. Thermophysical properties of the mixtures are calculated by REFPROP, and a mass-averaged method is used to calculate the pressure-drop. The temperature range used is that specified for each mixture, and the flow-rate used in the calculation was 30 sccm. Note that the largest parasitic load is due to heat exchanger ineffectiveness for fiber lengths <35 mm. At a heat exchanger length of 25 mm, the fractional parasitic loads are all <30%, well below the maximum acceptable fraction of 60%. Indeed, according to this analysis, the heat exchanger could be shortened to as low as 4 mm, in the case of Mix 4.

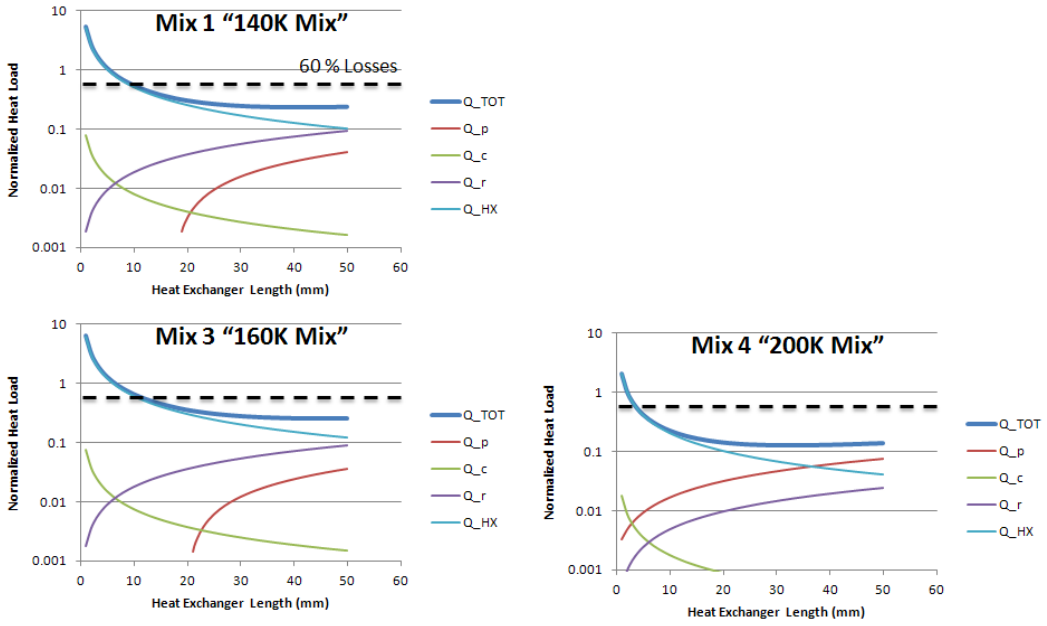

Figure 3.13: Calculated heat loads for the 3 refrigerant mixtures with a warm-end temperature of 300 K.

The refrigerants will be tested with both an ambient warm-end and with an ice pre-cooled warm end, so the parasitic losses are calculated again with a warm-end temperature of 273 K, in Figure 3.14.

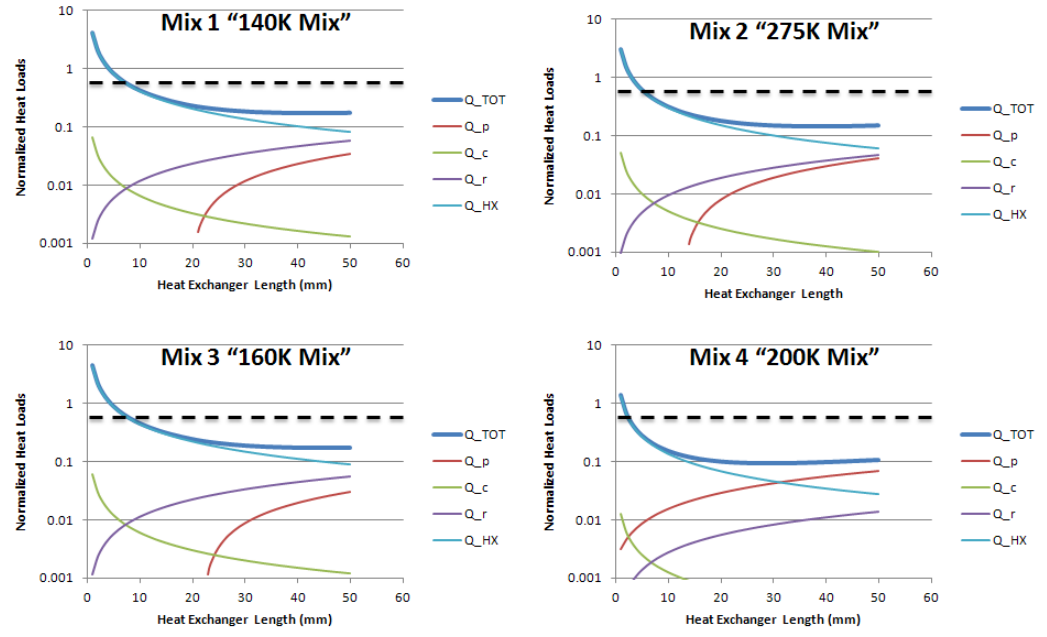

Figure 3.13: Calculated heat loads for the 4 refrigerant mixtures with a warm-end temperature

of 273 K.

3.4 Test Setup

The test setup is shown in Figure 3.15. The suction and discharge pressures of the miniature compressor were measured. The flow-rate of the refrigerant was monitored by a mass flow-meter, installed on the low-pressure side of the test-loop. A small platinum resistance thermometer (PRT) was mounted to the cold end of the MCC. The temperature was measured by applying a small voltage to the PRT, and measuring the current draw; the voltage was controlled to ensure that Joule heating in the PRT was below 0.1 mW. Pre-cooling of the refrigerant as facilitated by placing the MCC base in an ice bath, and a second PRT was mounted to the base of the MCC to monitor the base temperature. The MCC was held in a vacuum of $<10^{-4}$ Torr during the cooling tests, to minimize heat loads associated with conduction through air. The pressure, temperature, and flow-rate data were recorded by a computer running LabVIEW. For compressor characterization tests, the MCC was replaced by a needle-valve to provide a variable flow resistance.

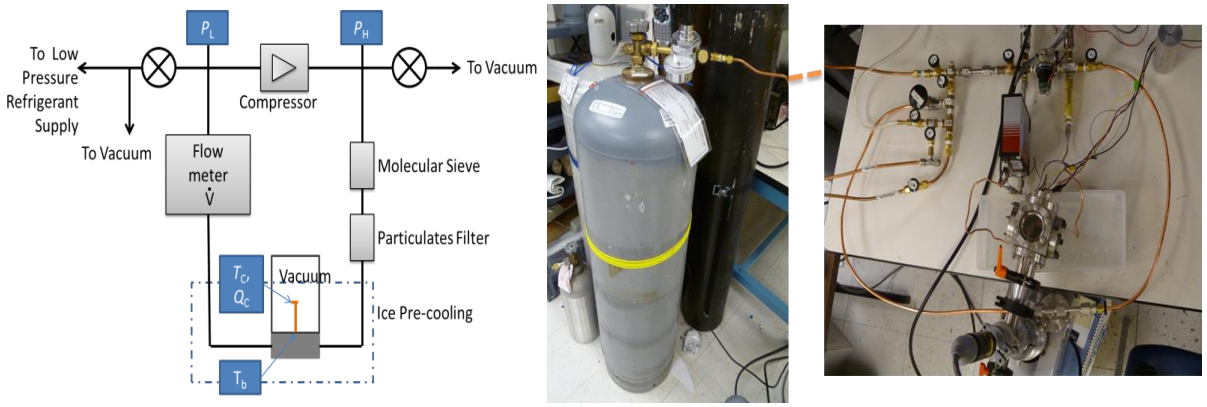

Figure 3.15: Schematic and photograph of test setup. Adapted from 53.

Icing has been noted as a problem in MCCs [46], so to ensure that any trace amount of water in the refrigerant was removed, 1 g of 3 Å molecular sieve was placed in the test loop. A 15 μm particulates filter was installed between the molecular sieve and the MCC to prevent any particulate build-up in the micro-channels. Before running any tests, the lines were evacuated to a pressure of $<10^{-4}$ Torr, then charged with refrigerant from a low-pressure supply cylinder.

3.5 Cooling Results

3.5.1 Cooling from ambient

The cooling profile for the six refrigerants is shown in Figure 3.16. With isobutane, the minimum temperature was governed by the boiling point of isobutane at the low pressure. In each of the mixtures, and with propane, the minimum temperature was determined by balancing the cooling power with the parasitic heat loads on the MCC, including heat conducted through the heat exchanger, through the DC leads on the temperature sensor, radiation from the vacuum package, and conduction through the rarified gas in the vacuum. The minimum temperatures, corresponding heat loads, and cooling power are all listed in Table 3.2. These specific cooling powers of several hundred J/mol are values typically found in J-T cooling in which the refrigerant enters the heat exchanger as a single-phase vapor. These gas-refrigerant systems typically have $(\Delta h|_T)_{min}$ values that are an order of magnitude lower than liquid-refrigerant systems, in which the refrigerant entering the heat exchanger contains liquid components. The test running pure propane is expected to be a gas-refrigerant system when cooling from ambient temperature, but the mixtures are designed to have some liquid at ambient temperature under high pressure. Note that the cool-down time for the mixtures is considerably longer than for the pure refrigerants. This phenomenon will be discussed in greater detail in Chapter 4.

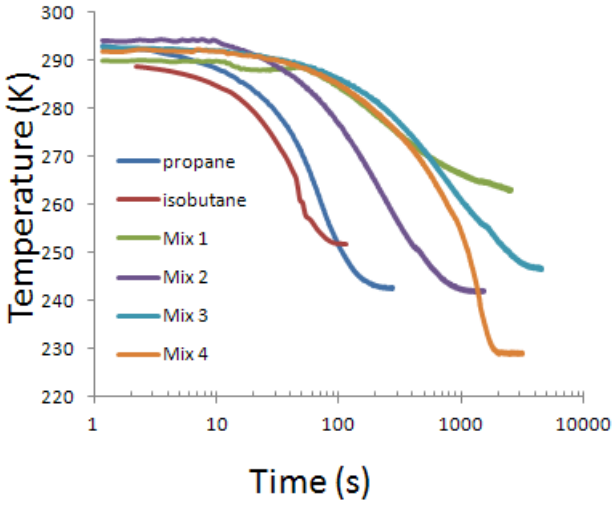

Figure 3.16: Cool-down curves for the 6 refrigerants in question, plotted as a semi-log plot. Note that the pure refrigerants cool quickest, but Mix 4 reaches the lowest temperature.

	T_{min} (K)	Q (mW) At 295 K	Measured Δh at 295 K (J/mol)	Calculated Δh at 295 K (J/mol)
Propane	242.2	15.8	603	723
Mix 1	261.7	4.67	378.6	4,845
Mix 2	241.7	6.63	328.3	1,932
Mix 3	245.6	5.53	329.7	5,222
Mix 4	228.4	7.89	415.8	7,574

Table 3.2: Minimum temperature, heat load required to keep the MCC at ambient temperature, and associated refrigerant enthalpy change, for propane and the four mixtures. The enthalpy change calculation is performed with REFPROP between 0.6 MPa and 0.1 MPa.

3.5.2 Effect of pre-cooling

When the system operating with propane was pre-cooled with an ice bath, the refrigerant going into the system was in the liquid-phase. As it subsequently evaporates across the J-T valve, its low temperature is limited by the boiling point at the low-pressure, shown in Figure 3.17.

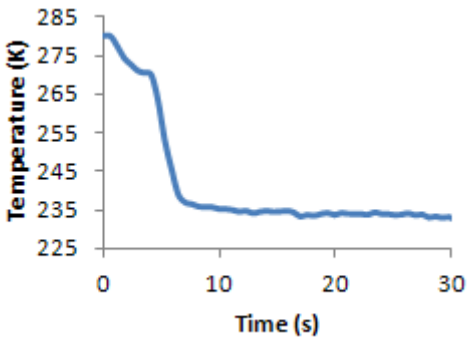

Figure 3.17: cool-down curve of propane with ice pre-cooling.

With the refrigerant mixtures, the cool-down curves are shown in Figure 3.18. The test of each mixture was conducted with the same refrigerant charge used for the non-pre-cooled tests. With each mixture, the system experiences steady flow rates for a period of time, during which time the MCC reaches a steady temperature. Eventually, the system experiences pulses in the flow-rate, corresponding to departures from the steady temperature. In the case of Mixtures 1 and 4, the pulses correspond to increased cooling power, and the temperature decreases. But for Mixtures 2 and 3, the overall cooling power does not increase, and the average temperature remains constant. Detailed analysis of the cooling power during steady flow will be the subject of Chapter 4, and analysis of the cooling power and flow-regime associated with pulsating flow will be the subject of Chapter 5.

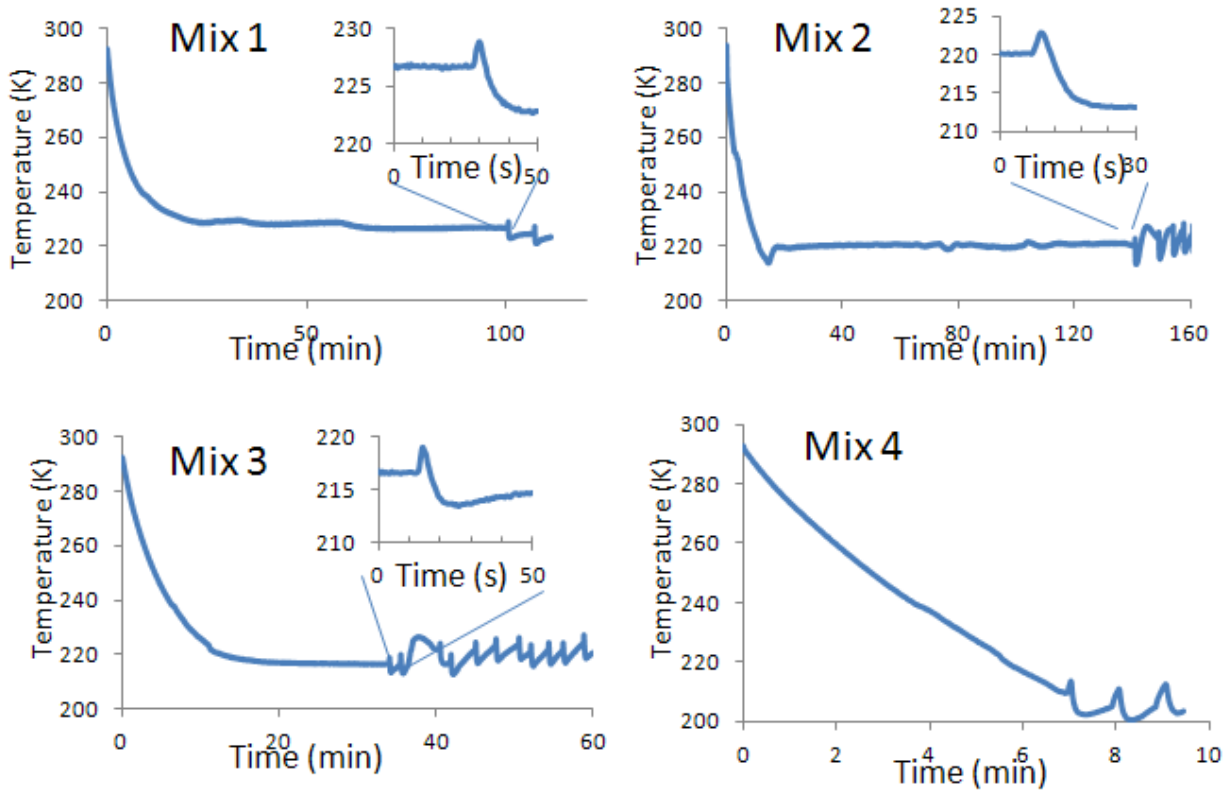

Figure 3.18: Cool-down curves of the 4 mixtures with ice pre-cooling. Inserts for Mix 1, 2, and 3 show a zoomed-in profile of the first departure from steady-state. Note that there are different time scales for each plot.

After the flow transitioned to pulsing flow, heat was applied to the PRT to lift the temperature up to the base temperature of 273 K. Measurement of the average heat applied and the flow-rate yields the average isothermal enthalpy difference of the mixture at 273 K, which is listed in Table 3.

	T before pulses (K)	T after pulses (K)	Measured Δh at 273 K (J/mol)	Calculated Δh at 273 K (J/mol)	Time to pulses (min)	Calculated time to pulses (min)
Mix 1	226.8	222.6	384.1	3751	100.4	54
Mix 2	220.3	222.3	545.4	4737	140.5	17.3
Mix 3	216.9	220.2	747.1	7660	34.1	29.4
Mix 4	209.9	193.6	1135.8	8412	7.1	7.25

Table 3.3: Steady-state temperature (before pulses), average temperature after pulses, isothermal enthalpy difference at 273 K measured with pulses, calculated enthalpy differences, measured time between cooling and pulses, and a calculation of that time based on a model given in Chapter 5.4.3.

Of these refrigerant mixtures, only Mix 4 is successful insofar as it reaches the low-temperature for which it is designed. It was then subjected to a more thorough investigation.

3.5.3 Temperature stabilization with 200K Mix

The MCC was connected to the test setup, 0.125 MPa of refrigerant was fed to the low-pressure side, and the system cooled as shown in Figure 3.19. During an initial charging period, the high-pressure and flow rate built up slowly. During that period, the cooling was slow. Eventually, the flow rate started to experience intermittent drops and jumps, and this was accompanied by rapid cooling. However, the low temperatures were not stable.

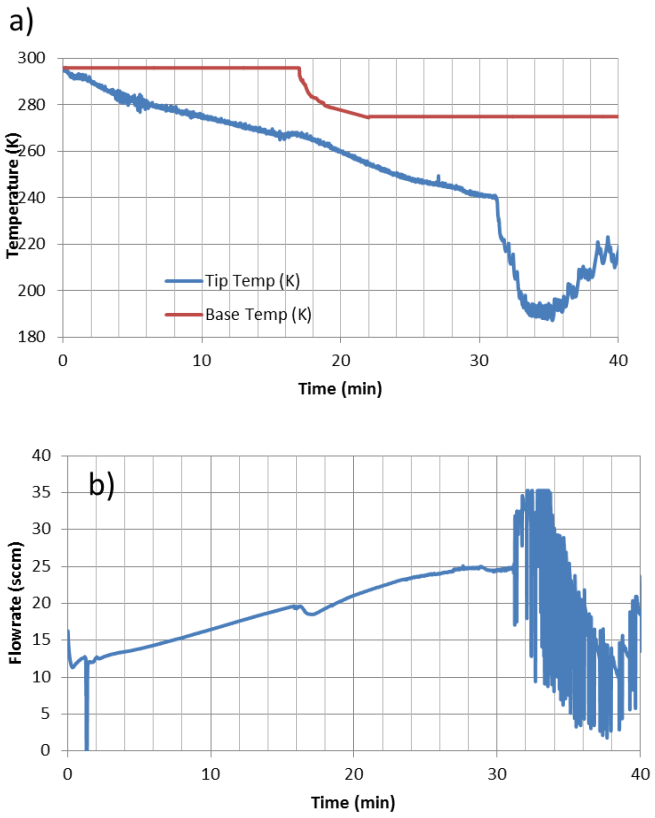

Figure 3.19: (a) the temperature profile and (b) flow rate as the MCC cools down. There is a 30 minute initial period where the flow rate builds up, followed by rapid cooling which accompanies instabilities in the flow rate. Reproduced from [55].

Because the J-T valve of our MCC has a transparent top, we were able to visualize the refrigerant during the unsteady flow period. It was found that the intermitted drops and jumps in flow rate were associated with a sudden build-up of liquid in the J-T valve, shown in Figure 3.20. Previous studies of hydrocarbon refrigerants in microchannels have shown that under certain conditions the refrigerant can form intermitted liquid slugs [58]. Although the specific conditions which lead to slug-flow are still a topic of research, it is likely that that is causing the instabilities in flow rate seen in our MCC.

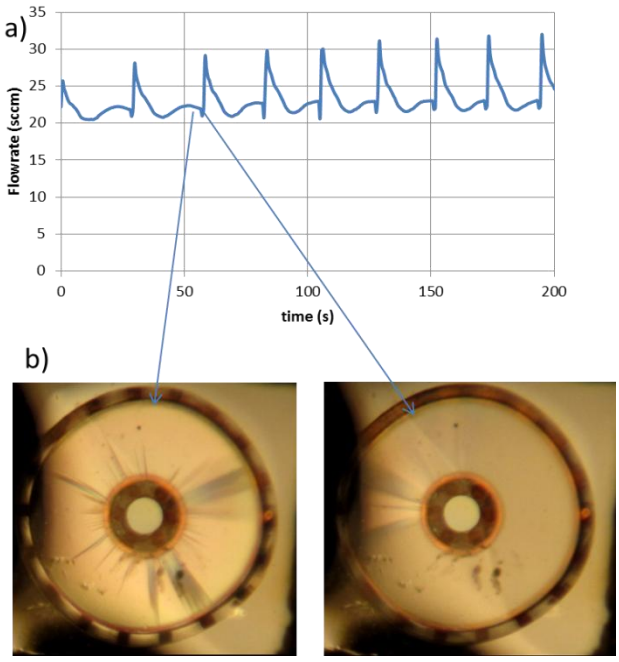

Figure 3.20: 200 s of flow rate data collected while visualizing the cold-tip. Darker regions in the J-T valve are liquid, and lighter regions are vapor. The cold-tip fills with liquid during the periodic jumps in flow rate. Reproduced from [55].

The unstable flow gives rise to unstable temperatures on the cold tip of the MCC. These temperatures can be stabilized by using the PRT as a small heater in addition to a temperature sensor. By controlling the voltage applied to the PRT, one can briefly apply 15-25 mW of heat to the MCC whenever it crosses below a pre-defined temperature.

As the flow fluctuates it periodically switches between high-cooling and low-cooling modes. During the period with lower cooling power, the MCC is still liable to warm above the desired temperature, up to 6 K, as shown in Figure 3.21a. To alleviate this, the frequency of the oscillations must be higher or the thermal mass of the cold-end must be more such that it does not warm appreciably during periods of lower cooling power. It was found that increasing the flow-rate through the MCC to 50 sccm could increase the frequency enough to stabilize the temperature to within 1 K, shown in Figure 3.21b. This higher flow-rate was achieved by assembling a second MCC, and the assembly variation resulted in a different flow-rate response.

A third MCC with a 1.9 μm gap for the J-T valve was assembled as well. This larger gap allowed a flow-rate of 125 sccm with a high-side pressure of 0.42 MPa. However at such a flow-rate, the pressure drop in the heat exchanger prevented a high enough pressure ratio across the J-T valve, and the MCC only experienced cooling to 210 K, as shown in Figure 3.21c. Unfortunately, the second MCC was damaged before the cooling power could be fully characterized. The next section on MCC efficiency will only consider the first MCC with a flow-rate in the range 10-30 sccm.

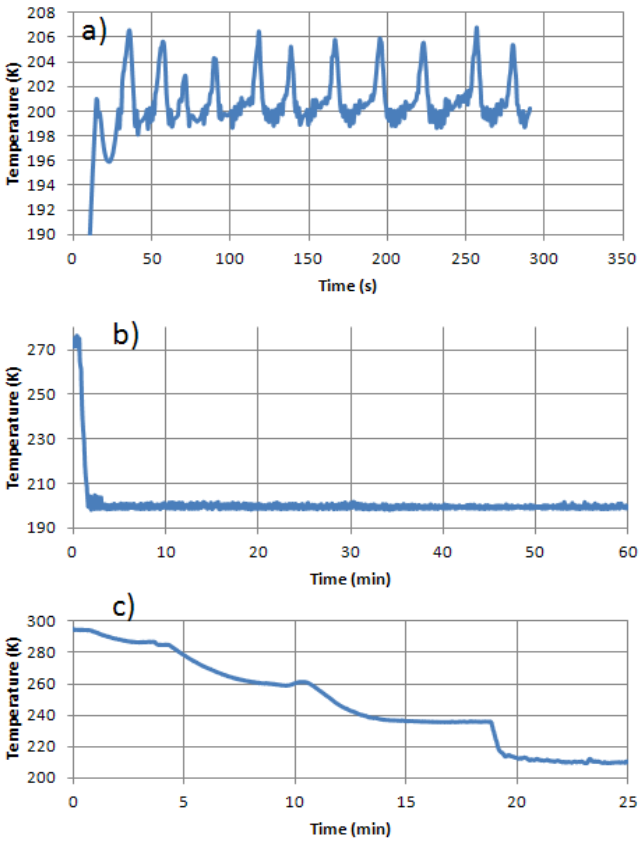

Figure 3.21: Stabilized temperatures showing (a) spikes of 6 K; *(b) stability to* ±1 °C, *with rapid cooling from 275 to 200 K in 62 s; and (c) a device with high flow-rates preventing cooling below 210 K. No heat is applied for the third device. Reproduced from [55].*

3.5.4 Cooler Efficiency.

The coefficient of performance (COP) of the system is defined as the ratio of the heat lift at the

cooler to the power input at the compressor. Recall from figure 3.10 that the efficiency of the compressor is quite low at the low flow-rates seen by the MCC. The effect of the compressor inefficiency can be removed from the analysis by considering the performance of the cooler in terms of the ratio of heat lift to the change in Gibb's free energy at the compressor: $\dot{n}\Delta g$. An ideal J-T cooler has a COP where the cooling power is given by $\dot{n}(\Delta h|_T)_{min}$ and the compressor power is given by the same flow-rate, times the change in Gibb's free energy. The COPs for the system, for the cooler, and for an ideal J-T cooler, are therefore given by:

$$\begin{aligned} COP_{system} &= \frac{\dot{Q}_c}{P} \\ COP_{cooler} &= \frac{\dot{Q}_c}{\dot{n}\Delta g} \\ COP_{ideal\ JT} &= \frac{(\Delta h|_T)_{min}}{\Delta g} \end{aligned} \tag{3.6}$$

Two separate tests were performed to measure the COP as a function of both temperature and low-side pressure, with results plotted in Figure 3.22. The cooling power of the MCC must remove all the heat generated from the device under testing, which in this case is considered to be the PRT. This heat includes both the active Joule heating when the PRT acts as a heater (~5 mW), and any heat absorbed by the PRT from the surroundings through radiation or conduction through the DC leads (~2 mW). These parasitic heat loads on the PRT are calculated based on the device geometry and temperature.

For the tests with results plotted in Figure 3.22a, the pressure ratio was maintained at 4.6:1, and the temperature at 200 K. With increasing pressure, $(\Delta h|_T)_{min}$ decreases, resulting in a decrease in $COP_{ideal\ J\text{-}T}$. However, an increasing pressure causes an increasing flow-rate through the MCC, resulting in a higher heat-lift and higher COP_{cooler}. The increasing back-pressure also increases the power consumed by the compressor, so the COP of the system is largely unaffected by the different pressures, until above 0.145 MPa, the COP_{system} decreases with further increases

in pressure.

In order to reach the lower temperatures shown in Figure 3.22b, the higher cooling power associated with higher pressures was required. Hence the system was held with a high pressure of 0.72 MPa and a low pressure of 0.15 MPa. Note that as temperature increases, the ideal J-T cooler COP increases. This is because $(\Delta h|_T)_{min}$ drops for T<200 K as shown in Figure 5. Note that the cooler COP increases with a faster slope than $COP_{ideal\ J\text{-}T}$, between 178 and 191 K. This indicates that there is both a decreased gross cooling power due to the lower $(\Delta h|_T)_{min,}$ and a further decreased net cooling power due to parasitic heat loads on the MCC such as radiation and conduction down the CFHX, which increase with decreasing temperature. At 197 K, there was a decrease in flow-rate—likely a result of an increase in viscosity of the refrigerant mixture—which cause the cooling power and COP_{cooler} to decrease. At 200 K, the effects of an increased $(\Delta h|_T)_{min}$ and decreased parasitic heat loads caused the COP_{cooler} to increase further. During this test, the power drawn by the compressor remained constant.

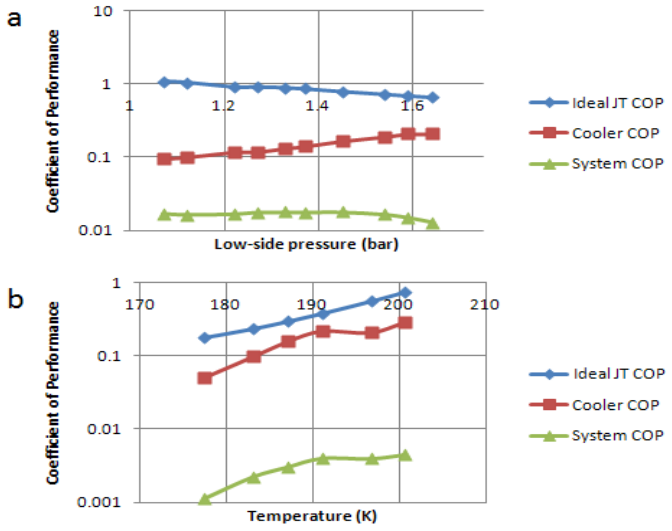

Figure 3.22: Curves of an ideal J-T cooler COP, cooler COP, and system COP: (a) COPs as a function of pressure, at 200 K; (b) COPs as a function of temperature, with high pressure of 0.72MPa and low pressure of 0.15 MPa. Enthalpy and Gibb's free energy values were calculated

with REFPROP [19].

The maximum COP of the cooler reaches 60% of the COP of an ideal J-T cooler at 191 K, with a value of 0.25. For comparison, the highest ideal J-T COP of any pure fluid in the same temperature range with the same pressures occurs for R-23 (chlorodifluoromethane) with a COP of 0.14. For our MCC, the maximum system COP is 0.018, which is comparable to the COP of multi-stage thermoelectric coolers for the same temperature range and heat lift. Our COP is expected to increase significantly with compressor optimization. Such a compressor is developed in Chapter 6.

3.5.5 Background heat.

Parasitic heat loads on the MCC include heat conducted through the heat exchanger, through the DC leads on the temperature sensor, radiation from the vacuum package, and conduction through the rarified gas in the vacuum. Such heat loads were characterized as a function of temperature by performing a background heat leak test [57]. In such a test, the MCC is first cooled to a low temperature. The compressor is then shut down, high-side pressure vented (to drop the flow-rate to 0), and a known heat is applied to the cold-tip. With no cooling power, the MCC starts to warm up, and the temperature profile is recorded. At each temperature, there is a unique temperature rise rate (dT/dt). The process is repeated several times with different heat loads. The heat load is plotted as a function of (dT/dt) at a single temperature, giving a linear relationship. Extrapolating that linear relationship to dT/dt=0 gives a negative heat load value, which corresponds to the cooling power required to keep the temperature at a stable value—in essence the cooling power equal to the background loads at that temperature. Deviations from linearity are represented in an uncertainty in the measured value. The background loads as a function of temperature are plotted for a 25 mm long fiber-based MCC in Figure 3.23, for both ice pre-cooling and no pre-cooling.

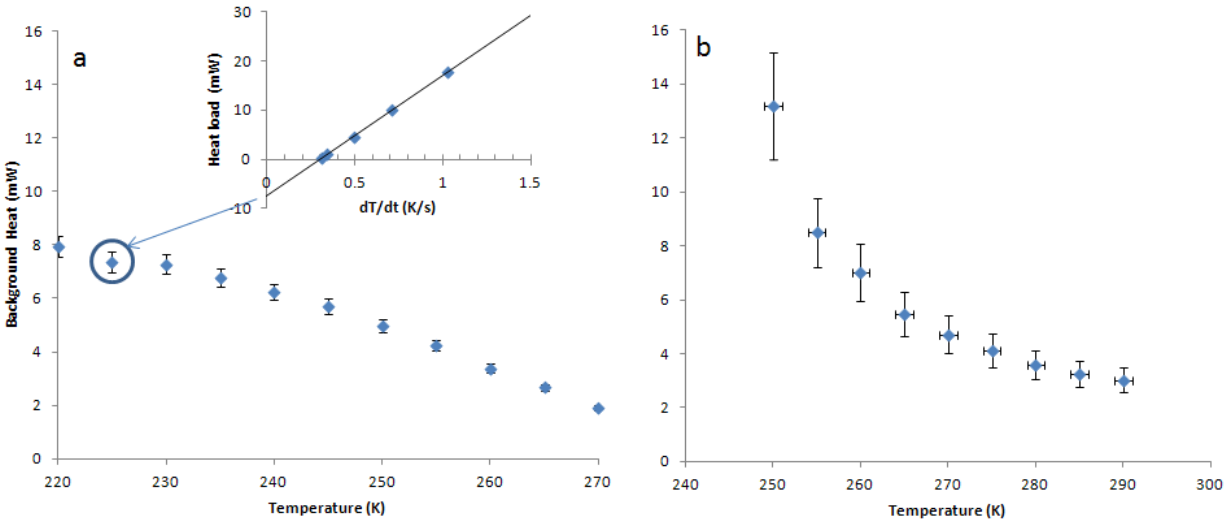

Figure 3.23: background heat load for a) ice pre-cooling, and b) no pre-cooling. The insert shows the dT/dt and heat load data used to determine a background heat load of 7.36 mW at 225 K.

3.6 Conclusions

This chapter covers the following: assembly of fiber-based MCCs, following the method of Lin [16], but updating the process to include an epoxy-based solution; assembly and characterization of a miniature compressor, based on a commercial rotary piston oscillator and micromachined check-valves; and testing of the MCC with the miniature compressor using refrigerant mixtures. The compressor can generate a maximum pressure of 0.76 MPa with a suction pressure of 0.1 MPa using Nitrogen as a compressible fluid, and can produce a maximum flow-rate of 503 sccm. The pressure and flow-rate data can be modeled either by assuming the compression is isothermal or isentropic, and both models agree with the data when a dead-volume parameter is adjusted. A maximum efficiency of 17 % at a flow-rate of 270 sccm, but considerably lower efficiencies are seen when the flow-rate is a lower range.

When coupled to a MCC and running with a mixed refrigerant, the compressor requires a long initial period to build up a high pressure and resulting high flow-rate. In contrast, pure

refrigerants are much quicker at reaching their final pressure and flow-rate. Without pre-cooling, the cooling-powers of the mixtures are much lower than calculated. With pre-cooling, the refrigerants first experience steady flow, with low cooling power. Eventually all of the refrigerants will cause the MCC and compressor to experience a pulsing flow regime. In some cases this will greatly enhance the refrigerant cooling power. A study of the steady flow regime will be the subject of Chapter 4, which will develop a model of cooling power based on refrigerant separation in the high-pressure lines. The idea of refrigerant separation will also be used to model the initial pressure build-up period of the refrigerant mixtures. Chapter 5 will cover a thorough study of the pulsating flow phenomenon, developing models for time-to-pulses, isothermal specific cooling power of the refrigerants undergoing pulses, and non-isothermal specific cooling power.

The cooling power of a MCC operating with the “successful” mixture was measured, from which a coefficient of performance was calculated to be 0.018. The largest contributor of inefficiencies was the compressor, which has its optimal operation with a much higher flow-rate. Our COP is expected to increase significantly if a compressor had optimal operation at a flow-rate of 10-30 sccm. Such a compressor is developed in Chapter 6.

CHAPTER 4: ANALYSIS OF STEADY FLOW IN MICRO CRYOGENIC COOLERS[1]

Micro cryogenic coolers (MCCs) are useful to a number of small electronic devices which require low cooling power. The cooling power of micro cryogenic coolers operating with mixed refrigerants in a Joule-Thomson (J-T) cycle can be calculated based on enthalpy change for the mixture, but it has been observed that cooling power depends on flow regime. This chapter demonstrates a method to measure the isothermal enthalpy change in a mixture undergoing J-T expansion in an MCC for different flow regimes. The enthalpy change for a mixture undergoing steady flow is an order of magnitude below that calculated. For steady flow, an analysis of component separation within the mixture due to annular flow shows good agreement with measured data.

4.1 Introduction

As was mentioned in the previous chapter, when running a MCC with a miniature compressor and low-pressure mixture, the system first experiences a steady flow regime and a low cooling power. Eventually the system transitions to an unsteady flow regime where the flow experiences pulses. These pulses have been associated with liquid in the J-T valve of the MCC (See Figure 3.17). This chapter covers a method to measure the specific cooling power of the MCC in both steady and pulsating flow regimes, and develops a model for the steady flow regime. Section 4.2 covers the cooling-power and subsequent enthalpy measurement, with results shown in section 4.3. Section 4.4 develops a model of the steady flow cooling power by considering the liquid hold-up due to an annular flow regime, showing good agreement between the measured enthalpy difference and the modeled enthalpy difference.

[1] Portions of this chapter are reproduced from [59], with permission from Elsevier.

4.2 Methods and Materials

4.2.1 Test Set-up

The ideal cooling power ($\dot{Q}$) of a J-T cryogenic cooler can be calculated as the product of the flow rate ($\dot{n}$) with the minimum isothermal enthalpy difference between the high- and low-pressure refrigerant, over the temperature range experienced by the cooler [21]: $\dot{Q} = \dot{n}\,(\Delta h|_T)_{\min}$. Enthalpy can be calculated as a function of pressure, temperature, and refrigerant composition from an equation of state model, and the isothermal enthalpy changes can be subsequently found. The refrigerant studied in this chapter is a Mix 4 ("200K Mix") composed of methane (8 %), ethane (46 %), propane (14 %), butane (4 %) and pentane (28 %). (Values given in molar percent.) The compositions were chosen to maximize $(\Delta h|_T)_{\min}$ between a high pressure of 0.4 MPa and a low pressure of 0.1 MPa, over the temperature range of 200 K to 300 K. Although the refrigerant is designed to cool from 300 K, pre-cooling to 275 K was found to be necessary for effective cooling with MCCs using this refrigerant [12, 55]. In this test, the micro cooler is studied under an isothermal condition, where the cold-end of the MCC is actively heated until it is the same temperature as the warm-end. When there is only a single temperature experienced by the cooler, rather than a temperature range, the cooling power is given by $\dot{n}\,(\Delta h)$, with the enthalpy calculated at the device temperature.

The J-T MCC used in this experiment is shown in Figure 4.1, and is composed of a micro-machined J-T valve, hollow-core fiber-based counter-flow heat exchanger (CFHX), and micro-coupler. Fabrication and assembly of this device are detailed in Chapter 3, but briefly covered here. The J-T valve is formed by anodic-bonding a borosilicate glass chip to an etched silicon chip. A gap between the two chips measuring 1.5 μm in height and 500 μm radially provides a flow restriction where the refrigerant undergoes Joule-Thomson expansion and

cooling. A second MCC was also assembled with a gap height of 1.9 µm, which allowed much higher flow-rates. High-pressure refrigerant is delivered to the J-T valve through hollow-core glass fibers with inner diameter and outer diameter (ID/OD) of 75/125 µm. The fibers are held in a glass capillary ID/OD=536/617 µm, and the low-pressure refrigerant travels through the interstitial space between the fibers within the capillary, forming a CFHX. However, in this test the temperature across the entire cooler is ideally held at a single temperature, so no heat needs to be transferred between the low-pressure and high-pressure micro-channels. Still, when the cooler acts in a non-steady flow regime, the presence of a heat exchanger allows us to quickly resolve changes in the cooling power.

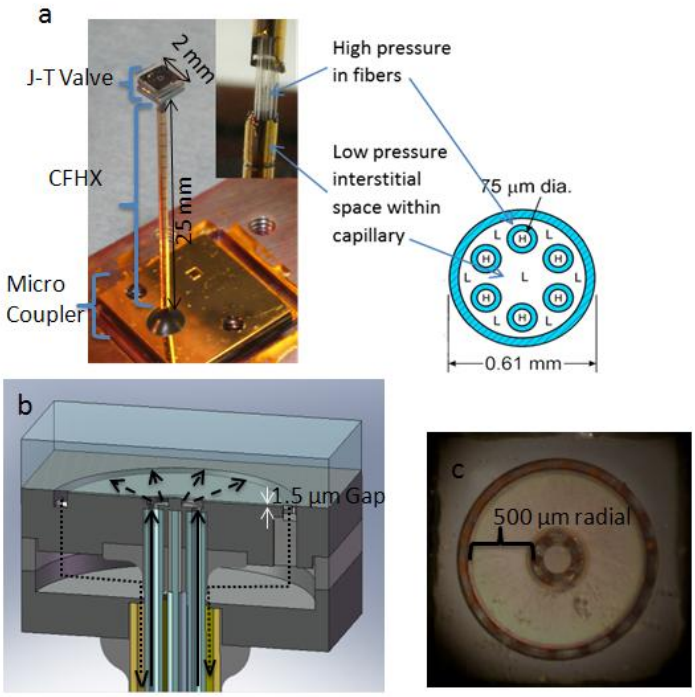

Figure 4.1: The micro cryogenic cooler used in this experiment: a) photograph of the MCC, with insert showing fiber micro-channels held within a capillary forming the CFHX; b) schematic of J-T valve, showing the path of the high-pressure refrigerant (solid line) as it expands across the J-T valve (dashed line), and returns at a low-pressure (dotted line); and c) top-view photograph of the J-T valve.

The micro-coupler interfaces the MCC with the external test setup, shown in Figure 4.2.

The refrigerant was compressed by a customized non-lubricated miniature compressor, described in the previous chapter. Pressures and flow-rates of the refrigerant were monitored. It has been noted that MCCs can suffer from clogging due to ice formation from trace water in the system [46]. Previous studies with this MCC have used activated carbon adsorption systems to remove trace water [21]; however such a dryer system would also selectively adsorb some of the hydrocarbon refrigerants and change the composition of our refrigerant. Therefore, a 0.3 nm molecular sieve was used to remove trace moisture contaminants without changing the composition of the refrigerant mixture. After the molecular sieve, the refrigerant passes through a particulates filter with a sintered mesh of 7 μm element pore size, to remove any particulate contaminants [55]. Pressure drops across the molecular sieve and filter are measured to be <0.1 kPa. Standard 1/8" copper refrigeration tubing carries the filtered refrigerant to the MCC. The MCC was held under vacuum during the tests. The vacuum test stage and 20 cm of the coupling tubing was placed in an alcohol bath to pre-cool the refrigerant and ensure a steady yet controllable warm-end temperature. A radiation shield shrouded the MCC cold end, preventing heat loads due to radiation from lab ambient conditions. The temperatures at the radiation shield, MCC base, and J-T valve on the MCC were measured with platinum resistance thermometers. A voltage was applied to the resistance thermometer at the J-T valve, which provided heating to the cold-tip of the MCC. A computer running LabVIEW used a control-loop to determine the voltage to ensure that the temperature of the J-T valve was the same as that at the inlet to the CFHX, such that the device could experience an isothermal enthalpy difference.

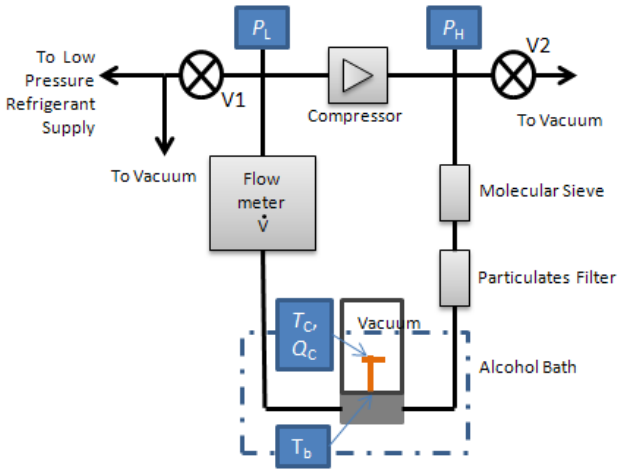

Figure 4.2: schematic of the test set-up used. Measured values include low-side pressure (P_L), high-side pressure (P_H), base temperature (T_b), cold-tip temperature (T_c), heat applied to cold-tip (Q_c), and flow-rate ($\dot{V}$). During the tests, Valve 1 remains open to the low pressure refrigerant supply.

4.2.2 Isothermal Enthalpy Measurement

The heat applied to the MCC by the control-loop determined the net cooling power of the MCC. The gross cooling power was the sum of the net cooling power and the parasitic heat loads. Such loads are due to radiation, conduction through the DC leads, conduction through the CFHX, and conduction through the vacuum. Ideally, the entire MCC is at the same temperature as the vacuum test stage, so there would be no temperature gradients to drive conductive or radiative heat transfer. However during the test, temperature differences of up to 1°C between the cold-tip and warm base can occur, resulting in some conductive and radiative heat loads. Radiative heat loads were calculated from the Stefan Boltzmann law with a known radiation shield temperature, known cold-tip temperature, and known MCC geometry. Conductive heat loads were calculated from a Fourier's Law model, through the glass heat exchanger and DC leads with known geometry. Enthalpy change could then be calculated based on the heat load and flow-rate measurements. This measures the change in enthalpy between the high-pressure and low-pressure streams at the J-T valve. But because enthalpy is a function of temperature and pressure,

and the temperature at the J-T valve is kept the same as the temperature at the warm-end inlet to the MCC, and if pressure drops in the CFHX are small, this will also be the enthalpy change across the entire MCC—including heat exchanger.

When the refrigerant mixture was operated at the temperature range in question with the low-flowrate MCC (1.5 μm gap), the miniature compressor could generate a high pressure of 0.337 MPa with a suction pressure of 0.100 MPa, which was open to the refrigerant supply tank, regulated at 0.100 MPa. The tank further ensured a constant composition of the refrigerant at the compressor, which differs from the method used by Gong, Deng and Wu [37], which did not use a low pressure reservoir, but rather used an initial charge in their system. The composition shift they observed was based on location in the J-T system. Our pressure in the MCC corresponds to a flow-rate that varied between 2 and 6 std. cubic cm per minute (sccm), depending on temperature. With this flow-rate over the temperature range of interest, two distinct flow patterns were observed: one with steady flow-rates, and another with pulsating flow-rates.

After data were collected for 5 minutes at a single temperature, the alcohol temperature was changed, the system allowed to equilibrate at the updated temperature, and data acquisition resumed. The test started with the alcohol bath at a temperature of 294 K and the MCC system operating in a steady flow regime. The bath was then cooled in increments of 2-5 K, down to 270 K. At that point the test had been operating for roughly 1 hour, and the system transitioned to a pulsating flow regime. Once in the pulsating flow regime, the temperature was increased to collect pulsating flow enthalpy data in the temperature range 270-300 K. Pulsating flow will be the subject of Chapter 5, and not discussed in this chapter. To get steady-flow data at lower temperatures, the lines were evacuated, re-charged with fresh refrigerant, and the test started with an alcohol bath at 270 K. After decreasing in steps to 245 K, over a period of 1 hour, the system

again transitioned to pulsating flow. The bath was cooled further to 240 K, below which thermal stresses began to damage seals in the coupler. Sealing damaged was noticed due to small amount of refrigerant leaking into the vacuum space during each flow pulse (the pressure of the evacuated chamber would briefly increase from 10^{-4} Torr to 10^{-2} Torr at times coenciding with a pulse). The bath temperature was increased in increments in order to complete the enthalpy measurements for pulsating flow.

For the higher-flow-rate MCC (1.9 μm gap), a similar test procedure was applied, but the cooler response was different. The pressure generated was 0.45 MPa, with flow-rates in the range 115-125 sccm. The reason for this discrepancy will be discussed in section 4.4.4. With higer flow-rates, the steady flow regime persisted for a shorter period of time. Steady flow-rate enthalpy measurements were taken starting at a bath 294 K, then deccreased down to 280 K, at which point the flow regime transitioned into plusing flow. Bath temperatures were increased in steps to 286 K to measure the pulsing flow enthalpy difference in that temperature range—which will be discussed in the next chapter. Afteward, the lines were evacuated, and re-charged, and the test started with a bath temperature of 277 K. Steady flow enthalpy data was measured in steps down to a temperature of 265 K, at which point flow pulsations began. An attempt was made to measure steady flow at lower temperatures by re-charging the lines a third time, but by the time the MCC base temperature reached the low temperature of 265 K, flow pulsations had developed.

4.3 Results

The isothermal enthalpy change data for these two flow regimes are plotted against cold-tip temperature in Figure 4.3. Also included is a calculation of enthalpy difference between the

mixture at 0.337 MPa and 0.1 MPa as a function of temperature, as calculated by the NIST standard reference data software REFPROP [19]. Uncertainty bars come from both a variation in measured enthalpy data over the 5 minute data collection time, and inaccuracies from the measurement of the parasitic loads. The parasitic loads are assumed to be accurate to 10 %. The statistical uncertainties are calculated from the first standard deviation in enthalpy data collected over 300 seconds, which includes variations in the parasitic heat loads. The parasitic loads are up to 0.3 mW, and applied heat loads are typically in the range 0.2-0.8 mW for the low-flow-rate, steady flow tests, so these loads are quite significant to the those measurements. The high-flow-rate steady tests saw applied heat of 20 mW, so parasitic were much less significant.

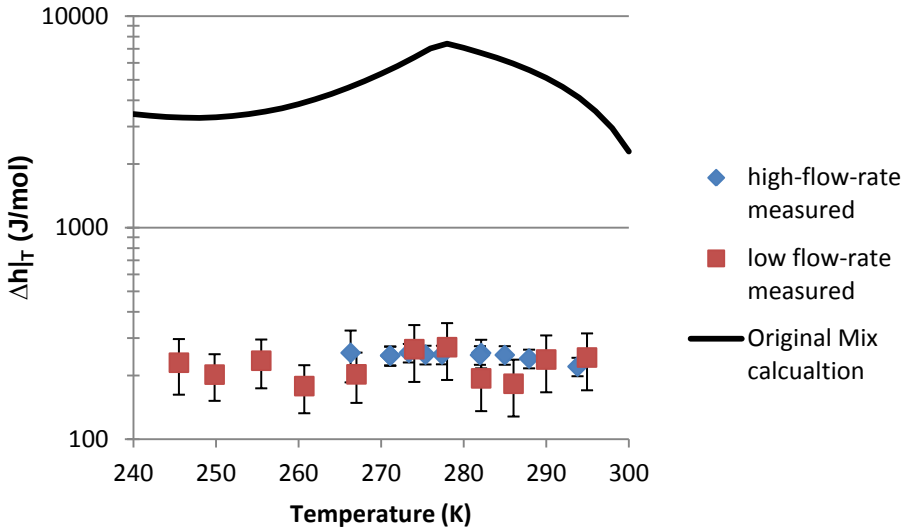

Figure 4.3: a) measured values of isothermal enthalpy change of the refrigerant for both high- and low-flow-rate MCCs as well as values calculated by REFPROP for a 2-phase mixture, plotted against cold-tip temperature.

4.4 Discussion

4.4.1 Steady-flow Enthalpy and Liquid Hold-up

Note from Figure 4.3 that for steady flow they can be an order of magnitude below those calculated. The reason for this discrepancy lies in the liquid/vapor flow regime. With two-phase

flow, the gross cooling power across a J-T valve is found from an energy balance as (see Figure 4.4):

$$\dot{Q} = [\dot{n}_{\mathrm{v}} h_{\mathrm{v}} + \dot{n}_{\mathrm{l}} h_{\mathrm{l}}]_{P_{\mathrm{low}}} - [\dot{n}_{\mathrm{v}} h_{\mathrm{v}} + \dot{n}_{\mathrm{l}} h_{\mathrm{l}}]_{P_{\mathrm{high}}} = \dot{n}_{\mathrm{Tot}} \Delta h_{\mathrm{FA}}, \tag{4.1}$$

where $\dot{n}_{\mathrm{Tot}}$ is the total molecular flow rate of both phases, the subscripts v and l refer to the vapor and liquid phases, and Δh_{FA} is the flux-averaged difference enthalpy found by re-arranging Equation 4.1 to give:

$$\Delta h_{FA} = \left[\frac{\dot{n}_v}{\dot{n}_l+\dot{n}_v} h_v + \frac{\dot{n}_l}{\dot{n}_v+\dot{n}_l} h_l\right]_{P_{low}} - \left[\frac{\dot{n}_v}{\dot{n}_l+\dot{n}_v} h_v + \frac{\dot{n}_l}{\dot{n}_v+\dot{n}_l} h_l\right]_{P_{high}} \tag{4.2}$$

These "flow-averaged" quantities (sometimes referred to "cup-mixing" quantities [60]) are the values of flow-rate and enthalpy difference measured in this test; however REFPROP calculates mixture enthalpies based on mole-averaging between phases, rather than flow-averaging.

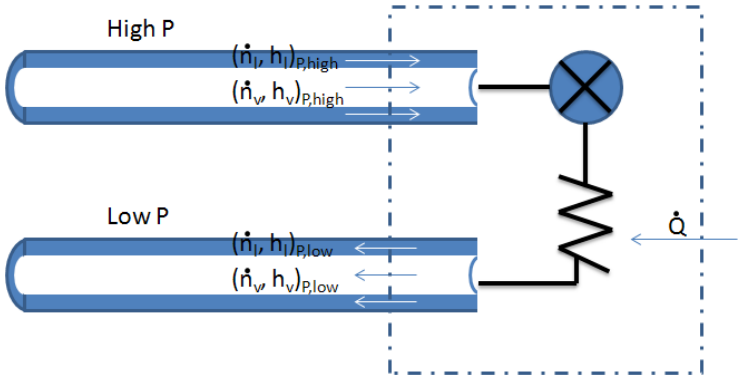

Figure 4.4: Schematic of refrigerant flowing through a heat exchanger into a J-T valve and absorbing heat at an evaporator, when the refrigerant is in a vapor-liquid 2-phase flow, with the liquid forming a film along the perimeter of the heat exchanger channels. An energy balance on the control volume (dashed-box) yields Equation 4.1.

The ratio of vapor mole flux to liquid mole flux depends on the flow regime. Initially, as the system cools, heavy components in the refrigerant will condense either on the sidewalls of the channels. With low flow-rates in micro channels, the ratio of fluxes can then be calculated

from Stokes theory, as [61]:

$$\frac{\dot{n}_l}{\dot{n}_v} = \frac{\rho_l}{\rho_v} \frac{-1-\left(\frac{r_i}{R}\right)^4+2\left(\frac{r_i}{R}\right)^2}{-2\left(\frac{r_i}{R}\right)^4-\left(\frac{r_i}{R}\right)^4\frac{\mu_l}{\mu_v}+\left(\frac{r_i}{R}\right)^2} \tag{4.3}$$

where ρ represents molar density, μ dynamic viscosity, R the channel radius and r_i the radius to the liquid/vapor interface. In a cylindrical geometry, r_i/R can be calculated from the vapor quality (X) of the mixture and liquid and vapor densities as:

$$\frac{r_i}{R} = \sqrt{\frac{X/\rho_v}{X/\rho_v+(1-X)/\rho_l}} \tag{4.4}$$

Physical properties of each phase can be calculated by REFPROP. Because the density of the liquid is much more than that of the vapor, the value of r_i/R will be close to 1, and consequently $\dot{n}_l/\dot{n}_v$<<1. The values 1- r_i/R and $\dot{n}_l/\dot{n}_v$ are plotted in Figure 4.5a for this mixture with a pressure of 0.337 MPa and the temperature range 240-300 K. Note that the ratio of liquid to vapor mole-flux is $<10^{-3}$ for this mixture over the temperature and pressure range seen during steady flow. Note also from Equations 4.3 and 4.4 that the ratio of liquid-to-vapor flow-rates is a function of fluid properties, but not the size of the channel in question. This analysis can be applied to the coupling channels as well as the micro-channels.

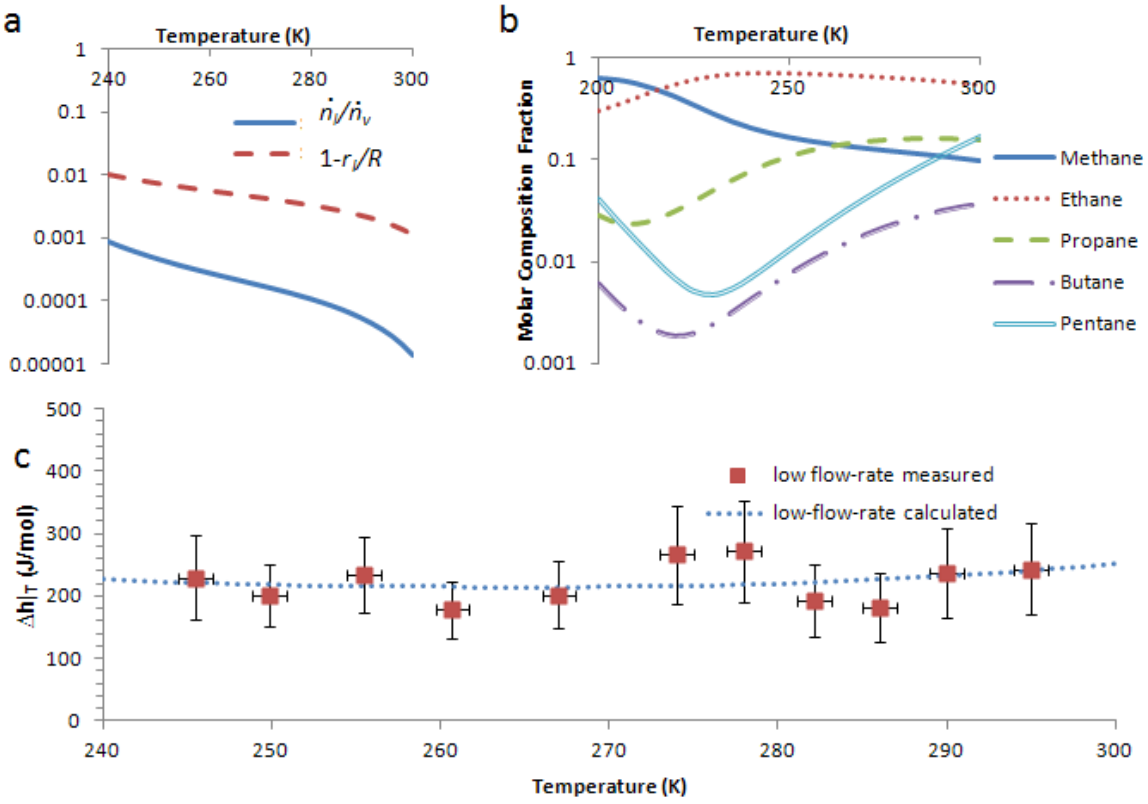

Figure 4.5: a) ratio of molar fluxes $\dot{n}_l/\dot{n}_v$, and a non-dimensional thickness of the liquid film 1-r_i/R, over the temperature range of interest at 0.377 MPa, b) molar composition of the vapor-phase of the refrigerant at 0.337 MPa for various temperatures, calculated by imposing vapor-liquid-equilibrium with REFPROP, c) measured isothermal enthalpy change for steady flow, and Δh values calculated with equations 2-4, plotted against MCC cold-tip temperature.

All components that liquefy in the high-pressure channels adhere to the walls, and only small amounts pass through the J-T valve and contribute to cooling. Liquid films are observed in the J-T valve. Because the mixture is non-azeotropic, the vapor has a different composition than that of the overall mixture, which is a function of both temperature and pressure, shown in figure 4.5b.

Figure 4.6 compares the high-flow-rate and the low-flow-rate both measured and calculated values. In the high pressure case, some pressure drop through the micro-channels is expected. This can be calculated from Poiseuille flow to be 0.03 MPa in both high and low

pressure sides of the heat exchanger. The calculations for the high-flow-rate MCC enthalpy measurements are thus carried out with a high pressure of 0.41 MPa and a low pressure of 0.13 MPa. This as well shows good agreement to the measured values.

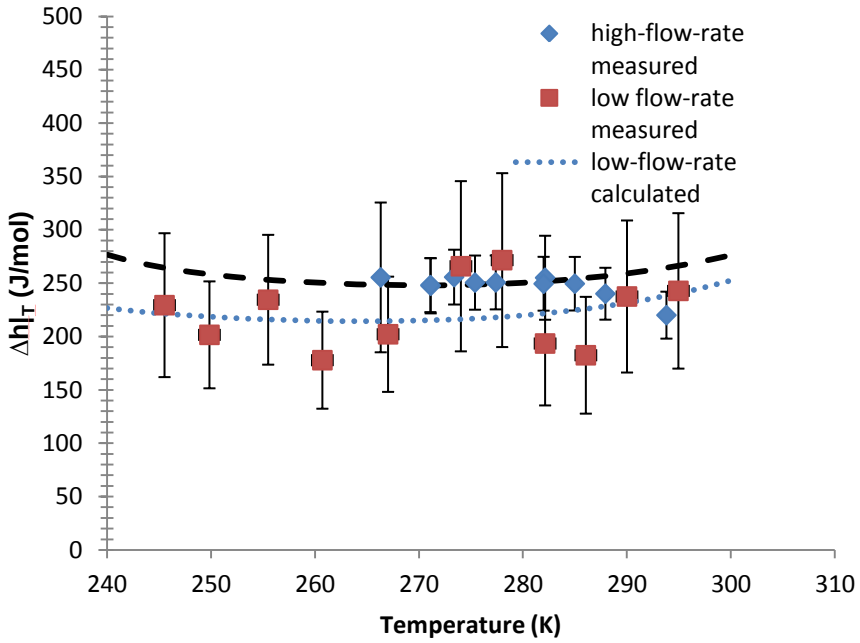

Figure 4.6: Isothermal enthalpy measurement and model with film flow for both high and low flow-rate MCC devices.

4.4.2 Composition Shift Model

In this refrigerant mixture, refrigerant will form a liquid along the wall. At the vapor-liquid interface, the composition of both the liquid and vapor are governed by vapor-liquid-equilibrium (VLE) conditions. Away from the interface, the composition in the vapor phase can be enriched in heavy components, compared to the VLE condition. For example, the original mixture contains 28 % pentane, and in VLE at 295 K and 0.337 MPa a vapor would only contain 16.5% pentane. Yet away from the interface the pentane concentration can be higher—up to the original 28 %. When the compressor suction port is connected directly to the original mixture, the vapor exiting the compressor discharge port will have a bulk pentane concentration of 28 %. However,

a very thin film of liquid will coat the walls around high-pressure channel, where the vapor pentane concentration will be 16.5 %. The pentane concentration in the channel can be found by applying a convective-diffusive transport equation, with an inlet boundary concentration of 28 %, and a wall boundary concentration of 16.5 %.

The convective-diffusive transport of *molecules* is mathematically equivalent to the convective-diffusive transport of *heat*, and an analytical solution to diffusion of heat in a cylinder undergoing laminar flow, with a constant wall temperature is given by:

$$\frac{T_{wall}-T}{T_{wall}-T_{inlet}} = \exp\left(-4 \cdot 3.66 \frac{\alpha L}{\bar{u} d^2}\right) \tag{4.5}$$

where T is the bulk temperature, α the thermal diffusivity, L the channel length, d the channel diameter, and $\bar{u}$ the mean bulk flow speed [62]. The equivalent solution of mass diffusion with a constant wall concentration is:

$$\frac{x_{i,wall}-x_i}{x_{i,wall}-x_{i,inlet}} = \exp\left(-4 \cdot 3.66 \frac{D_i L}{\bar{u} d^2}\right) \tag{4.6}$$

where x_i is the molar concentration of the i^{th} component in the vapor phase (bulk average), and D_i is the mass diffusivity of the i^{th} component. For the light alkanes used as refrigerants, the mass diffusivity ranges from 0.015 cm^2/s to 0.032 cm^2/s, as calculated by Chapman-Enskog theory [63]. According to Equation 4.6, using D_i=0.015 cm2/s, d=1.5 mm, and $\bar{u}$ =2.9 cm/s (corresponding to 10 sccm with a vapor density of 0.147 mol/L calculated with REFPROP), the term $\frac{x_{i,wall}-x_i}{x_{i,wall}-x_{i,inlet}}$ will be <1% after traveling through 1.5 cm of tubing. At $\bar{u}$ =37 cm/s (corresponding to 126 sccm), 20 cm of tubing are required. Still, that length of tubing is present in the pre-cooled channels, and the bulk vapor concentration at the MCC can be assumed to be that of the vapor in VLE.

The vapor concentrations at VLE are a function of temperature and pressure and species,

but only a very weak function of concentration. Therefore, we can assume that the concentration of each component flowing through the MCC is always the same concentration, given by a VLE calculation, regardless of the concentration at the compressor.

To confirm that the composition through the MCC is indeed different from the original mix, we performed a separate test to sample the refrigerant that passed through the MCC. The modified test setup is shown in Figure 4.7. In this test, the refrigerant was compressed, passed through the filters and pre-cooled lines, passed through the heated MCC where it experienced isothermal expansion, and then was collected. During an initial period, valve 4 is closed and valve 3 is open, such that the system runs in a closed-cycle and allows the high pressure to build up. Once the system reaches its equilibrium high-pressure, valve 3 is closed and valve 4 is open, and the system runs in an open-cycle capacity while a 300 mL sample is collected. Three samples were taken at 295K, 272K, and 250 K, during steady flow. The high-pressures that the compressor was able to generate during these 3 tests were 0.397 MPa, 0.375 MPa, and 0.336 MPa, respectively. The collected refrigerant was analyzed with gas chromatography/thermal conductivity detection (GC/TCD), with results shown in Table 4.1. Also included in Table 4.1 are the compositions of the vapor components, calculated with REFPROP. The calculated values show generally very good agreement with the measured values.

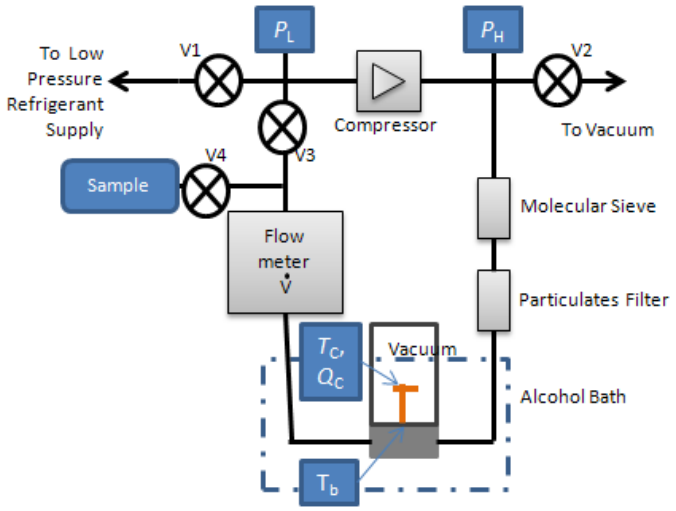

Figure 4.7: Modified test set-up, to sample the refrigerant mixture that passed through the MCC.

	295 K at 0.397 MPa		273 K at 0.375 MPa		250 K at 0.336 MPa	
	Measured	Caluclated	Measured	Calculated	Measured	Calculated
Methane	10.15	10.14	11.71	12.13	13.78	15.06
Ethane	55.93	56.58	63.12	64.29	69.71	70.22
Propane	16.30	16.02	16.95	15.81	14.18	12.21
Butane	3.69	3.45	2.82	2.22	1.21	0.93
Pentane	13.82	13.81	5.37	5.55	1.11	1.58

Table 4.1: Molar percentages of refrigerant mixture collected during steady flow at 295 K, 273 K, and 250K, determined by GC/TCD analysis. Compositions of the vapor portion of the mixture are included, as calculated by REFPROP at the temperature and pressure specified.

4.4.3: Charging time

An interesting result of this liquid hold-up in the high-pressure channels is that it takes a long period of time to build up the highest pressure in the high-pressure channels. This phenomenon has been observed in the initial start-up period of MCC operation, as in Figure 4.7. This section develops a model to explain the time required to reach the high pressures.

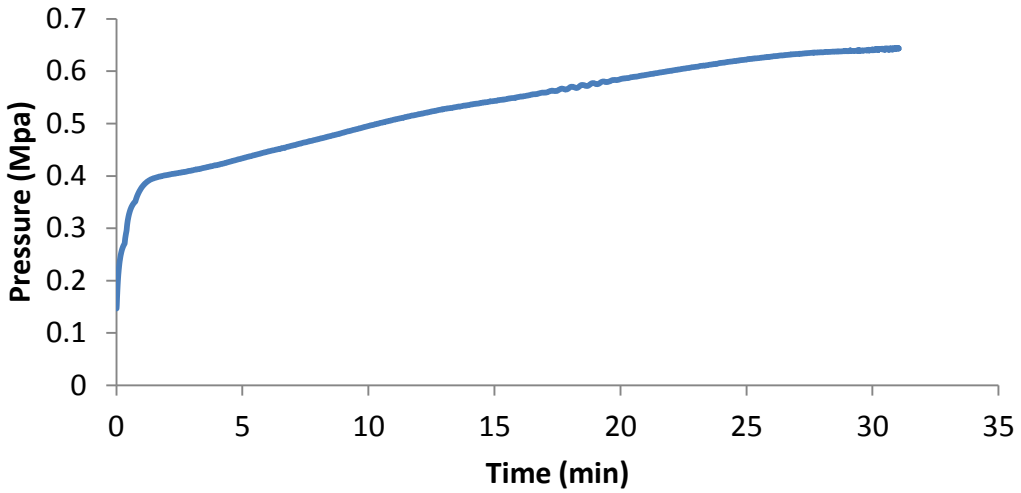

Figure 4.8: The initial period of MCC operation. After the refrigerant lines were evacuated and charged with refrigerant at 0.100 MPa, the compressor was turned on at t=0. A period of 30 min was required before the high-pressure reached an equilibrium value of 0.64 MPa. The low-pressure in this test was regulated at 0.14 MPa. The MCC used in this test had a J-T valve gap of 1.7 micron, allowing a flow-rate of 37.8 sccm at the highest pressure.

The two MCCs used thus far in this chapter represent the two extremes in flow-rate. Typical MCC operation has a flow-rate in the range of 10-30 sccm. Consider the initial pressure build-up of an MCC operating this mixed refrigerant which has a nominal flow-rate of 30 sccm with a high pressure of 0.4 MPa and low pressure of 0.1 MPa. The flow-rate through the MCC increases whit increasing pressure-drop across it. As was shown in Chapter 3.2.1, the flow through the compressor is a function of the pressure generated at the compressor and the compressibility of the refrigerant in question.

Without pre-cooling, the refrigerant that enters the MCC is given by the vapor components of the mixture at the high pressure. The composition of this vapor mix will be a function of pressure. It will be shown in section 4.4.5 that whatever components enter the MCC will also exit it regardless of cold-tip temperature. The low-pressure lines are initially filled with the original mix, but after refrigerant flows through the MCC, the low-pressure lines will be a

combination of the original mix and the vapor-component mix. This new combination of gasses will have a compressibility closer to 1, and the compressor will be able to generate higher pressure. Eventually, only the vapor-component mix will be in circulation, and all of the liquid-components will be held-up as a film in the high-pressure channels.

This argument is made quantitative by modeling a conservation of moles in the vapor-phase of both the high-pressure lines and low pressure lines, as a function of time. The mathematical details of the model are presented in Appendix B. Figure 4.9 b-d shows the development of (a) pressure, (b) flow-rate through the MCC, (c) low-pressure composition, and (d) molar fraction of liquid in the high-pressure lines, as a function of time.

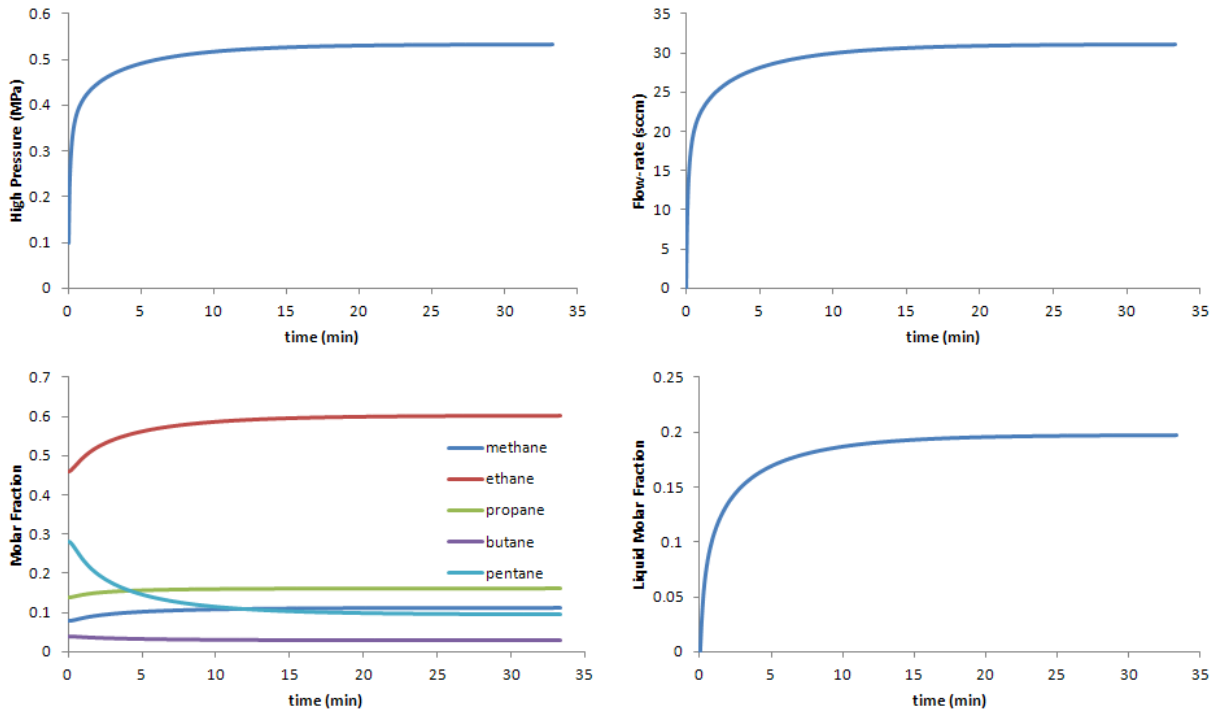

Figure 4.9: The development of (a) pressure, (b) flow-rate through the MCC, (c) low-pressure composition, and (d) molar fraction of liquid in the high-pressure lines, as a function of time. Note that the final liquid fraction is 0.2, which is low enough that the liquid remains in film-flow, according to a flow-regime model presented in [15].

4.4.4: Other Refrigerant Mixtures.

To verify that liquid hold-up of this nature is the general rule with refrigerant mixtures, a similar composition measurement was performed with the other 3 refrigerant mixtures discussed in Chapter 3.3. The results are shown in Figure 4.10.

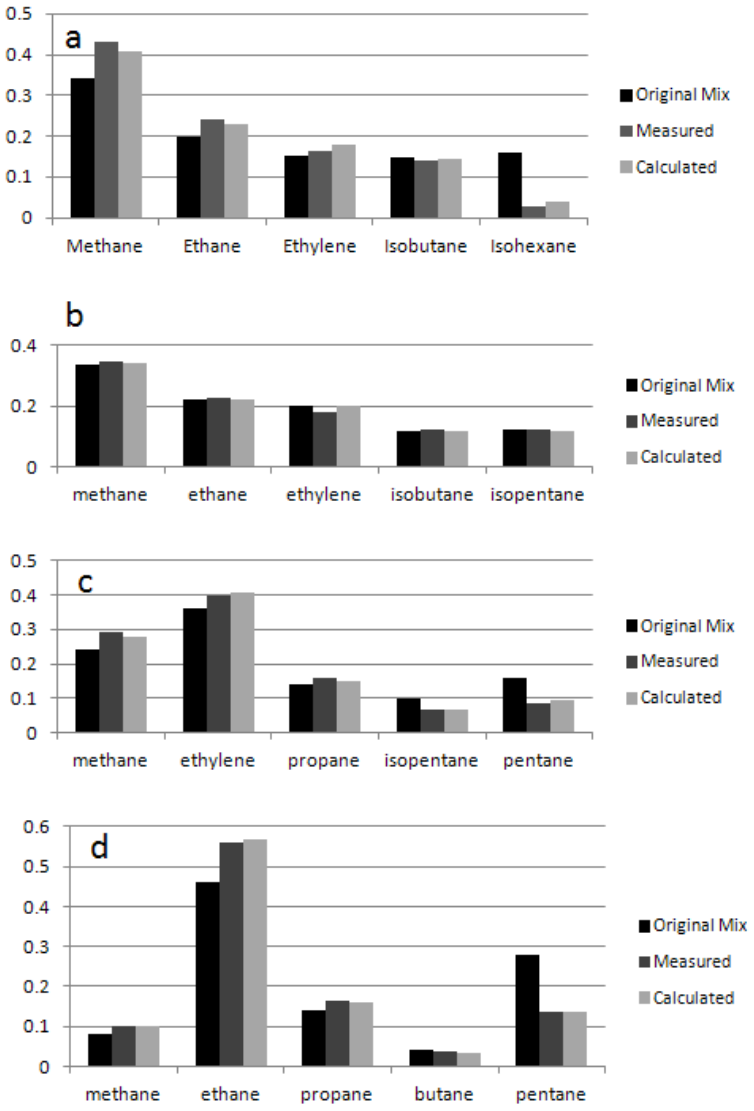

Figure 4.10: Measured of refrigerant passing through the MCC with no pre-cooling, of a) Mix 1 "140K Mix", b) Mix 2 "275K Mix", c) Mix 3 "160K Mix," and d) Mix 4, "200K Mix". Note that the results plotted in (d) are repeated from Table 4.1. Note also that in case (b) no composition change is expected for Mix 2 because no fraction of that mix liquefies at 295 K for P<0.6 MPa.

4.4.5 Non-isothermal performance

Consider operating the MCC with Mix 4 (“200K mix”) without pre-cooling. If According to this analysis, the refrigerant that reaches the MCC inlet will have a molar composition of 10.5% methane, 58.2 % ethane, 16.0 % propane, 3.2 % butane, and 12.0% pentane. The isothermal enthalpy difference of this mixture as it expands from 0.45 MPa to 0.100 MPa is plotted in Figure 4.7. Note that the minimum in this case occurs at the warm-end, and has a value of 317 J/mol. At 125 sccm, the cooling power of an MCC running this refrigerant is 29 mW, and given a background heat leak presented in Chapter 3.5.5, the MCC could reach 214 K when the active cooling balances the background heat leak. However, at this high flow-rate we also expect some cooling loss due to imperfect heat transfer. Performing the heat exchanger effectiveness calculation from Chapter 3.3, at a length of 25 mm, the total refrigerant losses reaches 60% of the total cooling power at T=250 K, which is where we see the MCC cooling to.

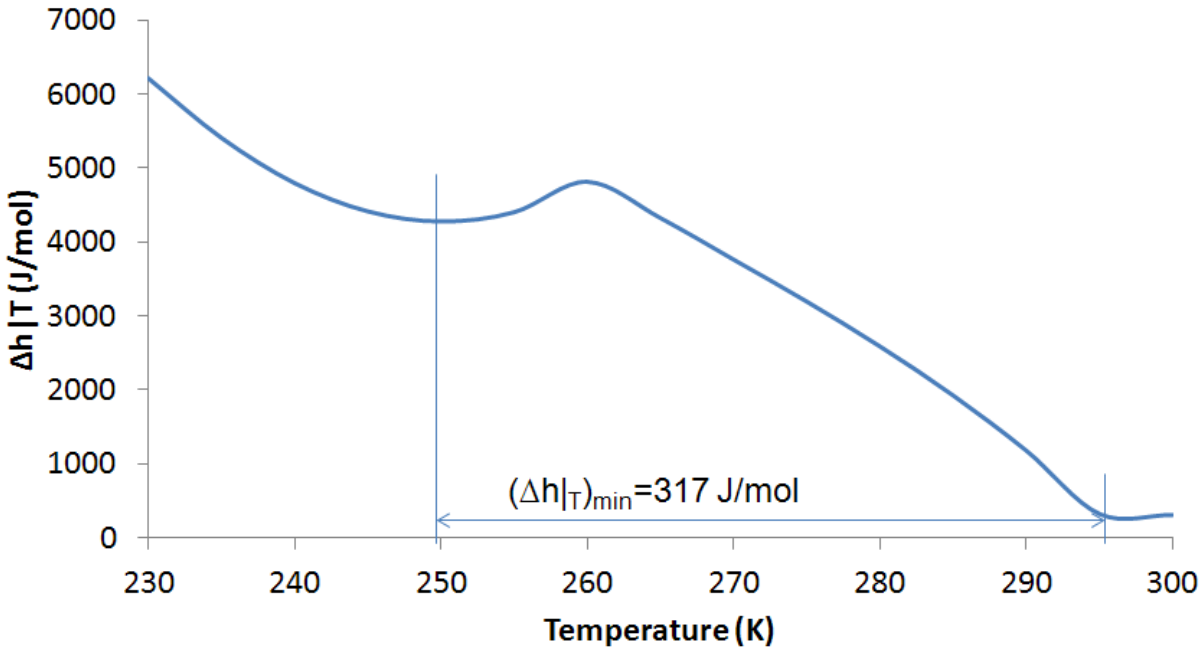

Figure 4.11: Isothermal ehtlapy diffrerence plot of a refrigerant mixture whose composition is determined by the vapor-phase composition of Mix 4 (“200K Mix”) in VLE at 295 K and 0.45 MPa. Note the minimum value occurs at 295 K with 317 J/mol.

For an MCC operating without pre-cooling, with an inlet temperature of 295 K and a cold-tip temperature of 250 K, when the refrigerant enters the fiber micro-channels it will cool down and some of the mixture will condense on the side-walls. The liquid would at first form a film, but if the liquid is held-up, eventually more and more liquid would be deposited on the walls, and the film would grow in thickness. This film growth occurs very quickly due to the small surface of the micro channels. With a thicker film, more of the liquid would flow through the MCC. With a thick enough film, a comparable amount of liquid would flow through the MCC as is deposited as a film, and the film thickness would reach equilibrium. In such equilibrium, the composition change in the MCC would be very small. This idea is verified by measuring the composition of refrigerant passing through the high-flow-rate MCC with an inlet temperature of 295 K, and a cold-tip temperature of both 250 K and 295 K. Before measuring the composition, the refrigerant was allowed to equilibrate over a period of 10 min. The results are shown in Figure 4.12. Note that in the case of the 250 K cold-tip measurement, there is some depletion of pentane and a small enrichment in lighter components. Still, both measured compositions are in agreement with a calculation of liquid holdup at 295 K.

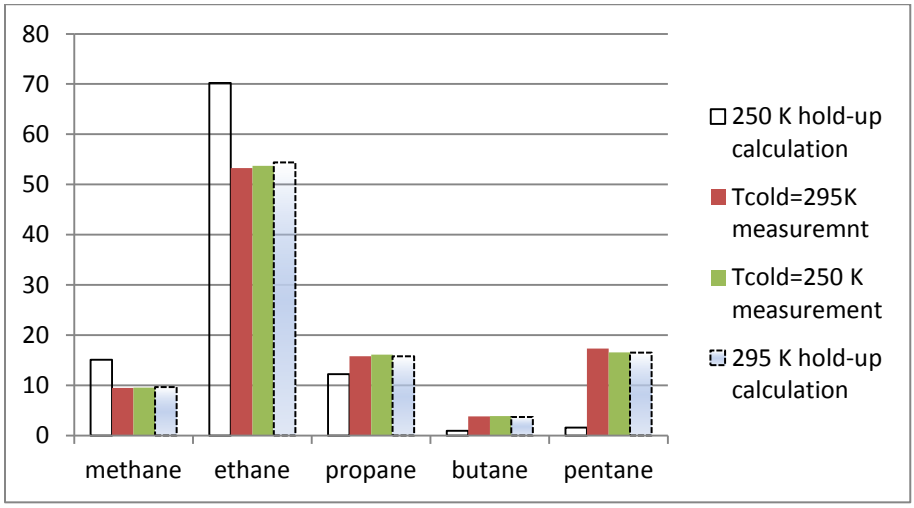

Figure 4.12: The composition of refrigerant passed through an MCC with a warm temperature of

295K, and a cold temperature of (red) 295 K and (green) 250 K. Note that the measured compositions are in much better agreement with a calculation of 295 K liquid hold-up (dotted outline) than 250 K liquid hold-up (solid outline).

4.5 Conclusions

The conclusions of this chapter are summarized as follows:

- This chapter demonstrates a method to measure the enthalpy difference of a mixed refrigerant in a J-T MCC.
- The measurement shows an order-of-magnitude difference between the enthalpy change of refrigerant in a steady flow regime and that of the original mixture.
- The measured low cooling power for steady flow agrees well with values calculated by the expansion of a mixture dominated by the vapor components of the refrigerant, as predicted by an annular flow pattern in which low flow-rates of liquid prevent the liquid components from contributing to the cooling. This liquid hold-up is verified by measuring the refrigerant composition with GC/TCD. Liquid hold-up is also verified in the other 3 low-pressure mixtures with a similar GC/TCD measurement. One consequence of such liquid hold-up is an extended period of time during which the pressure in the high-side lines develops.

Chapter 5 will investigate the pulsating flow regime, and develop a model of the pulses as liquid slugs developing in the small-scale pre-cooled lines. The model will be compared with both isothermal and non-isothermal specific cooling powers and show excellent agreement.

CHAPTER 5: STUDY OF PULSATING FLOW

Micro cryogenic coolers can provide low temperatures with smaller volumetric footprint and smaller power draw then their conventional-scale counterparts. But they can exhibit lower-than-desired cooling power. We measure the specific cooling power of a refrigerant expanding from a high pressure of 0.6 MPa to a low pressure of 0.1 MPa, while undergoing pulsating flow in a micro cryogenic cooler with pre-cooling. We further observe that the pulses in the flow-rate occur due to a volume of liquid forming in the high-pressure coupling mini-channel. The composition of the flowing refrigerant is analyzed with gas chromatography and thermal conductivity detection (GC/TCD), showing that there is no overall composition change in the refrigerant after it enters the pre-cooling lines. A model of the cooling power under such a pulsating flow regime is developed with good agreement to measured values. An improved refrigerant mixture is designed with this model, and subsequently tested, showing specific cooling power increasing.

5.1 Introduction

Refrigerant mixtures can increase the specific cooling power of a refrigerant compared to a pure refrigerant if the composition of the mixture is optimized. Operating with a well-designed refrigerant allows Joule Thomson (J-T) coolers to reach cryogenic temperatures with typical working pressures of 2.0 MPa. Such refrigerant are non-azeotripic mixtures of hydrocarbons, hydrofluorocarbons, nobel gasses, and nitrogen [18]. However, the composition of the mixture can change, for example due to preferential leaks and preferential dissolution in compressor lubricants. A leak-free and oil free system will eliminate those problems, but because the mixtures are non-azeotropic liquid hold-up will also change the overall composition [37]. Narasimhan and Venkatarathnam developed a method to compensate for the composition shift in

macro-scale (10 W) J-T coolers [38].

When coupling a J-T micro cooler to a mini or micro-scale compressor, the maximum discharge pressure of the compressor is limited to well below 2.0 MPa. Chapter 3 has shown that a J-T micro cooler can achieve temperatures of 200 K when connected to a compressor with a discharge pressure of 0.6 MPa and suction pressure of 0.1 MPa, when the cooler is pre-cooled to 273 K. In such low-pressure operation the flow-rate of the system will either experience steady flow or pulsating flow. In both cases, the cooling power of the refrigerant has been measured to be lower than calculated. For steady flow, it has been shown in the last chapter that the refrigerant mixture composition will change due to hold-up of the liquid components in the macro-scale pre-cooled channels. However, pulsating flow requires further investigation.

It should be noted that this pulsating flow regime is different from other sources of cooling instability reported for J-T micro coolers. Previous MCC reports show that instability can be a result of clogging in the Joule-Thomson valve due to solid formation [46, 64]. In macro-scale J-T coolers, ice can form clogs from trace moisture contaminants; a maximum of 2 parts per million (ppm) of water contaminant is recommended as a critical upper concentration [64]. However in MEMS-scale channels, such as those used by Lerou et al [46], contaminant concentrations of 0.16 ppm still let to ice formation. In the present work, ice clogging is not the cause of pulsation, as is evident by the existence of pulsating flow at temperatures above 273 K. Another often cited cause of occurs due to a surplus of cooling power, which can lead to excess amounts of liquid forming downstream of the J-T valve [65], which leads to unsteady liquid flow in the low-pressure channels, and associated high-frequency low-amplitude temperature oscillations. This sort of flow was observed by Burger et al. with liquid ethylene in his coaxial heat exchanger [43]. The pulsating flow experienced by the MCC under investigation is different

as it corresponds to intermittent liquid flow across the J-T valve, as reported in Chapter 3 (see Figure 3.20), rather than down-stream of the J-T valve.

This chapter explores the pulsating flow regime of micro coolers by performing a visualization analysis study of refrigerant vapor/liquid 2-phase flow in the heat exchanger of the micro cooler, by measuring the isothermal enthalpy change of the refrigerant at different temperatures, and by measuring the composition of the refrigerant. Based on this analysis, a model of pulsating flow will be presented that considers each pulse to be a slug of liquid that forms in the large pre-cooling channels and fills the micro-channels of the micro-cooler. Such slug-based separation leads to a new method to calculate the specific cooling power of a refrigerant mixture, and this new calculation method is verified by designing and testing a modified refrigerant mixture with an increased cooling power.

5.2 Materials and Methods

The micro cryogenic cooler (MCC) used in this experiment was described in Chapter 3.1, but its design and operation is briefly repeated: It operates under the Joule-Thomson cycle whereby compressed refrigerant enters the high pressure channels of a counter-flow heat exchanger (CFHX), expand to low pressure across a restriction (referred to as the "J-T valve") thereby cooling, and the cooled refrigerant returns though the low-pressure channels of the CFHX before returning to the suction port of the compressor. The MCC used for these tests uses 6 hollow-core glass fibers (ID/OD=75/125 μm) as the high-pressure channel of the CFHX. The fibers are held in a capillary (ID/OD= 536/617 μm), and the interstitial space between the fibers within the capillary forms the low-pressure channel of the CFHX. The J-T valve is formed by anodic-bonding an etched silicon chip to a borosilicate glass chip. A gap etched into the silicon,

measuring 1.5 μm in height provides the flow restriction. This MCC is shown in Figure 5.1. Details on the fabrication and assembly of this device are described in Chapter 3.1. Typically, the outer diameter of the capillary is coated in gold to decrease radiative heat loads. However, in order to facilitate the visualization experiment, a MCC without the gold coating was assembled, as shown in Figure 5.1c. The warm-end of the CFHX is connected to a macro-coupler, which is fastened to a base-plate flange, as in Figure 5.1d. The base-plate flange allows the MCC to be placed in a vacuum using standard vacuum fittings.

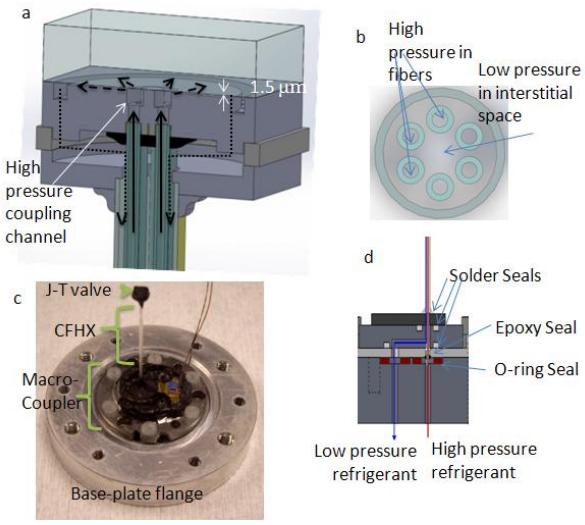

Figure 5.1: The MCC used in these tests. a) cross-sectional drawing of the J-T valve, showing path of the refrigerant as it expands from high pressure (solid line) to low pressure (dotted line), b) cross-section of the CFHX, c) photograph of a MCC assembled without gold coating, d) drawing showing assembly of the MCC to the base-plate flange.

The compressor used in these experiments was formed from a commercial piston-oscillator coupled to custom micro-fabricated check valves, as described in Chapter 3.2. The experimental set-up is shown in Figure 5.2. The major difference between this experimental set-up and the one described in Chapter 3.4 is the location of the high-side pressure transducer, the addition of refrigerant collection reservoirs, and the addition of a high-speed camera. The high-side pressure transducer is placed to measure the pressure of the refrigerant after the passing

through filter and sieve. The refrigerant then travels through roughly 40 cm of copper tubing (ID/OD=1.4/3.2 mm), of which 20 cm is held in a pre-cooled bath, before reaching the MCC. Downstream of the MCC, the flow-rate of the refrigerant is measured with a mass flow-meter. The MCC is held under a vacuum of 1-10 Pa (10^{-5}-10^{-4} Torr), which ensures that any heat loads due to convection or conduction through the air are negligible.

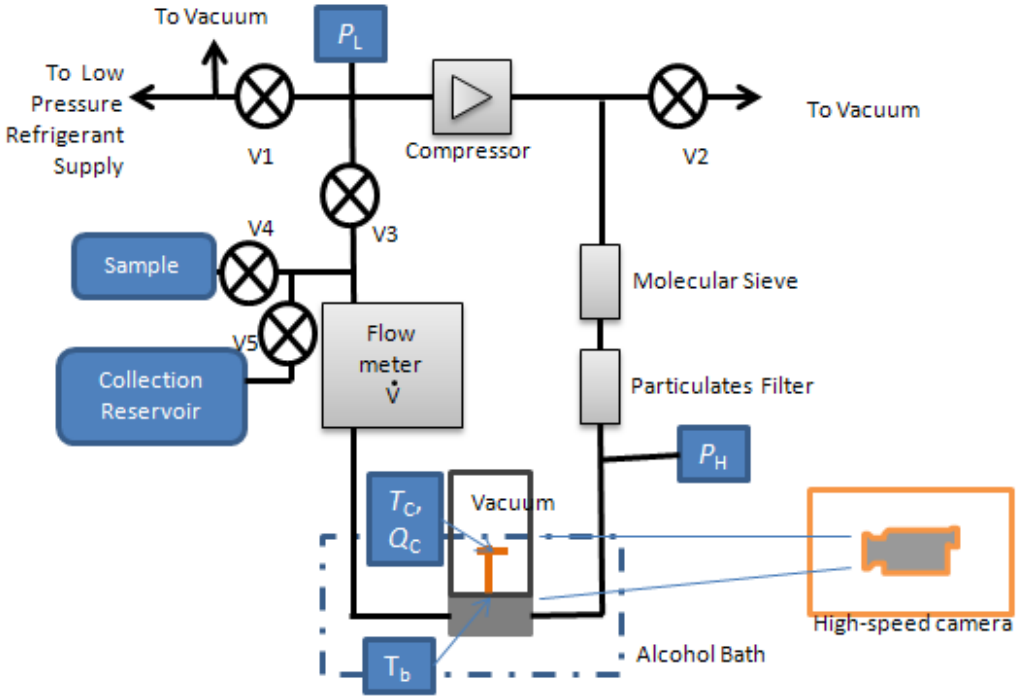

Figure 5.2: schematic of the test set-up. Measured data include: High pressure (P_H), Low pressure (P_L), Flow-rate ($\dot{V}$), MCC base temperature (T_B), MCC cold-end temperature (T_c), and heat into the MCC cold-end (Q_c).

As in experiments detailed in previous chapters, before running the compressor, all refrigeration lines are evacuated to 10 Pa (10^{-4} Torr). Mixed refrigerant regulated at 0.1 MPa is fed to the suction port of the compressor and allowed to pass through the compressor check valves such that the system starts with an internal pressure of 0.1 MPa. When the compressor is turned on, the high-pressure takes a period of time to develop. During this initial starting period, the system experiences steady flow-rates. If no pre-cooling were applied, the steady flow regime

would persist as detailed in the previous chapter. However, if pre-cooling is applied to the MCC base-plate flange, then after a period of time the flow will transition to a pulsating regime. This period of time is discussed in section 5.4.3.

For the visualization study, only the base-plate flange is pre-cooled. A high-speed visual camera with frame-rates up to 10,000 fps is connected to an optical microscope, and captures the movement of liquid in the fibers of the heat exchanger and in the J-T valve gap. It was found that operation at frame rates higher than 2,000 fps required illumination that posed an unacceptable heat load to the MCC.

The composition of the refrigerant was measured with gas chromatography and thermal conductivity detection (GC/TCD) at a commercial natural gas analysis lab [66]. Samples of refrigerant were taken by closing Valve 3 (shown in Figure 5.2), and slowly opening the valve to an evacuated bottle. During the initial start-up period of the test, refrigerant was collected in a low-pressure reservoir by opening Valve 5. Once pulsations developed and continued for 10 min, the refrigerant was collected into the sample bottle by closing Valve 5 and opening Valve 4. Three samples were collected in this manner: one with 255 K pre-cooling and pulsations, another with 275 K pre-cooling with pulsations, and one with neither pre-cooling nor pulsations.

To measure the isothermal enthalpy change of the refrigerant, the method described in Chapter 4.2 is applied. The MCC is shrouded in a radiation shield, and a platinum resistance thermometer is mounted onto the J-T valve. The vacuum package and 20 cm of coupling line is held in an alcohol bath to pre-cool the MCC macro-coupler and incoming refrigerant. The temperature at the J-T valve, macro-coupler, and radiation shield are all monitored. A small voltage is applied to the PRT at the J-T valve, causing it to heat up. The voltage is controlled such that the temperature of the J-T valve is increased to that of the macro-coupler. That required

heat gives the net heat load to the MCC. Adding net heat to parasitic loads due to radiation and conduction gives the gross cooling power. Dividing the gross cooling power by the molar flow-rate yields the specific isothermal enthalpy difference of the mixture at the J-T valve temperature. Each isothermal enthalpy measurement is taken at a single alcohol bath temperature, and measures the applied heat over at least 6 pulsation cycles, which takes 5-10 min. Afterward, the alcohol bath temperature is changed, and the next data point is measured.

Three of the four refrigerant mixtures from Chapter 3.3 were studied in this test: Mix 1 "140K Mix," Mix 3 "160K Mix," and Mix 4 "200K Mix." Mix 2 ("275K Mix") was not used in this study because with the MCC used, the time required to generate pulsations was prohibitively long. The compositions are the 3 mixtures used are repeated in Table 5.1. Recall that the gross cooling power of a Joule-Thomson cooler is given by the product of the flow-rate ($\dot{n}$) with the minimum isothermal enthalpy difference between the high-pressure stream and low-pressure stream, minimized across the temperature range experience by the heat exchanger: $(\Delta h|_T)_{min}$ [24]. The composition of the 3 mixtures was chosen to maximize $(\Delta h|_T)_{min}$ between a high pressure of 0.4 MPa and a low pressure of 0.1 MPa, over the listed temperature range. The program NIST4, which uses thermophysical properties calculated with the NIST software SUPERTRAPP was used to perform the optimization [68]. The $\Delta h|_T$ curves for each mixture are plotted in Figure 5.3.

200K Mix	140 K Mix	160 K Mix
8 % methane	34 % methane	24 % methane
46 % ethane	20 % ethane	36 % ethylene
14 % propane	18 % ethylene	14 % propane
4 % butane	16 % isobutnae	10 % isopentane
28 % pentane	12% isohexane	16 % pentane

Table 5.1: the compositions of the 3 mixtures studied for isothermal enthalpy difference tests.

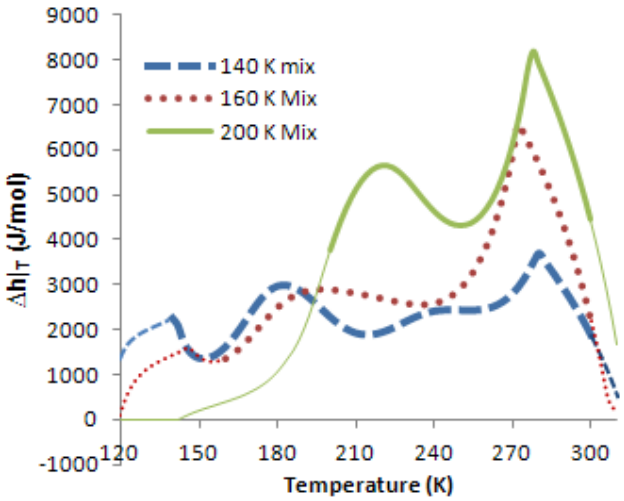

Figure 5.3: isothermal enthalpy difference curves of the 3 mixtures used in the enthalpy measurement test. The regions where the refrigerant was designed to operate are shown in bold in the figure.

5.3 Results

5.3.1 Two-phase flow visualization

During the visualization tests, radiative heat loads prevented the MCC cold-end to cool below 280 K during steady flow, even with the MCC base cooled to 273 K. During steady flow, no

liquid is observed in the fibers. After nearly two hours the first pulse in flow-rate occurs. Each pulse in flow-rate is accompanied by an increase in cooling performance, as shown in Figure 5.4, with a minimum temperature of 245 K.

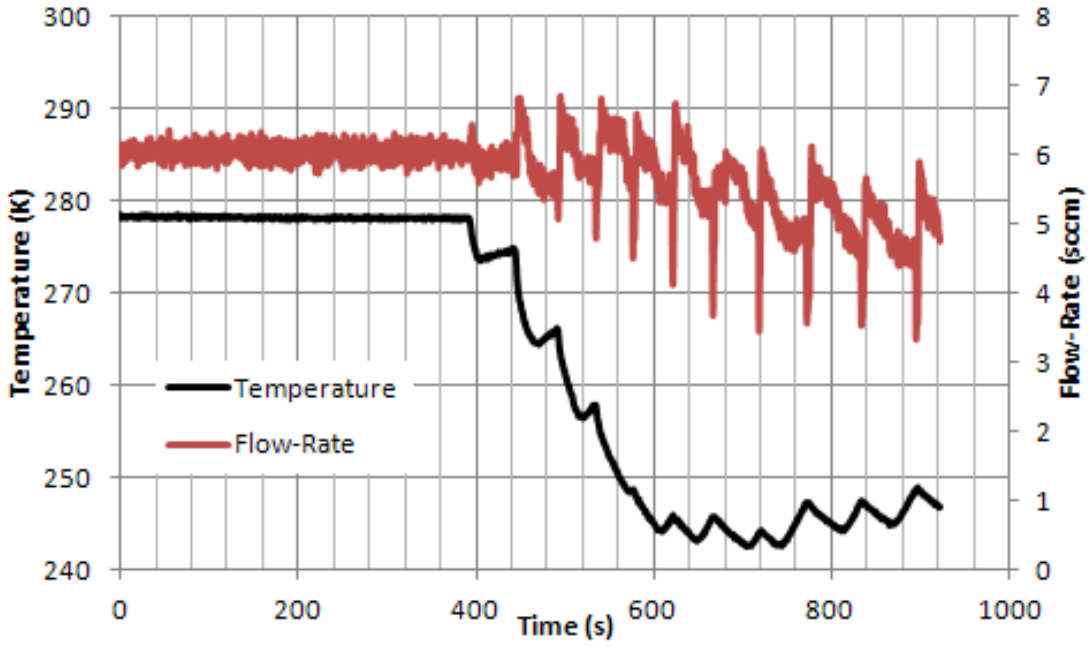

Figure 5.4: Temperature curve (black) and flow-rate curve (red) of the MCC as it experiences its first pulses during visualization studies. Note that each pulse in flow-rate brings about greater cooling.

The observed flow patterns in the fibers are as follows: first, the fiber is in single-phase liquid flow. The abruptly a front of liquid passes into the fiber from the macro-coupler and fills the fiber with liquid. This corresponds to the pulse in the flow-rate. The fiber experiences single-phase liquid flow for a short period of time, after which there is a transitional period that contains 2-phase flow, in the form of vapor bubbles, small slugs of liquid, or liquid slug-annular rings. After a period of this 2-phase flow, the fiber dries out and experiences single-phase vapor flow again, and the cycle repeats. Such flow-patterns are shown in Figure 5.5.

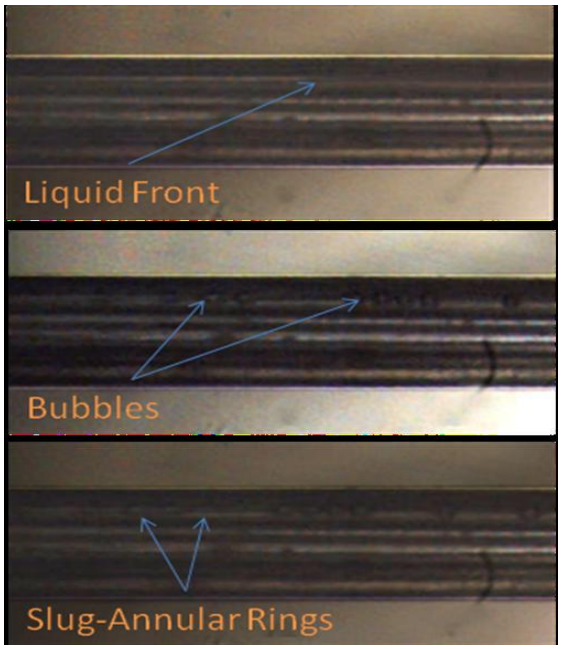

Figure 5.5: flow-patterns observed during pulsating flow. a) liquid front in the fiber, b) bubbles and c) slug-annular rings during the transition from liquid flow to vapor flow.

The speed of the liquid front as it passes through the fibers was determined from the video data to be 7.44 mm/s on average, which agrees well with a speed calculated from the ratio of molar flow-rate with density-times-area: $v = \dot{n}/\rho A$. Here density is calculated for the liquid components of the mixture at 273 K and 0.54 MPa.

Once a liquid pulse reaches the J-T valve, it quickly crosses the radial gap. But in the high-pressure coupling channel of the J-T valve chip, 0.14 μL of vapor will have to drain across the gap at the same time the liquid is flowing. As a result, liquid will not fully fill the J-T valve gap even if the fibers are experiencing single-phase liquid flow, as shown in Figure 5.6 a-d. After the liquid pulse passes through the J-T valve, some of the low-pressure channel will fill with liquid, shown in Figure 5.6f and g. The low-pressure liquid can travel down the CFHX, but once the fibers contain 2-phase transitional flow, the liquid front in the low-pressure channel will retreat back to the J-T valve, and will dry out. When liquid from the 2-phase transitional flow reaches the J-T valve, it crosses the gap in the form of an “exploding film” as shown in Figure

5.6e.

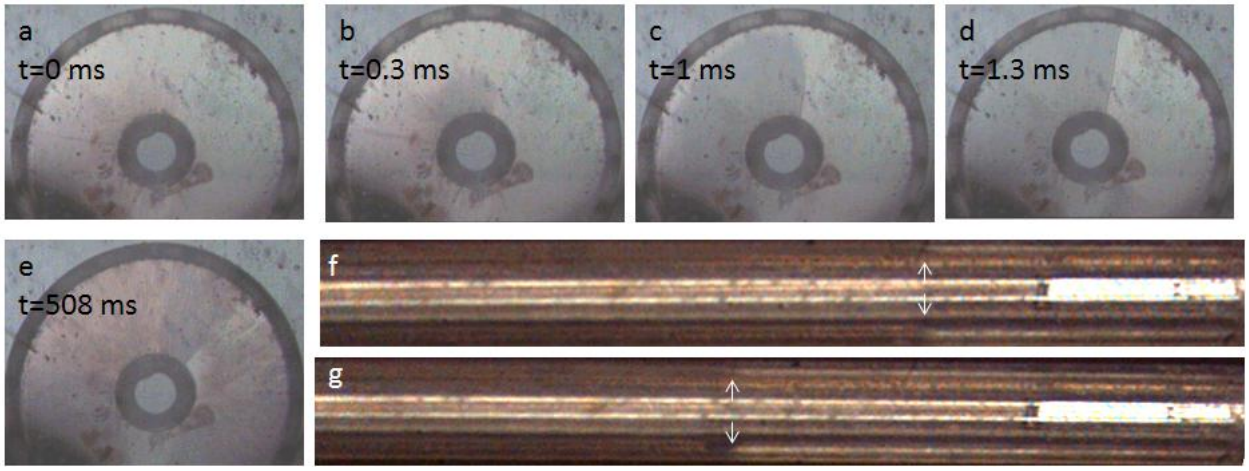

Figure 5.6: Liquid as it passes through the J-T valve and low-pressure channel. a-d) a liquid pulse crossing the J-T valve over 1.3 ms. Note that even when the liquid has fully crossed the J-T valve, some vapor will flow. e) "exploding film" as the flow transitions from vapor to 2-phase. f) and g) Liquid front advancing down the low-pressure channel of the CFHX.

The transitions between each of the flow regimes all appear in the temperature and flow-rate profiles, shown in Figure 5.7. Liquid-phase refrigerants tend to have the highest cooling power owing to the fact that they can evaporate. During the single-phase liquid flow, the cooling power is the highest, and the temperature of the MCC cold-tip drops. During the 2-phase transitional flows, the cooling power will slowly drop as less liquid flows, and the temperature will stop dropping and start to rise. During vapor flow, the cooling power of the refrigerant is quite low, so the temperature will rise. The transition from vapor flow to liquid flow is abrupt, and results in an abrupt change from rising temperature to falling temperature.

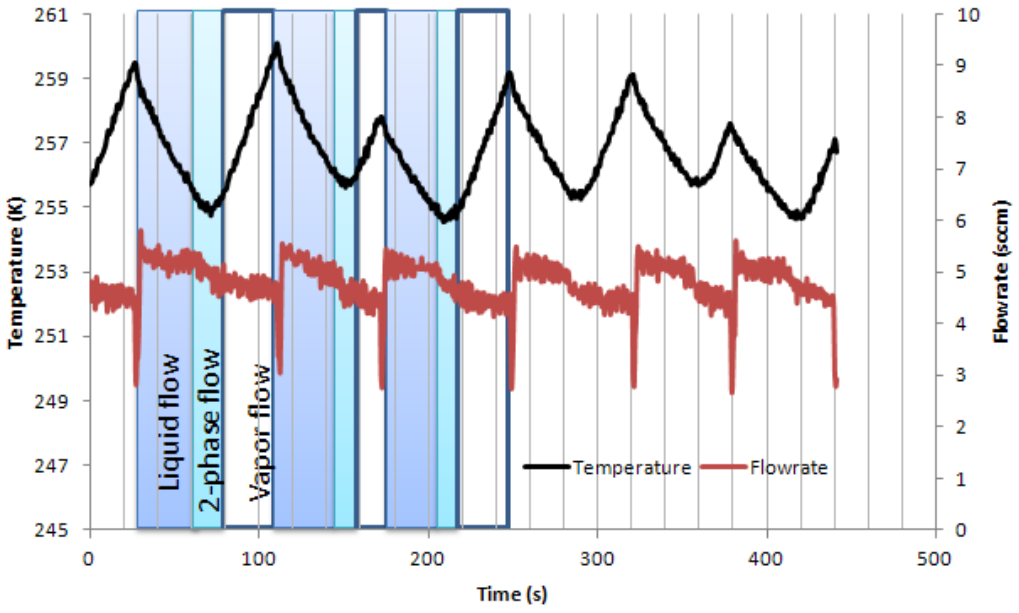

Figure 5.7: Temperature and flow-rate curves with liquid/vapor flow regime pointed out.

5.3.2 Isothermal Enthalpy difference measurement

The results of the isothermal enthalpy test are shown in Figure 5.8. The first refrigerant mixture considered was the "200K Mix." To measure the isothermal enthalpy difference the alcohol bath started at 280 K and the flow was steady. The bath was cooled down to 253 K over 1 hour, by which time pulses developed. After collecting data for 8 min at 250 K, the alcohol bath was then warmed in increments of roughly 5 K, while a $\Delta h|_T$ data point was measured at each temperature point ("Up 1" in Figure 5.8a). After the bath temperature reached 280 K, the bath temperature was dropped again in increments of ~5 K, and enthalpy points were measured, to ensure that hysteresis was not affecting the measured enthalpy data ("Down 1"). Finally, a second set of enthalpy data were measured while the temperature was increased in increments to 286 K ("Up 2"). During this data run, the typical high-side pressure was 0.594 MPa. Additionally, several weeks later the system was evacuated and re-charged with refrigerant, and the test repeated ("Up

3"). The enthalpy data are plotted in Figure 5.8. As in Chapter 2, the error bars on each point are taken as the standard deviation in $\Delta h|_T$ between each pulsation cycle. Also included in Figure 5.8 is the enthalpy change calculated by REFPROP for the original mixture (dotted line), the mixture after liquid hold-up at 295 K and 0.594 MPa (dashed line). The solid lines are calculated according to a method presented in Section 5.5.3. For the "200K Mix," the measured enthalpy data are somewhat lower than those calculated with the mixture after experiencing room-temperature liquid hold-up.

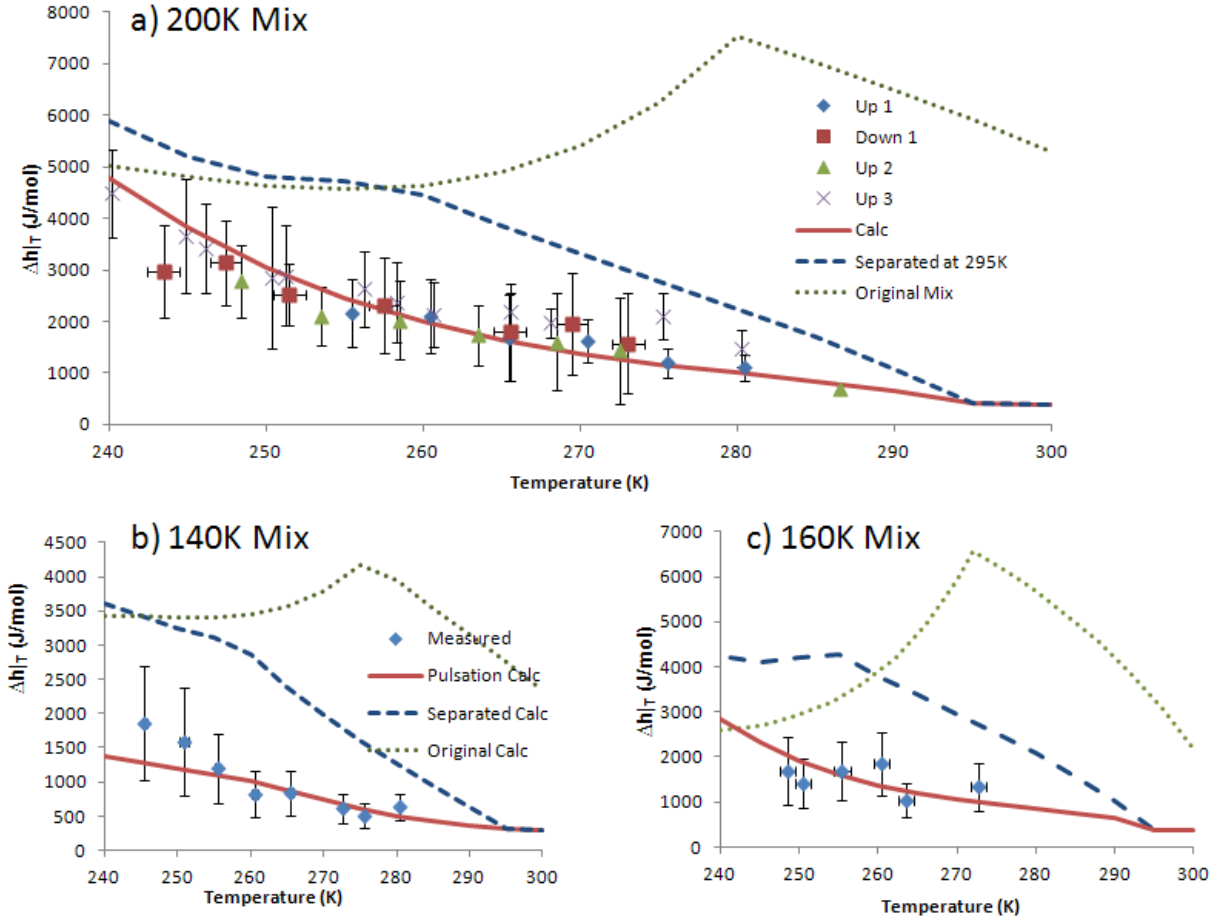

Figure 5.8: measured and calculated isothermal enthalpy differences of a) 200K Mix, b) 140K Mix, and c) 160K Mix. The dotted lines are calculations based on the original mixture, the dashed lines are calculations of the enthalpy difference after the liquid components of the mixture have been removed due to room-temperature liquid holdup, and the solid lines are calculations based on pulsing, as presented in Section 5.5.3

The isothermal enthalpy difference was also measured for the 160 K mix and 140 K mix, in Figure 5.8b and c. Note for these two mixtures, the measured enthalpy difference is considerably lower than that calculated for either the original mixtures or the mixtures after room-temperature liquid hold-up.

5.3.3 Non-isothermal Cooling Power

In cooling operation of the micro cryogenic cooler, there is a large temperature gradient across the heat exchanger. For a cooler experiencing a steady flow, the cooling power is given by the minimum in isothermal enthalpy difference within the temperature range experienced by the heat exchanger: $\dot{Q}/\dot{n} = (\Delta h|_T)_{min}$. With refrigerant experiencing pulsating flow, however, the cooling power may be different than this expression, and needs to be measured. The gross cooling power will be given by the sum of the applied cooling power (as in the previous section), and the parasitic heat loads. In this experiment, a second MCC was used which has gold-coated heat exchanger 20 mm in length. Two measurements of applied cooling power at various cold-tip temperatures were performed to demonstrate repeatability.

Because the MCC used in this section was shorter than the one used in Chapter 3.5.5, it will experience a different background heat load. To determine the parasitic heat loads, a background heat leak test was performed on the MCC with ice pre-cooling, similar to in Chapter 3.5.5. The heat leak test proceeds as follows: first the MCC cools to 195 K with the 200K Mix and ice pre-cooling. Second, a constant amount of heat is applied to the PRT. Simultaneously, the compressor is turned off and the high-side pressure is vented, such that the flow-rate through the MCC drops to zero and there is no active cooling. This will cause the temperature of the MCC to rise. Third, steps 1 and 2 are repeated with a different amount of heat applied to the PRT. The temperature rise rates are plotted against applied heat, at various temperatures, in Figure 5.9a.

Note that for each temperature, the rise-rate is linear with applied heat. Extrapolating to a rise-rate of 0, one finds a negative heat. This is the heat dissipated by the cooler in order for it to maintain that temperature—that is to say the parasitic heat load. The parasitic loads are plotted against temperature in Figure 5.9b. Data with temperatures below 230 K are influenced by transient heating effects, and do not accurately reflect the parasitic heat load, so they are not included.

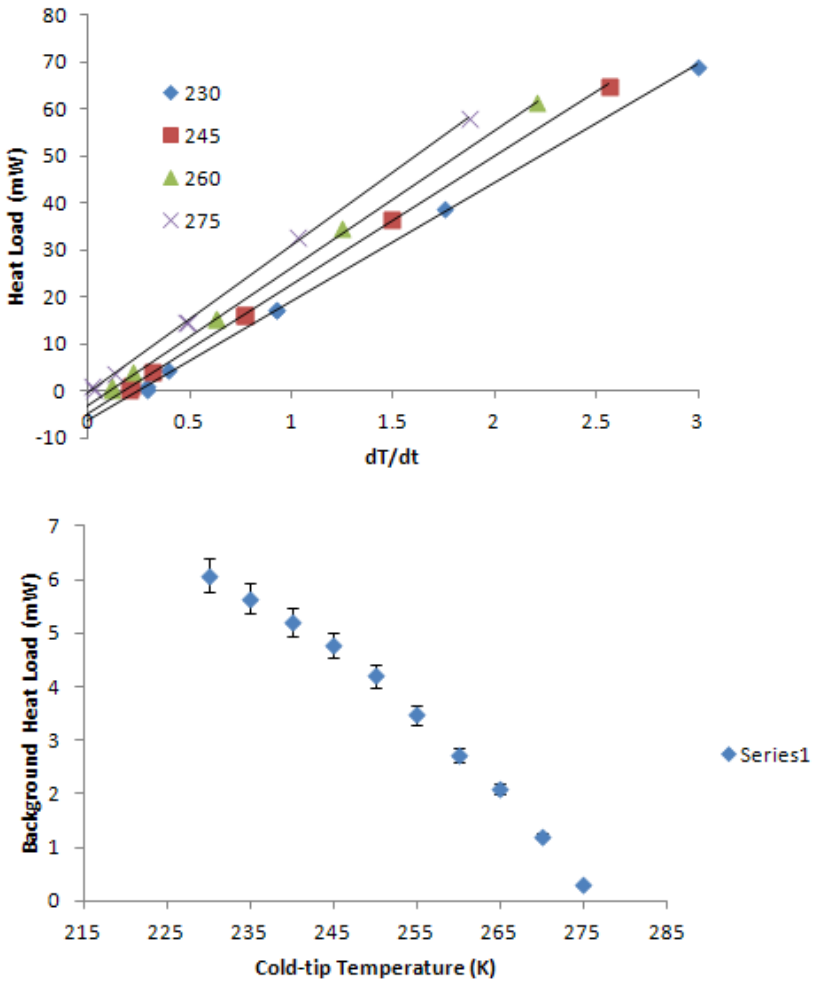

Figure 5.9: a) the heat loads plotted against temperature rise rate at 4 different temperatures, b) Measured parasitic heat loads as a function of cold-tip temperature.

Knowing the parasitic heat loads, the applied cooling power is found by cooling the MCC

to 200 K and stepping up the temperature by adjusting the hot set point, as in Figure 5.10a. The warm-end temperature for this measurement was kept at 273 K with the ice-bath. Finally, the specific cooling power is found by dividing the gross cooling power (sum of applied heat load and background heat load) by the flow-rate. The measured specific cooling power is plotted against cold-tip temperature in Figure 10b. The solid line in Figure 5.10b is the calculated isothermal enthalpy difference of the original mixture, and the dotted line is the $(\Delta h|_T)_{min}$ value of the original mixture with a warm-end temperature of 273 K, plotted against cold-end temperature.

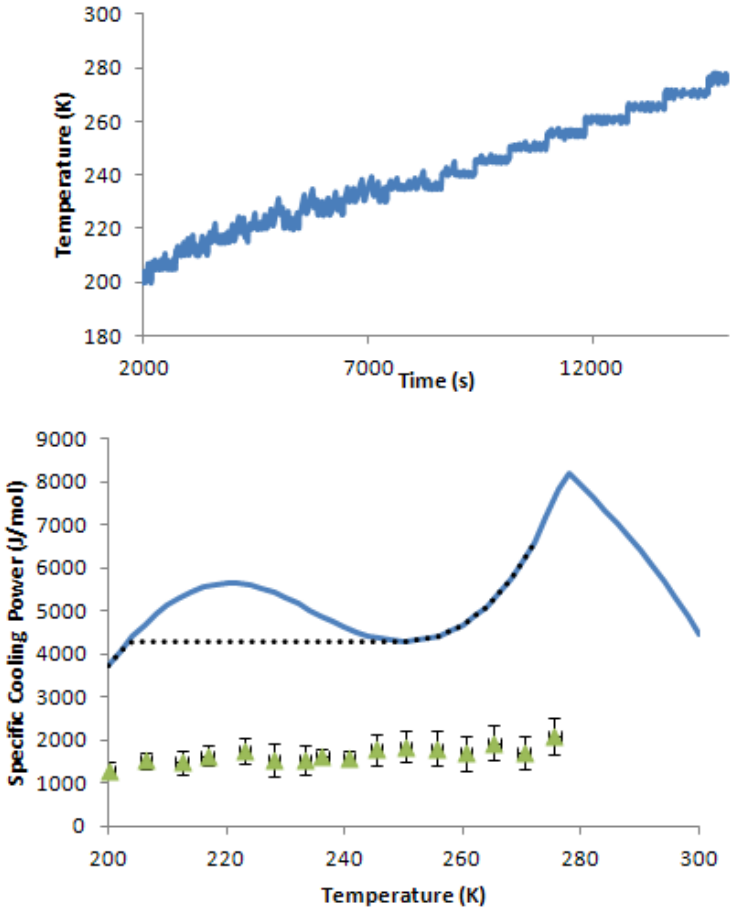

Figure 5.10: a) temperature profile as heat was added to increase the temperature in steps and

measure the cooling power, b) measured (triangles) and calculated (lines) specific cooling powers. Calculations are performed according to $\dot{Q}/\dot{n} = (\Delta h|_T)_{min}$.

5.3.4 Composition Analysis

Once the test set-up was modified to collect refrigerant for analysis, two runs of pulsating refrigerant collection were performed. In the first, the refrigerant was pre-cooled to 251 K with a high-side pressure of 0.355 MPa, and in the second the refrigerant was pre-cooled to 273 K with a high-side pressure of 0.360 MPa. During the first run, exposure of the macro-coupler in the MCC to low temperatures over a long period of time caused a hairline fracture in one of the epoxy joints in the macro-coupler, which caused a small leak rate in the MCC, resulting in a vacuum pressure of 20 Pa, rather than 10 Pa as desired. The leak rate was more drastic during liquid flow, increasing the vacuum pressure as high as 100 Pa during a liquid pulse. This selective leak introduced some uncertainty between the measured composition and the composition flowing through the MCC. The measured composition will have less of the heavy components that escaped through leakage. This uncertainty is captured with the error bars in Figure 5.11.

A third collection run was performed without pre-cooling under steady flow-conditions at 295 K and 0.38 MPa on the high-side. The resulting concentrations are shown in Figure 5.11. Note that the change in the concentrations at different levels of pre-cooling is very small, and that all concentrations agree well with composition of the vapor at 295 K and 0.4 MPa. This contrasts sharply with steady-flow in which the concentrations were a strong function of pre-cooling temperature, varying by up to 80%. It appears that liquid is still held-up in the room-temperature coupling channels, but with pulsations liquid is no longer held in the pre-cooled channels.

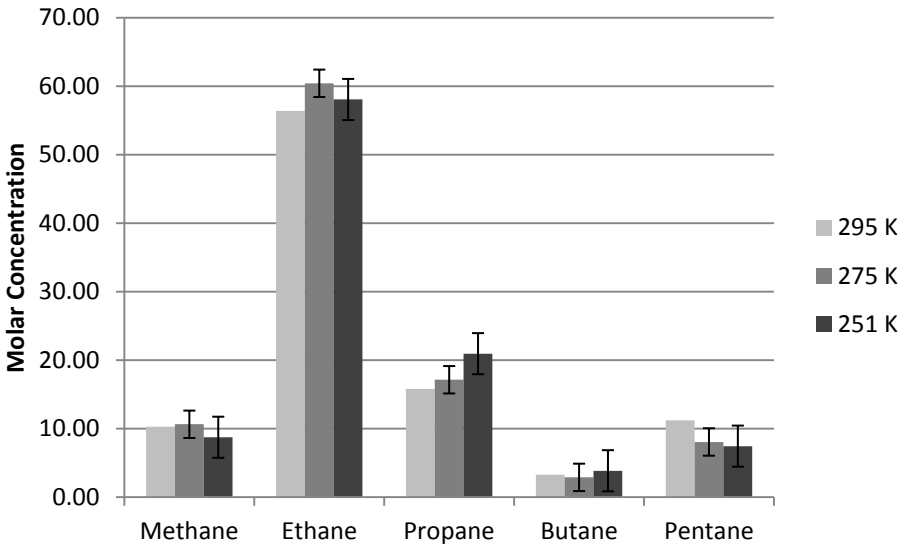

Figure 5.11: molar concentration of the 5 components in the 200K Mix after running with pre-cooling at 3 different temperatures.

5.4 Discussion

5.4.1 Pulses

According to the visualization data, pulses originate in the high pressure coupling lines, upstream of the MCC. According to the GC/TCD data, the bulk refrigerant during pulsating flow is the same as that which experiences complete liquid hold-up in the room temperature lines. These can be understood in terms of liquid slugs forming in the pre-cooled lines.

Consider a cool-down test of the 200K Mix. Initially the original mixture fills all of the refrigerant lines, at a pressure of 0.1 MPa. Once the compressor starts running, the high-side pressure builds up, and once it is above 0.206 MPa (the 200K Mix dew point at 295 K), liquid will start to form. The liquid will form along the walls in order to reduce surface energy. Due to a no-slip boundary condition along the walls, the liquid phase will move much slower than the vapor phase. For laminar annular flow, it has been shown that the liquid molar flux will be <0.01% of the vapor molar flux. As the pressure continues to build to 0.6 MPa, more of the

heavy components liquefy along the walls. Without pre-cooling, eventually all of the liquid components will be held along the walls, and only the vapor components will be in circulation. If the volumes of the high-pressure and low-pressure channels were equal and all of the liquid components present in the initial refrigerant charge were coated on the walls of the high-pressure channel, the molar liquid fraction in the high-pressure channel of:

$$X_h = \frac{P_h/P_l+1}{P_h/P_l+1+(P_h/P_l)(1-X_l)/X_l} \tag{5.1}$$

where X_h is the molar liquid fraction in the high-pressure channel, P_h the pressure of the high-pressure channel (0.6 MPa), P_l the pressure of the low-pressure channel (0.1 MPa), and X_l the liquid fraction of the refrigerant resulting from a flash equilibrium at the high pressure and ambient temperature (0.311 as calculated by REFPROP for the 200K Mix). At a pressure ratio of 6:1, Equation 1 yields X_h=0.345. Note that X_h will be larger than X_l because X_h includes liquefied components that originated in both the high-pressure channels and low-pressure channels.

However once the 295 K vapor reaches the pre-cooled lines, the temperature is below the dew point of the non-pre-cooled vapor components, so more liquid will form on the walls of the pre-cooled lines. As more of the refrigerant passed across the pre-cooled lines, the thickness of the liquid film will increase further. Eventually the thickness would reach a critical thickness, where surface tension in the radial direction overcomes inertia, viscosity, and surface tension in the axial direction, and the liquid film will form a slug of liquid.

Such a slug will have a volume of roughly: $V = 2/3\pi r^3$ which for a channel radius of 1.3 mm gives a slug volume of 4.6 μL. This is larger than the volume of the fibers in the MCC (0.57 μL), so the liquid can completely fill the fibers before any vapor enters the flow. The composition of the liquid will be governed by vapor-liquid-equilibrium (VLE) conditions. Once vapor enters the flow, the liquid that is already in the fibers take time to dry-out, and the fiber

experiences 2-phase flow. In this manner, eventually all of the modified refrigerant will pass through the MCC, just not all at once. First the liquefied components will pass, and then the vaporized components will pass.

5.4.2 Pulsation Frequency

This reading of the results predicts that a pulse will occur whenever enough liquid forms upstream of the MCC to form a slug. The volume of the slug would be a function of geometry and thus constant over different mixtures. The frequency of pulsation would then be given by:

$$f = \frac{\dot{n} X_l}{V \rho_l} \tag{5.2}$$

Looking at the data from the isothermal enthalpy test, the frequency of pulsations is plotted against the liquid fraction of each mixture, shown in Figure 5.12a. The quality is calculated by first removing the components due to liquid hold up at room temperature, and then calculating the molar liquid fraction of the remaining mixture at the pre-cooling temperature, and high-side pressure. The frequency is linear with molar liquid fraction, with different flow-rates having different slopes. In Figure 5.12b, the ratio of frequency and flow-rate is plotted against liquid fraction, and all of the data fall on the same line. The inverse of the slope gives the slugs to be 70 μmol, or 6.4 μL with a density of 11 mol/L.

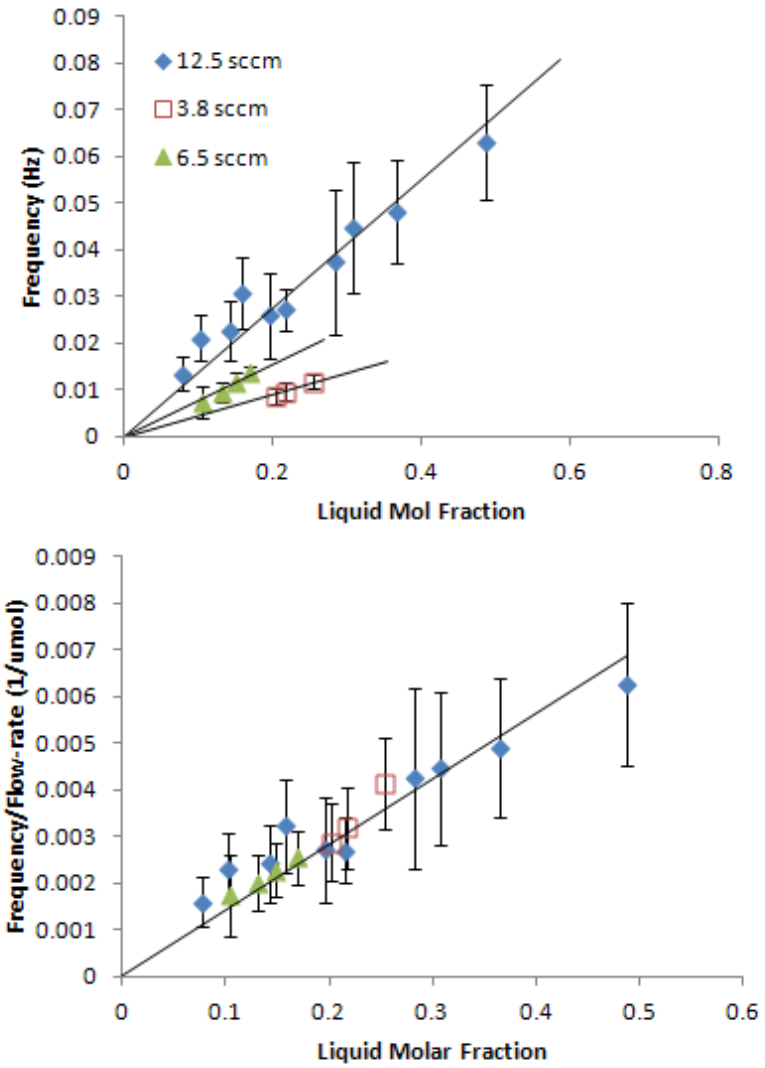

Figure 12: a) frequency of pulses as a function of liquid molar fraction for 3 different flow-rates, and b) the ratio of frequency and flow-rate as a function of liquid molar fraction.

5.4.3 Time to Pulses

This analysis describes pulses corresponding to slugs of liquid forming in the high-pressure pre-cooled lines, after a liquid film reaches a critical thickness. The time required to develop the first slug can be calculated knowing the film growth rate and the critical thickness. The critical thickness can be calculated from a critical vapor fraction (X_{crit}):

$$thk_{crit}/R = 1 - \frac{r_i}{R} = 1 - \sqrt{\frac{X_{crit}/\rho_v}{X_{crit}/\rho_v + (1-X_{crit})/\rho_l}} \tag{5.3}$$

where R is the channel radius, r_i the radius to the interface, ρ_v the vapor density and ρ_l the liquid density. Coleman and Garimella developed an empirical model for the transition between annular and slug flow in mini-channels as [68]

$$X_{crit} = a/(G+b)$$
$$a = 69.5673 + 22.595\, exp(0.2586 \cdot d_h) \tag{5.4}$$
$$b = -59.9899 + 176.8137 exp(0.3826 \cdot d_h)$$

where G is the mass flux in kg/m^{2}s, and d_h the channel hydraulic diameter in mm. This empirical model was developed for refrigerant R134a, but has been shown to predict the critical vapor fraction for other fluids as well, including water [69]. In 1/8" Cu tubing with a flow-rate of 30 sccm, the critical vapor fraction is 0.39, giving a critical thickness of 1.5% of the total channel radius. Based on this analysis, one can calculate the time required for liquid slugs to first appear as

$$t = \frac{\rho_l A}{\dot{n}(1-X)}\left(\frac{thk_{crit}}{R}\right) \tag{5.5}$$

where A is the surface area experiencing cooling, X the molar vapor quality of the fluid entering the pre-cooled channels, and thk_{crit} the critical film thickness from Equation 5.3. This is the analysis alluded to in Chapter 3.5.2, with results shown in Table 3.3. Note that the calculated times agree well for Mixtures 3 and 4, and show agreement to within a factor of 2 for Mixture 1, but are off by nearly an order of magnitude for Mixture 2. The difference between Mixture 2 and the other three mixtures is that Mixture 2 was designed to have no liquid in 0.4 MPa channels at ambient temperature, whereas the other 3 mixtures were designed to have up to 22 % of the

refrigerant liquefy in the high-pressure ambient temperature channels.

One assumption of this analysis is that the refrigerant at the suction port of the compressor has the original composition. This is not necessarily the case. Although the low-pressure lines are open to a large refrigerant reservoir, they are also open to the returning channel, which should have a different composition. This would result in the refrigerant at the suction port of the compressor having a lower concentration of the heavy components. As a result, less of the refrigerant fed into the high-pressure lines would condense along the walls, and the time required for the liquid film to reach its critical thickness would be longer.

5.4.4 Isothermal Enthalpy Difference Measurement

Such a flow regime would also change the isothermal enthalpy difference measured across a J-T valve. The overall cooling power of a single period of pulsation undergoing isothermal expansion is given by:

$$\dot{Q}_{gross} = \frac{1}{\tau_T}\left(\int_{\tau_v} \dot{Q}_v dt + \int_{\tau_l} \dot{Q}_l dt\right) = \frac{\tau_l}{\tau_T}\dot{n}_l \Delta h_l + \frac{\tau_v}{\tau_T}\dot{n}_v \Delta h_v \tag{5.6}$$

Here, τ_l τ_v and τ_T are the period of liquid flow, vapor flow, and total pulse period. The term Δh_l is the change in enthalpy of the components which are in liquid form in the high-pressure stream. Because the term $\frac{\tau_l}{\tau_T}\dot{n}_l$ will give the total flow-rate times the liquid fraction ($\dot{n}X_l$), and similarly $\frac{\tau_v}{\tau_T}\dot{n}_v$ gives the total flow-rate times the vapor fraction ($\dot{n}X_v$), Equation 5.6 gives a measured isothermal enthalpy difference of:

$$\frac{\dot{Q}}{\dot{n}} = X_l \Delta h_l + (1 - X_l)\Delta h_v \tag{5.7}$$

The authors term this the “pulse averaged” enthalpy difference, and it is calculated for the 3 mixtures measured, and plotted against the measured isothermal enthalpy differences in Figure 5.8, showing very good agreement. Such “pulse averaging” will necessarily result in a lower

cooling power than that of the overall mixture. This is because during the liquid pulse, some liquid will pass into the low-pressure side of the heat exchanger, and its evaporation will serve to cool the base of the MCC rather than the cold-end.

When the MCC experiences a temperature gradient, a similar analysis can be applied, by replacing the Δh terms with $(\Delta h|_T)_{min}$ terms. The end result is

$$\frac{\dot{Q}}{\dot{n}} = X_l(\Delta h_l|_T)_{min} + (1 - X_l)(\Delta h_v|_T)_{min} \tag{5.8}$$

This pulse averaged enthalpy difference is calculated for the 200K Mix, shown in Figure 5.13.

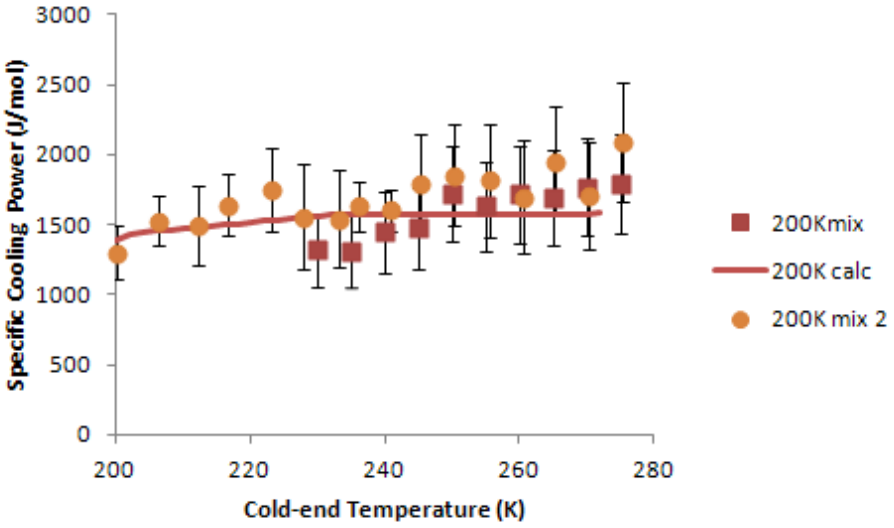

Figure 5.13: measured and calculated pulse-averaged specific cooling power for the 200K Mix, plotted as a function of cold-tip temperature, when the warm-end was pre-cooled to 273 K.

5.4.5 Modified Mixture

Refrigerant mixtures for MCCs operating in the pulsating flow regimes can be designed to increase the pulse-averaged enthalpy difference. This is demonstrated by adding isobutane to the 200K Mix. Two modified mixtures (Mix A and B) were mixed, with composition is listed in

Table 3. Unfortunately the isobutane used contained some helium contaminants, but Mix A and B still show enhanced performance. The isothermal enthalpy difference of these mixtures is measured and plotted in Figure 5.14a. The specific cooling power in the range of 205-275 K of Mix A is measured with 273 K pre-cooling, and plotted in Figure 5.14b. The solid lines in Figure 5.14a and b are calculated values, using the above calculation method.

	Mix A	Mix B
methane	5.60%	6.40%
ethane	32.20%	36.80%
propane	9.80%	11.20%
butane	2.80%	3.20%
pentane	19.60%	22.40%
iso-butane	26.70%	17.80%
helium	3.30%	2.20%

Table 5.2: Composition of 2 mixtures modified by adding an isobutane/helium mix to the 200K Mix.

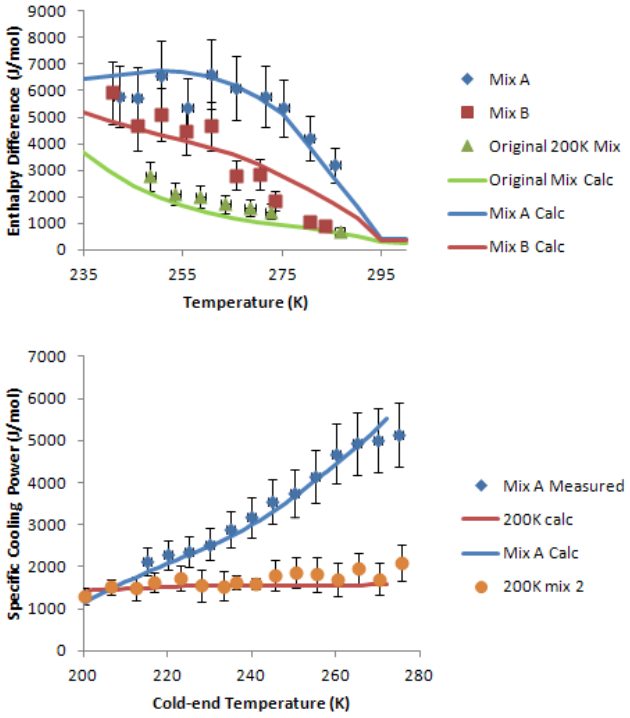

Figure 5.14: measured and calculated specific cooling powers of the original and modified 200K

Mix. a) Isothermal enthalpy difference of Mix A, Mix B, and the original 200K Mix. b) Specific cooling power of Mix A and the original 200K Mix as a function of cold-side temperature with the warm-end of the MCC pre-cooled to 273 K.

5.4.6 Pulsating flows in other MCCs

Pulsating flows of this nature will occur whenever non-azeotropic liquid slugs form in a mini-channel but are then transferred to a micro-channel heat exchanger. This will happen in mixed refrigerant MCC which uses mini-scale coupling channels for pre-cooling. Such flow pulsations have been observed in a second MCCs running mixed refrigerant, which used a polymer-based parallel-plate type heat exchanger shown in Figure 5.15. It is apparent that the geometry of the heat exchanger is not a factor in forming flow pulses, as the pulses form in the coupling lines upstream of the heat exchanger.

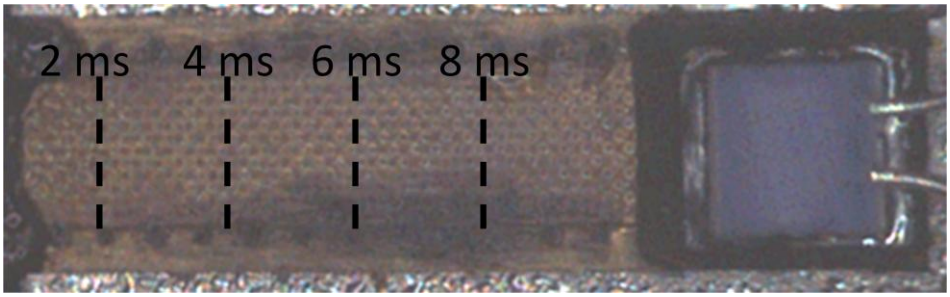

Figure 5.15: Location of the vapor-liquid interface in a polymer-based MCC during a liquid pulse, over 8 ms.

Were one to eliminate the pre-cooling lines, and instead perform pre-cooling on the micro-channels directly, such large liquid pulses would be eliminated. Some of the cooling power lost due to the temporal separation of the refrigerant may be recovered. However, micro liquid slugs may still form, and may result in some different micro-pulse cooling power. Studies of multi-phase microchannel flow have not been performed in the open literature on refrigerant mixtures undergoing phase change.

5.5 Conclusions

This article presents a study of mixed refrigerant in a micro cryogenic cooler undergoing a pulsating flow regime. The pulsating flow regime was visualized with high-speed video microscopy, the composition of the refrigerant mixture was measured with GC/TCD methods, and the isothermal enthalpy difference of multiple refrigerant mixtures was measured. The following conclusions can be drawn:

- Pulsating flows correspond to the buildup of a large slug of liquid upstream of the high pressure micro-channel CFHX. The slug of liquid has a larger volume than the CFHX high pressure channels, and fills them with liquid during a pulse. The MCC experiences all-vapor, all-liquid, and a brief 2-phase transitional flow.
- The overall composition of refrigerant passing through the MCC does not depend on the pre-cooling temperature, but the composition of the all-liquid- and all-vapor-phases of the refrigerant will depend on pre-cooling temperature.
- The average isothermal enthalpy difference of the refrigerant will be given by Equation 5.7, and the specific cooling power will be given by Equation 5.8.
- The composition of a refrigerant mix can be changed to improve the specific cooling power using these equations as guidelines.

CHAPTER 6: FABRICATION, ASSEMBLY, AND TESTING OF A MEMS-ENABLED MICRO GAS COMPRESSOR FOR A 4:1 PRESSURE RATIO

This study describes the fabrication, assembly, and testing of a micro gas compressor. The compressor is formed by MEMS-based check valves coupled to a Kapton membrane driven by a piezoelectric actuator. The valves are surface machined on a silicon substrate using polyimide as a structural material and copper as a sacrificial material. This design allows valves with low leakages, low compressor dead volume, and the high compressible volume required to generate the pressure levels required of numerous applications including cryogenic cooling. The assembled compressor is tested with voltages over the range of 25-180 V and frequencies over the range of 25-700 Hz. A maximum pressure ratio of 4.3:1 is found when the actuator provides a maximum displacement of 156 μm, and a maximum flow-rate through the compressor of 51 standard cubic cm per minute (sccm) is observed when the compressor is operating at its resonant frequency.

6.1 Introduction

Numerous micro systems benefit from micro gas compressors, including micro gas chromatography systems [70, 71], micro reactors with gas-phase reactants [72], micro fuel cells [73,74], and micro refrigeration [75]. Of particular interest are micro vapor-compression refrigeration systems which require compressors to increase the pressure of the refrigerant [76], as do Joule-Thomson cryogenic systems [1]. Several groups have demonstrated micro-scale heat exchangers and expansion valves, but have used considerably larger compression systems [47, 77-79]. There have been a number of studies investigating micropumps to compress a gas-phase fluid. Some of the more successful compressors operate with an actuated membrane and check valves [52,53,80]. Peristaltic pumps and valveless pumps have also been investigated for use as a

compressor [81, 82]. However, these pumps are unable to generate the pressures required for refrigeration and cryogenic systems. A maximum compression pressure ratio of 1.2:1 has been reported by Yoon et al [52], but a minimum pressure ratio of 4:1 is required for a number of mixed-refrigerant Joule-Thomson systems [12, 18].

Previous studies on micro compressors have generated low pressures due to a low ratio of swept volume to dead volume. In an isothermal system compressing a fixed mass of an ideal gas, the ratio of the final pressure to the initial pressure can be determined by the ideal gas law to be the ratio of the initial volume to the final volume: $P_f/P_i=V_i/V_f$. This final volume is considered "dead" volume. A well designed compressor will therefore have a minimized dead volume while maintaining a high swept volume.

The microcompressor used in this study is shown in Figure 6.1. It consists of a pair of check valves fabricated by MEMS processes, epoxy-bonded into a stainless steel valve substrate. A metalized Kapton membrane is pressed onto the substrate by a clamping fixture. Sealing between the membrane and substrate is facilitated by an o-ring placed in the substrate, such that it does not contribute significant dead volume upon sealing. The membrane is soldered to a copper "button" which connects to a mechanically amplified piezoelectric actuator. The actuator provides the high stroke length and force required to generate the required high pressures. Pressure ratios above 4:1 have been repeatedly demonstrated with this device. Pressures, flow-rates, and power-draw are measured as a function of actuator voltage and frequency. Further modifications to the assembly are suggested to improve the performance.

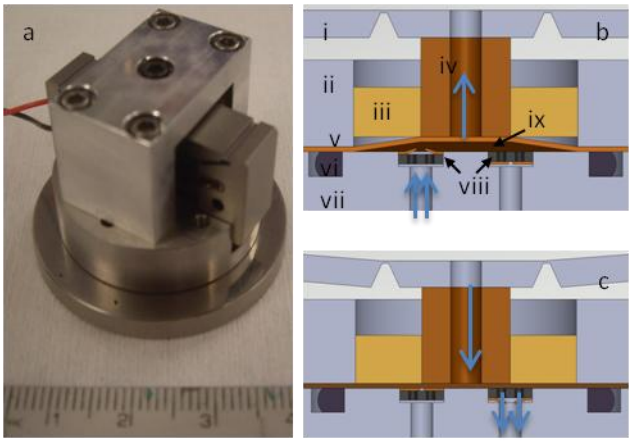

Figure 6.1: a) Photograph of the assembled micro compressor, with a cm-scale ruler for size comparison. b) cross-sectional schematic of the operation during an upstroke. The following parts are noted: i) amplified PZT actuator frame, ii) clamping fixture, iii) brass backing, iv) copper "button," v) copper-coated Kapton membrane, vi) O-ring, vii) valve substrate, viii) MEMS valves, and ix) compressible volume. c) cross-sectional schematic during a down-stroke operation. Note the dead-volume is minimized.

6.2 Fabrication and Assembly

6.2.1 Design parameters

In order to aid the design of the system, the pressure ratio as a function of flow-rate was modeled by applying conservation of mass and energy to a compressible volume, and assuming that the system is isentropic. Under such a formulation, the pressure can be expressed as [83]:

$$\frac{dP}{dt} = \frac{kP}{\rho V}(\dot{n}_{in} - \dot{n}_{out}) - \frac{kP}{V}\frac{dV}{dt} \tag{6.1}$$

Here, *P, k, V, ρ, t,* and $\dot{n}$ are the pressure, specific heat ratio, volume, molar density, time, and molar flow-rate, respectively. The flow through the valves in one direction is assumed to be linear with pressure drop across them, with a certain cracking pressure required for any flow: $\dot{n} = \alpha(P_{in} - P_{out} - P_{crack})$. Here α is a proportionality constant, taken to be a parameter of the valves. For a given α, Equation 1 can be numerically integrated to find the pressure variation in the compressible volume, and the subsequent net flow-rate. Figure 6.2 shows the pressure vs.

flow-rate curves for various conditions of valve leak rate, actuation stroke length, valve cracking pressure, and dead volume. As can be seen in Figure 6.2a, valves with a backflow leak rate of up to 1 sccm/bar are acceptable. Valves which do not exhibit cracking pressure are also favorable.

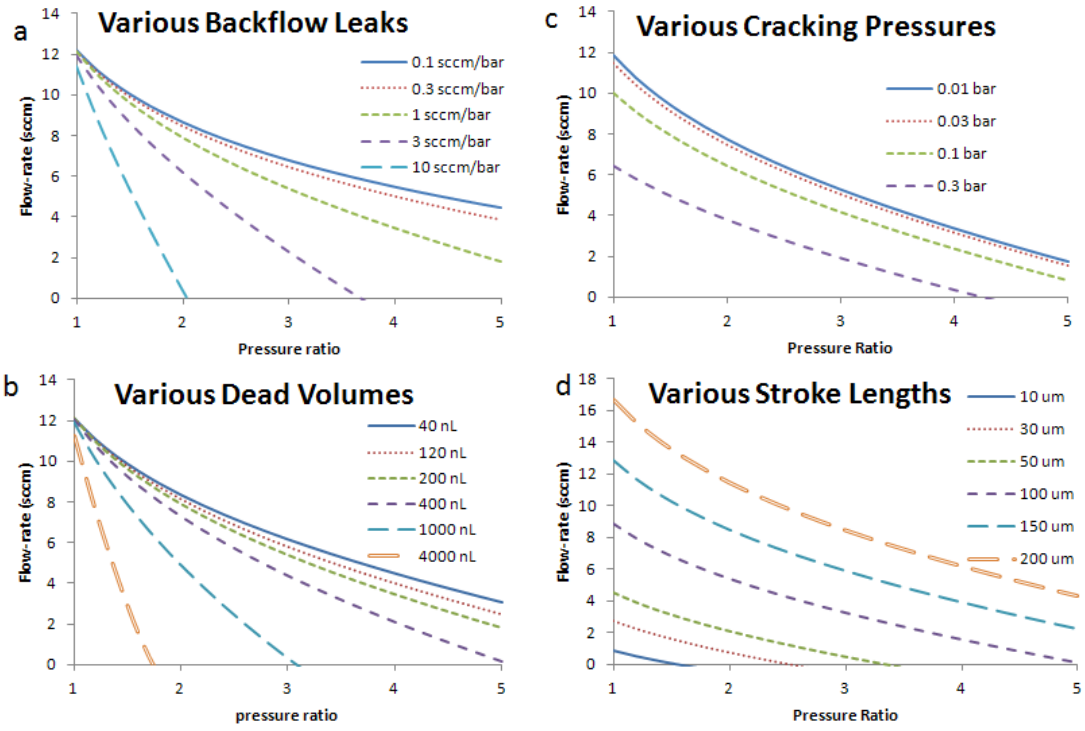

Figure 6.2: Modeled curves for pressure ratio vs flow-rate, under different conditions of valve back-flow rate, stroke length, cracking pressure, and dead volume. Unless otherwise stated, the backflow leak used in the model is 1 sccm/bar, stroke length is 150 µm, cracking pressure is 0, and dead volume is 200 nL.

6.2.2 Valve fabrication

The design of the check valves received considerable attention. The valves are surface micromachined rather than bulk micromachined to reduce the valve dead volume. A number of micro valves have been developed previously, including ones which require a cracking pressure in order to allow flow [84], and ones which require some pressure in order to close [53, 85]. For our application, the best valves do not require any cracking pressure to operate, but some

backflow leak is tolerable.

The valves developed here are made of polyimide. The flexures are not pre-stressed, which eliminates cracking pressure. The sealing surface of the valves is formed in a cavity, which allows a large area for sealing. The annular gap is controlled by a sacrificial layer, which can be made very small, thus requiring a very small pressure difference across the valve to seal. The design schematic of the valve is shown in Figure 6.3.

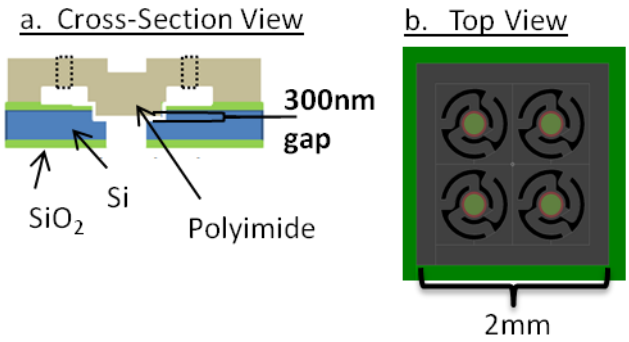

Figure 6.3: a) Cross-sectional schematic of an individual valve, and b) top view of a CAD-generated valve array.

The process flow for these valves is shown schematically in Figure 6.4. It consists of:

- growing and patterning a SiO_2 layer on a Si wafer,
- reactive ion etching (RIE) process to define the valve cavity,
- sputtering and patterning a 300 nm layer of copper to define the annular gap of the valve,
- evaporating a 2 µm layer of copper patterned with a lift-off technique in order to define valve flexure area,
- spin-coating a 10 µm polyimide layer as the valve structural material,
- patterning it with RIE to define the valve flexure geometry, and

- a deep RIE (DRIE) process on the backside of the wafer to form the through-hole to the valve.

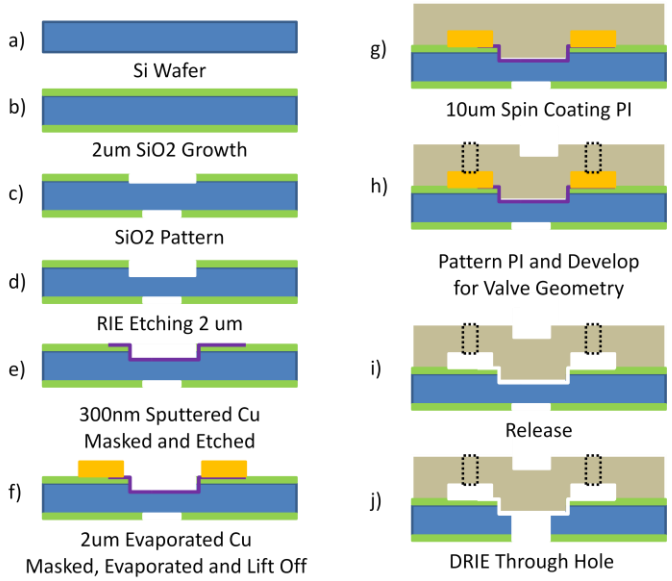

Figure 6.4: Process flow for the fabrication of a valve.

A single valve die which measures 2 mm x 2 mm contains a 2 x 2 array of 4 micro-valves, acting in parallel. This array ensures that if a single micro-valve is sealed, the valve die will still function. Further, if some particulates get behind the 300 nm gap between the polyimide and silicon sealing area, forcing the valve open, the through-hole to that valve can be sealed with epoxy, and the valve array will still be functional. A completed valve die is shown in Figure 6.5.

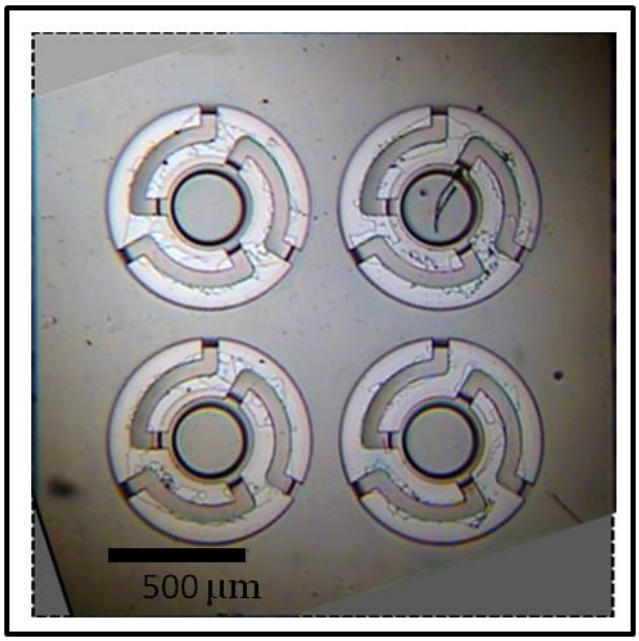

Figure 6.5: Photograph of a valve die showing a 2 x 2 valve array. (Note that the original photograph was rotated in the frame such that it did not include the top-left, bottom-left, or bottom-right corners. Extrapolations of these 3 corners are shown with dashed lines and a solid grey color). Each valve utilizes 3 rounded flexure arms. The silicon substrate appears as a lighter color than the darker polyimide.

6.2.3 Assembly

The complete micro compressor consists of a valve substrate, membrane assembly, actuator, and mounting bracket shown in Figure 6.6. The valve substrate is composed of two valve array dies, which are epoxy-bonded onto a stainless steel substrate. One of the valve arrays is prepared with a capping chip. The capping chip provides a 10 μm cavity for the valve to open into, and through-hole to allow the gas passage. In addition, it provides protection for the valves during a subsequent polishing process used to flatten the valves against the substrate, thereby reducing dead volume.

Two 2.1 x 2.1 mm cavities are milled into the steel substrate, one to a depth of 0.35 mm, and one to 0.75 mm. The inlet valve is bonded with the capping chip facing upward, and the outlet valve die is bonded with the valves facing downward. Epoxy fills the 50 μm wide gaps on

the sides of each valve die. In both cases, the surface of the silicon will be ~50 μm above the steel surface, and polishing is required for a smooth final surface. Because polishing produces particulates which can ruin the valves, the valve through-holes are filled with an acetone soluble wax for the polishing process, which is removed afterward. This process is shown in Figure 6.7. The backflow leak characteristics of the valves are checked after the final polishing, and any valves with a high backflow leak are filled with epoxy.

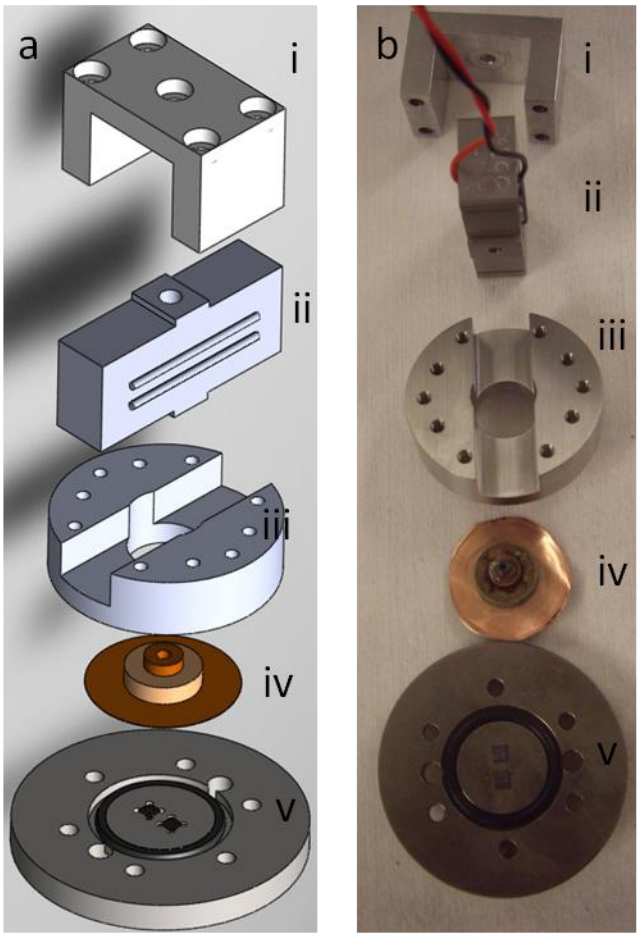

Figure 6.6:a) CAD image and b) Photograph of the micro compressor components. These are from top to bottom: i) mounting bracket, ii) actuator, iii) clamping fixture, iv) membrane assembly (copper button, brass backing and Cu-Kapton membrane), and v) valve substrate assembly.

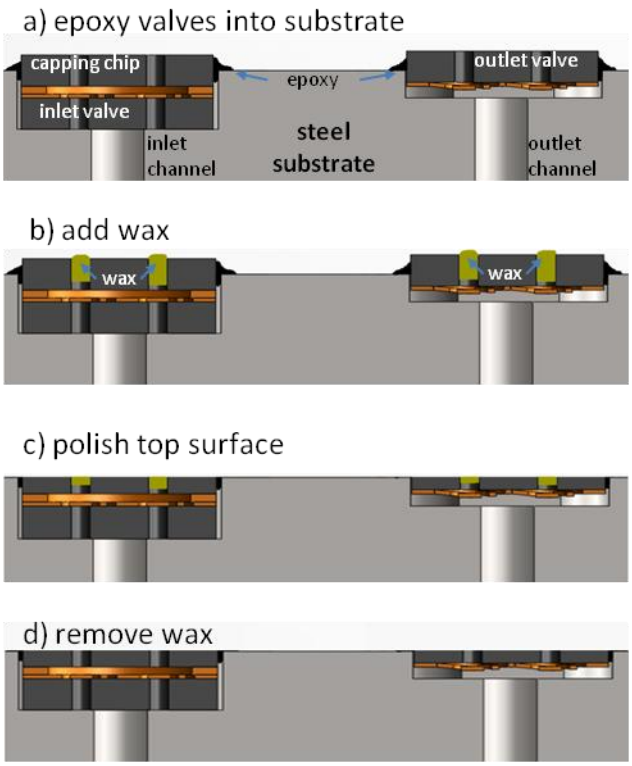

Figure 6.7: Assembly of the MEMS valves into the valve substrate:

The membrane is 50 μm thick Kapton, metalized with copper on both sides, cut to a diameter of 17 mm. The copper was removed with a copper etchant from one side to allow a softer mating surface with the steel. Kapton was chosen for its superior tensile strength, which allows the membrane to stretch and contract under actuation without damaging the membrane. The copper side of the membrane is solder-bonded to a copper "button" which connects it to the actuator. We found a solder bond to be strong enough to survive the stress associated with deforming the membrane over 10^6 cycles. A brass backing piece is placed around the copper "button" to prevent the membrane from bulging upward when there is a high pressure differential across it, since such bulges would constitute a dead volume. The compression area is bounded by the valve substrate on the bottom and membrane on the top. A membrane compression fixture (Figure 6.6a.iii) is bolted onto the substrate, with the membrane between it and the substrate. A 10 mm hole in the center of the fixture defines the maximum width of the compressible area. An

o-ring, with an inner diameter of 14 mm ensures that the compression area is sealed.

The actuator used in this test is a FPA-0200E-S-0518 flex-frame actuator from Dynamic Structures and Materials. It has a nominal (unloaded) stroke of 200 μm, and a maximum (no-stroke) force of 96 N. When the actuator is actuating against a load, the stroke decreases linearly with load, until at 96 N, there is no stroke. A 4.3:1 pressure ratio, with low pressure of 0.081 MPa against a membrane 1 cm in diameter yields a force of 20.7 N, corresponding to a maximum stroke of 156 μm. This actuator has #2-56 bolt taps in the top and bottom. The actuator is attached to the copper button via a set-screw, and a mounting bracket (Figure 6.6a.i) connects the top of the actuator to the clamping fixture. A small o-ring is placed between the mounting bracket and the actuator—in this way, the height offset of the membrane against valve substrate is controllable: tightening the top bolt lifts the actuator and membrane away, and when the top bolt is loosened, the o-ring forces the actuator and membrane down toward the valve substrate. The precision of such an approach is roughly 5 μm.

6.3 Testing, Results and discussion

The assembled compressor was tested for flow-rate under conditions of zero pressure buildup, and for pressure under conditions of zero flow. The working fluid was ambient air, at a pressure of 0.81 bar. The flow-rate into the suction port of the compressor is measured with a mass flow-meter, and the pressure at the discharge port is measured with a pressure transducer. A sinusoidal waveform is produced by a function generator, and amplified by a nominal value of 100x using an amplifier designed for piezoelectric actuators (Trek PZD 350), which can provide a peak current of 200 mA. Voltage and current drawn by the amplifier are monitored to determine the AC power draw by the compressor. These actuators are made for a maximum applied voltage of 150 V, and a minimum of -30 V. The maximum frequency with which they can be run is limited

by the current of the amplifier, which in turn depends on the driving voltage. For our actuator system at its maximum 180 V_{pp}, the maximum frequency achievable was 75 Hz. Lower voltages allowed higher frequencies.

With a signal voltage of 0.25 V_{pp} provided by the function generator, the flow-rate (for a pressure ratio of 1) and pressure ratio (for a flow-rate of 0) are plotted in Figure 6.8a as a function of frequency from 25 to 700 Hz. This voltage is chosen because it is the maximum actuation voltage that can be sustained by the amplifier at 700 Hz. Note that the flow-rate increases linearly with frequency until the system approaches its resonant frequency of 700 Hz. The linear relation between frequency and flow-rate at the lower frequencies is to be expected, as the flow-rate with a pressure ratio of 1 is given by the product of the volume displaced per stroke and the stroke frequency. The further increase in flow-rate near the resonant frequency is due to extra stroke length achieved by resonant operation and non-linear amplification. For frequencies above 300 Hz, the amplifier provides a gain above 100. The gain is shown as a function of frequency in Figure 6.9 a. At 700 Hz, although the signal provided by the function generator remains 0.25 V_{pp}, the voltage provided by the amplifier to the actuator is 42 V_{pp}. This indicates that the actuation length has nearly doubled, and the volume displaced per stroke nearly doubled with it.

Notice also from Figure 6.8a that the pressure ratio is only weakly dependent on frequency, until near the resonant peak. With no flow-rate, the pressure ratio of an ideal gas compressor will be given by the ratio of the swept volume to the dead volume—which is a function of geometry and independent of frequency. In a real compressor, some volume of gas will escape through valve leaks, and this may be thought of as dead volume as well. Such volume is the leak rate integrated over the leak time; thus with increasing frequency, there is less

leak time per stroke, the dead volume from valve leaks decreases, and the pressure ratio increases. When the system is in resonance, the increased stroke length will increase the swept volume, thus increasing the pressure ratio.

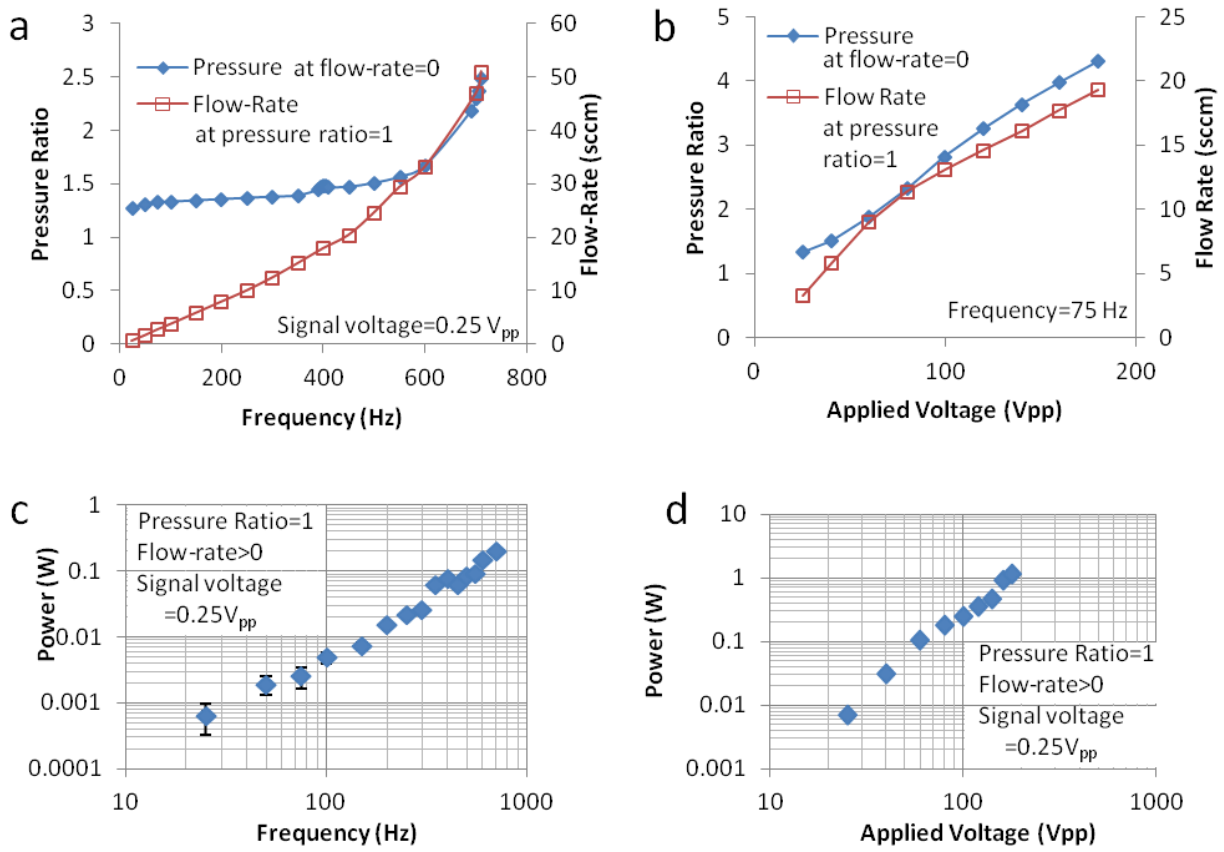

Figure 6.8: Pressure ratio (with zero flow) and flow-rate (with a pressure ratio of 1) as a function of a) frequency and b) applied voltage. The power drawn by the compressor is also shown as a function of c) frequency and d) applied voltage. The power-draw measurements were performed with a pressure ratio of 1.

Figure 6.8b shows pressure and flow-rate at a frequency of 75 Hz as the voltage is varied. This frequency is chosen as it is the maximum that can be sustained by the amplifier at a voltage of -30 to 150 V. Both the pressure and flow rate increase with increasing applied voltage, as one would expect when the swept volume increases. A maximum pressure ratio of 4.3:1 is reached at 180 V_{pp}. This is high enough to drive Joule-Thomson cryogenic cooling processes [12].

Real power drawn in an AC system is given by the integral average of the product of the voltage with the current, averaged over a period of oscillation:

$$P = \frac{f}{2\pi}\int_0^{2\pi/f} I(t)V(t)dt, \tag{6.2}$$

with *f* frequency, *V(t)* voltage and *I(t)* current. When the voltage and current are sinusoidal, with a phase angle separation of θ, this reduces to: $P = I_{RMS}V_{RMS}\cos\theta$, where RMS denotes the root-mean-squared value. However with this actuator at a frequency above 300 Hz, the waveforms will be distorted as in Figure 6.9b, requiring numerical integration of Equation (6.2). The resulting power draw data are all plotted as a function of frequency in Figure 6.8c, and voltage in Figure 6.8d. Note that the slope on a log-log plot of power vs. frequency is roughly 1 for *f<300* Hz, and roughly 2 for *f>300* Hz. The impedance of a capacitor is proportional to frequency, so when the voltage has constant amplitude the power is expected to be linear with frequency. Above 300 Hz, the amplitude of the voltage will increase with frequency as well, due to resonant pumping, resulting in a quadratic dependence of power on frequency. The log-log slope of power vs. applied voltage is roughly 2, showing that power is quadratic with applied voltage.

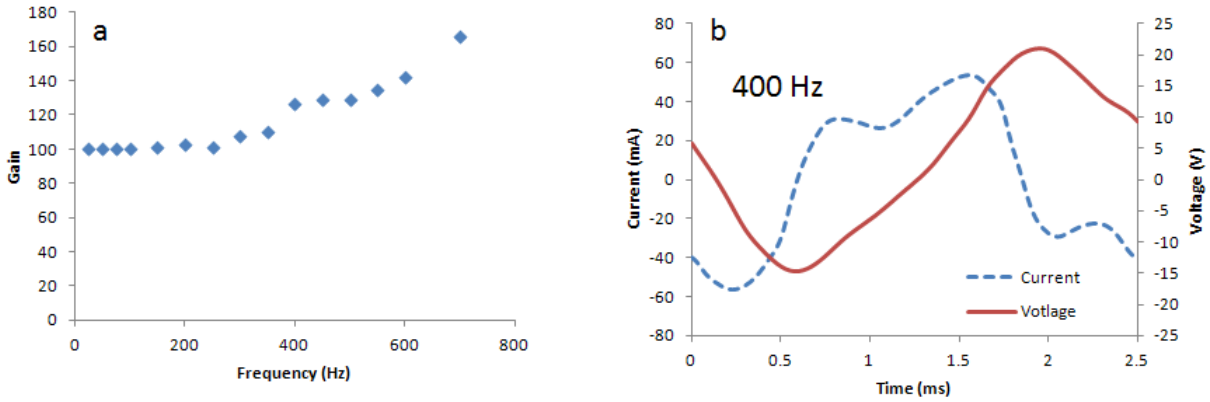

Figure 6.9: a) gain of the amplifier as a function of frequency. Note that it is a linear amplifier up to 300 Hz, and the gain increases from there. b) Voltage and current waveform drawn by the PZT actuator from the amplifier for 400 Hz, showing non-linear distortions.

Powers drawn for this compressor range from less than 1 mW to more than 1 W, which is comparable to miniature compressors used for small-scale refrigeration [12].

6.4 Conclusion

This paper discusses the fabrication, assembly and testing of a MEMS enabled micro compressor. The compressor operates by compressing gas between an actuated membrane and MEMS check valves. The check valves are surface micromachined on a silicon substrate, using copper as a sacrificial material and polyimide as the structural material. Such valves provide excellent sealing with no cracking pressure. Valve dies are epoxy-bonded to a stainless steel substrate, which is pressed against a metalized Kapton membrane driven by a piezoelectric actuator. The actuator provides the necessary force and stroke to generate pressure ratios above 4:1. Such pressure ratios are high enough to drive vapor-compression and Joule-Thomson refrigeration systems.

The highest flow-rates are seen when the system operates at its resonant frequency; there is also a boost in pressure at resonance. Under the conditions tested, the highest pressure occurs with the highest actuator stroke. At such a driving voltage, the frequency is limited due to current limits in the piezo-amplifier used here. Use of an amplifier designed to drive this piezo actuator at its full stroke and resonance frequency is expected to improve performance substantially, but is also expected to consume considerably more power.

CHAPTER 7: SUMMARY, CONCLUSIONS, AND FUTURE WORK

This chapter summarizes the major points of the dissertation: review of mixed refrigerant Joule Thomson (MRJT) thermodynamics, development of a miniature compressor and low-pressure refrigerant tests, analysis of steady flow in terms of liquid hold-up, analysis of pulsing flow in terms of mini-channel liquid slugs, and the development of a MEMS-enabled micro/mini compressor. The model of pulsing flow is used to understand the results of high-pressure mixture testing performed previously, and used to design mixtures to cool to 160 K and 200 K with higher cooling powers. Finally, future work is proposed, including detailed understanding of non-pre-cooled pulsing flow, thermoelectric pre-cooling of micro-channels, experiments to understand heat and mass transfer of refrigerant mixtures in micro-channels, and the development of a vapor-compression cascade cooler.

7.1: Summary

Figure 1.6 provides an at-a-glance summary of the most important contributions of this dissertation: the understanding of steady and pulsating flows. It is reproduced here as Figure 7.1.

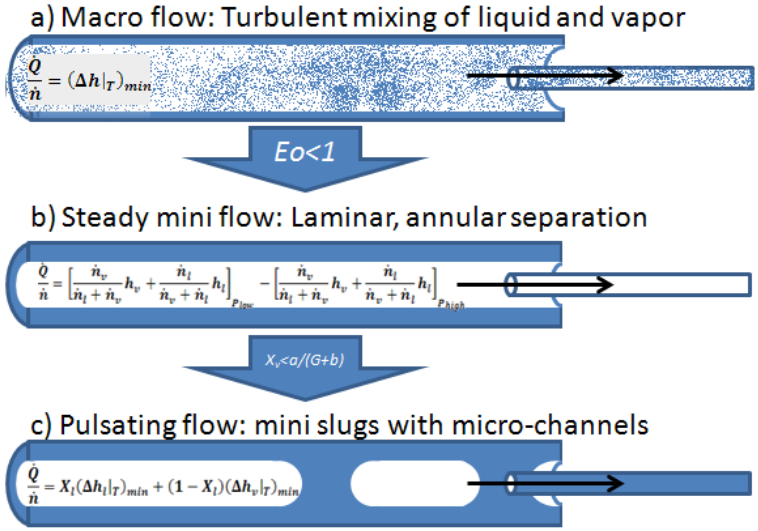

Figure 7.1: a reproduction of Figure 1.6, a schematic of 3 different flow regimes encountered

with mixed refrigerant cryogenic coolers, and expressions for their corresponding specific cooling powers. a) Macro-scale flow in which turbulent mixing ensures an even distribution of refrigerant composition. A thorough review of refrigerant mix design for this situation was given in Chapter 2. b) Steady, laminar mini-channel occurs when the Bond number is less than 1. In this flow regime, an annular separation between the liquid and vapor phases causes the cooling power to be given by a "cup-mixing" average. This was discussed in Chapter 4. c) Pulsating flow occurs when the mini-channel vapor fraction is less than a critical value. Here slugs of liquid form in mini-channels and have a larger volume than the downstream micro-channels. This allows a complex 2-phase flow phenomenon to be treated as 2 sequential 1-phase flows, as was discussed in Chapter 5.

A detailed summary of the first 6 chapters of this dissertation can be summarized as follows:

Chapter 1 listed the motivation of mixed refrigerant Joule-Thomson (MRJT) micro cryogenic coolers (MCCs) by highlighting the applications which would benefit from micro cooling technology, and showing how MRJT MCCs can be 10 times smaller than Stirling coolers, while 10 times more efficient than thermoelectric coolers. MRJT MCCs can experience micro- and mini-channel flow, as opposed to macro-scale flow. After reviewing previous work at CU on MRJT micro cooling that demonstrated steady but medium-temperature and unsteady but low-temperature performance using a large-scale compressor with a 16:1 pressure ratio, the following goals were presented:

- Develop a miniature compressor with a >4:1 compression ratio and demonstrate low-temperature cooling with a new low-pressure refrigerant mixture.
- Understand steady flow, including a model of refrigerant cooling power.
- Understand pulsating flow, including developing a model of refrigerant cooling power.

The understanding of the steady and pulsating flow is summarized in Figure 1.6, which is reproduced as Figure 7.1.

Chapter 2 reviewed the history and theory of MRJT cooling, including heat exchanger design optimization, and refrigerant mixture design optimization. Implicit in that design process

was the assumption that the liquid and vapor components of the refrigerant move with the same flow-rate, such as encountered in large-scale systems. Chapter 2 also gave a review of previous JT MCC development. All of the previously developed MCCs have used either a large high-pressure refrigerant supply bottle or a larger compressor to drive them, in contrast to our work with a miniature compressor.

Chapter 3 showed the major steps involved in fabrication and assembly of a fiber-based MCC. The fabrication was identical to that of Lin [16], but the assembly method was changed to replace solder coupling with epoxy, which allows simpler assembly while being robust at the low pressures experienced in this dissertation. Furthermore, a miniature compressor was developed in Chapter 3 by coupling a commercial piston oscillator to micro-machined check valves. The compressor showed a maximum compression ratio of 7.6:1 and a maximum flow-rate of 503 sccm with Nitrogen. Four refrigerant mixtures were designed for operation with a high pressure of 0.4 MPa and a low pressure of 0.1 MPa, over different temperature ranges, and each was tested with the miniature compressor and fiber-based MCC. Each mix exhibited steady flow with no pre-cooling, and with pre-cooling each mix exhibited a period of steady flow followed by a period of unsteady flow. In some cases the unsteady flow corresponded with enhanced cooling. Mix 1 (“200K Mix”) reached the designed low temperature, such that this chapter met the first dissertation goal.

Chapter 4 covered an analysis of the steady flow regime, showing that steady flow corresponds to complete hold-up of the liquid portion of the mixture in the high-pressure coupling lines. This was verified by measuring the isothermal enthalpy difference of the refrigerant mixture in the MCC during steady flow, and by sampling the mixture during steady flow. A charging time model was presented which describes the long period of time required for

the high pressure to develop. Such an understanding of steady flow meets the second dissertation goal.

Chapter 5 covered an analysis of the pulsing flow regime, showing that pulsing flow corresponds to slugs forming in the mini-channels of the high-pressure side, and filling the micro-channels of the MCC. This model of pulses was developed based on visual analysis of liquid flow in the MCC. The isothermal enthalpy difference during pulsing flow was measured following the methodology of Chapter 4, and the specific cooling power of the refrigerant in an MCC with a temperature gradient was measured as well. With pulsing flow, the cooling power of a refrigerant mixture can be calculated as:

$$\frac{\dot{Q}}{\dot{n}} = X_l(\Delta h_l|_T)_{min} + (1 - X_l)(\Delta h_v|_T)_{min} \tag{5.8}$$

where X_l is the liquid fraction of the circulating mixture at the high pressure and pre-cooling temperature—the circulating mixture will be the original mix enriched in lighter components with room-temperature liquid hold-up; $(\Delta h_l|_T)_{min}$ is the isothermal enthalpy difference between the high-pressure liquid components and the low-pressure mix of the same composition, minimized over the temperature range in question; and $(\Delta h_v|_T)_{min}$ is isothermal enthalpy difference of the vapor-phase components between high- and low-pressure. This equation meets the third dissertation goal.

Chapter 6 describes the development of a MEMS-enabled PZT driven micro gas compressor. Such a compressor uses MEMS-based polyimide check valves which show superior sealing and opening performance to the micro machined valves used in the rotary-based compressor. The compressor uses an amplified piezoelectric stack actuator to drive a piston 150 μm with a force of 20 N, to reach a pressure ratio of 4:1. A maximum flow-rate of 52 sccm was seen when the actuator oscillated at 750 Hz—this is a higher frequency than a Stirling system

can operate, and demonstrates the potential to miniaturize MRJT coolers beyond what is possible with Stirlings.

7.2: Conclusions

7.2.1: Analysis of High-pressure mixtures from Ref [16].

This understanding of pulsating flow can be applied to the results of Lin [16] with higher-pressure mixtures and the same fiber-based MCC. In the test set-up employed in [16], refrigerant was compressed at a large compressor, passed through several meters of refrigerant line, then passed through several cm of 1/8" copper tubing that was thermally anchored to a pre-cooled plate, pre-cooled to 240 K. Under such a situation, liquid slugs would have developed in the pre-cooled lines as well. First consider the 3-component mixture designed for operation at 16:1 to cool to 140 K. The mix was composed of 62 % methane, 14 % ethane, and 22 % propane. When operating with a high pressure of 1.4 MPa and low pressure of 0.08 MPa, no liquid would form (and be held-up) in the room-temperature lines. Because the mix is very simple, the liquid composition is close to the vapor composition, and the pulsing isothermal enthalpy difference plot is very similar to the non-pulsing plot, shown in Figure 7.1. In both cases, the cooling power goes to zero near 112 K, but is above 2000 J/mol at 115 K.

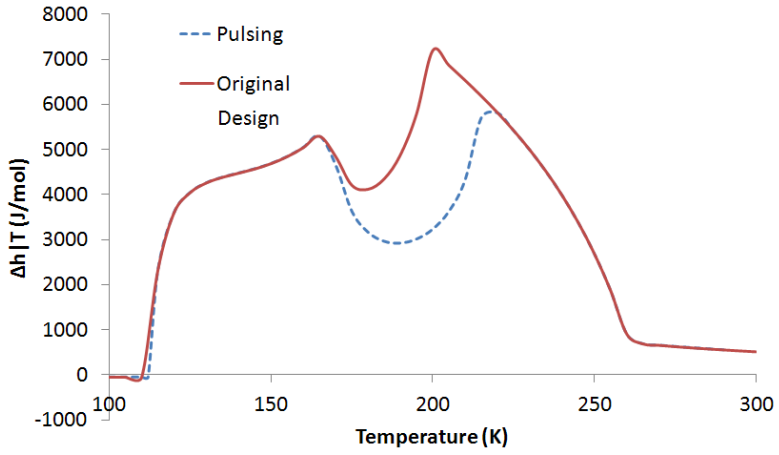

Figure 7.2: Plot of pulsing and non-pulsing isothermal enthalpy difference of the 3-component

mix.

The other mixture studied by Lin in [16] was composed of 6% Neon, 42% Nitrogen, 22% Methane, 16% Ethane, and 14% Propane. The presence of Nitrogen and Propane in that mixture would cause the existence of a 3-phase vapor-liquid-liquid (VLL) equilibrium, for with the pulsing flow model of Chapter 5 is ill-equipped to handle. The dynamics of 3-phase VLL flow in mini-channels and micro-channels has not been investigated in the open literature, and is likely the cause of such erratic cooling behavior, as shown in Figure 7.2. The Nitrogen-heavy liquid phase would give effective cooling in temperatures below 100 K, whereas the Propane-heavy liquid phase would give effective cooling in temperatures above 140 K. If a slug of the Propane-heavy liquid phase entered the MCC while it was below 100 K, the liquid would have a higher specific heat than the exiting nitrogen, and the heat exchanger would not effectively pre-cool the propane. The result would be a temperature jump, like the ones in Figure 7.2. Further understanding of VLL flow is required to properly understand the details of cooling with mixed refrigerants in micro coolers employing VLL.

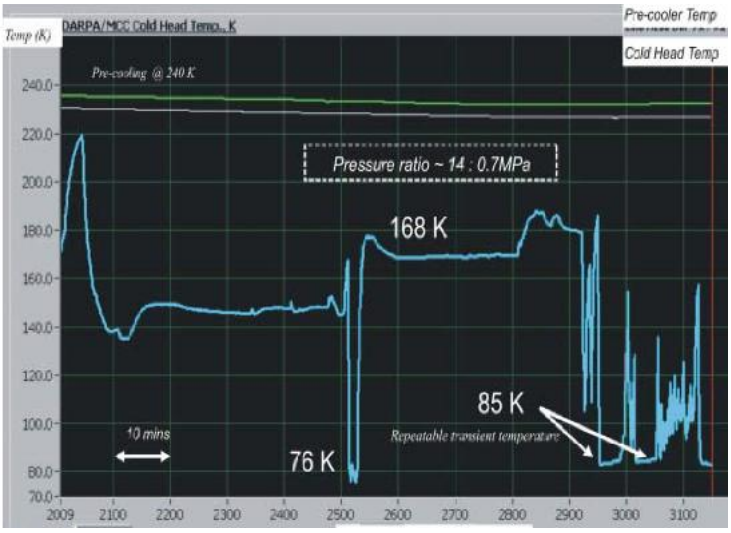

Figure 7.3: Rapid oscillations in temperature experienced by the MCC operating with a 5-component VLL mixture. Reproduced from [86].

7.2.2 Designing low-pressure refrigerant mixtures.

Equation 5.8 can be used to design refrigerant mixtures with higher specific cooling powers over the temperature range of interest. For example, to cool to 160 K, the original 160K Mix has a specific cooling power of 237 J/mol at the low temperature when expanding from 0.4 MPa to 0.1 MPa. This is not enough to overcome the background heats, and the operation with the 160K Mix could only cool to 220 K. Furthermore, the change in Gibbs energy of this mix at the compressor is 3310 J/mol, giving an ideal J-T COP of 8.36 % (see Equation 3.6). Adjusting the composition to 15.1% methane, 20.7 % ethane, 13.2 % ethylene, 34 % isobutane, and 17 % isopentane can increase that specific cooling power to 459 J/mol, shown in Figure 7.3. This is still quite low, but increasing the high-side pressure to 0.75 MPa while maintaining the 4:1 pressure ratio, and lowering the pre-cooling temperature to 260 K allows a re-designed mixture to increases the cooling power at 160 K to 831 J/mol—which is higher than the cooling power of the original 160K Mix at its lowest demonstrated temperature of 220 K. This re-designed "7.5:1.75" re-designed mix has an optimized composition of 22% methane, 12.2. % ethane, 17.1 % ethylene, 39 % isobutane, and 9.8 % isopentane, and has an ideal JT COP of 32.8 %. Of course, when operating with a high-pressure of 0.75 MPa with a low pressure of 0.1 MPa, the cooling power can be increased further, in this case to 1200 J/mol, but the COP remains at 32 %.

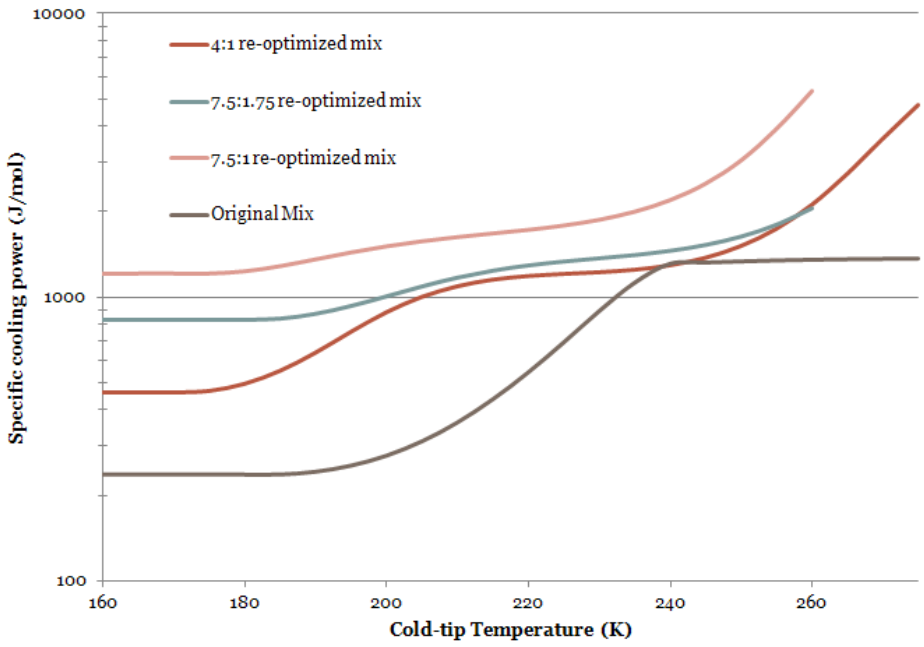

Figure 7.4: re-designed mixtures to cool to 160 K. Cooling with a pressure ratio of 7.5:1.75 and pre-cooling to 260 K greatly enhance the cooling capability.

The mix for increased cooling power to cool to 200 K can be found by introducing iso-butane. With a mixture composed of 2% methane, 42% ethane, 10% propane, 3% butane, 14% pentane, and 29% isobutane, the specific cooling power at 200 K increases from 1382 J/mol to 1674 J/mol. Higher gains in specific cooling power are made at the warmer temperatures, which serve to speed up the cool-down time.

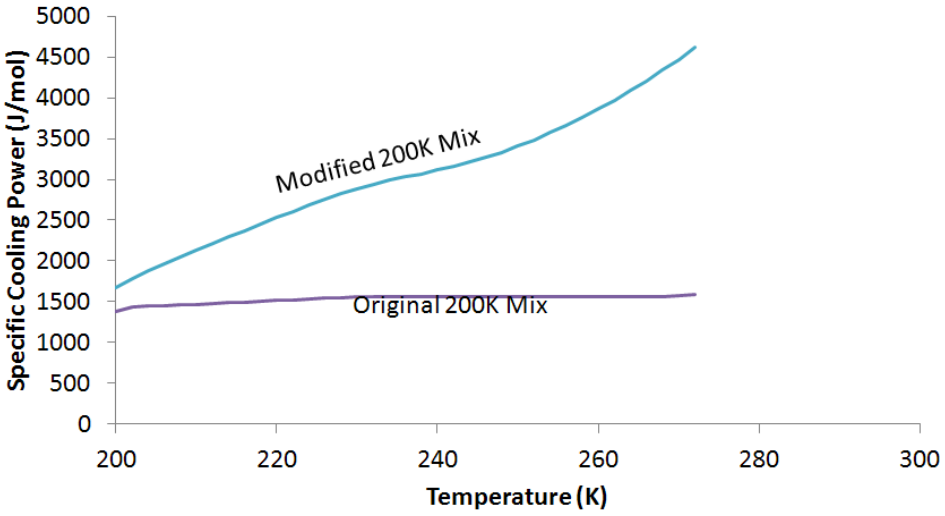

Figure 7.5: re-designed mixture to cool to 200 K.

7.3: Future Work

7.3.1: Non-pre cooled pulsations

Equation 5.1 calculated the maximum liquid fraction in the high-pressure non-pre-cooled lines after all of the liquefiable components in the low-pressure lines were deposited in the high-pressure liquid film. If that value were higher than the critical liquid fraction, then slugs of liquid would form in those lines and pulsing flow could occur without pre-cooling. This can be achieved by increasing the liquid fraction of the mixture, or increasing the total number of moles in circulation without increasing the volume of the high-pressure side. Indeed, pulsations without pre-cooling have been observed for the 200K Mix.

The refrigerant mixture was charged into the compressor at a suction pressure of 0.134 MPa, with a high-pressure of 0.60 MPa. After running, Valve 1 was closed, and the system allowed to equalize to a pressure of 0.219 MPa. Several hours later, the refrigerant was compressed, with pressure, flow-rate, and temperature shown in Figure 7.5.

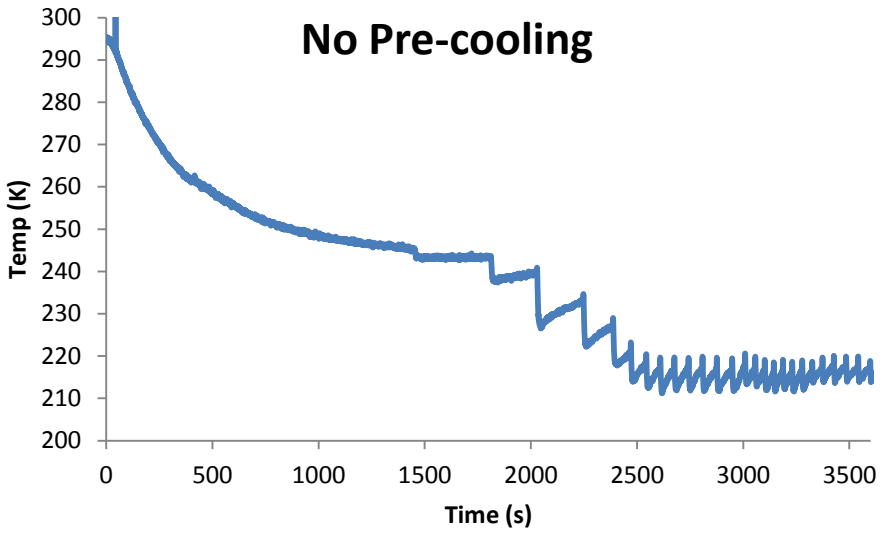

Figure 7.6: Cool-down curve of MCC without pre-cooling showing the development of pulses after 1500 s.

The flow-rate was roughly 40 during the pulsating flow. Compared to the same MCC undergoing pulsing flow with pre-cooling, the frequency is quite low, as would be expected with a lower liquid fraction. Still, further work is required to verify the circulating refrigerant composition and find the associated cooling power of pulsating flow developed without pre-cooling.

7.3.2: Integrated Thermoelectric Pre-cooling

In the context of this dissertation, pulsating flow is due to slugs of liquid that form in high-pressure miniature channels, and then pass into high-pressure micro-channels. When the MCC experiences steady flow, liquid is either not present in the coupling channels or is being held-up in them, and does not enter the high-pressure micro-channels of the heat exchanger. Liquid can still form in the micro-channels of the heat exchanger, but because the channels are fed with vapor-phase refrigerant, the cooling power is still low. If liquid were to form in the micro-channels upstream of the heat exchanger the cooling power could increase considerably.

This can be achieved with integrated thermoelectric (TE) pre-cooling of the CFHX. In

practice, this can be as simple as gluing a TE cooler to the CFHX using a thermally conducting epoxy, as shown in Figure 7.6. This set-up enabled temperatures as low as 180 K when running the 200K Mix. The TE pre-cooler can develop pre-cooling temperatures as low as 257K, when a power of 156 mW is applied. Lower TE driving powers lead to higher pre-cooling temperatures. The flow-rate through this device was between 10 and 20 sccm.

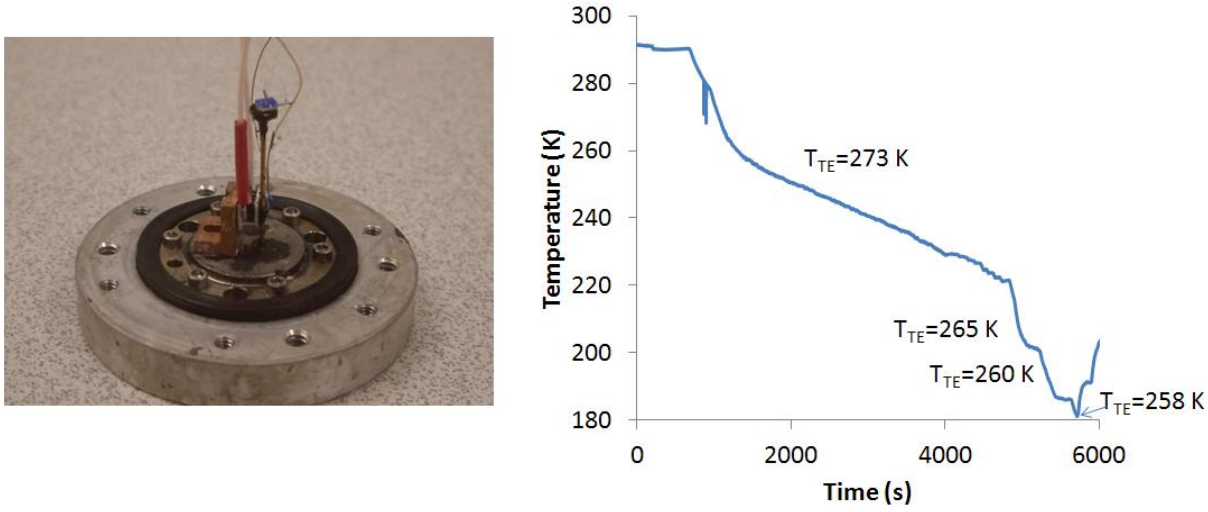

Figure 7.7: a) Photograph of an integrated TE-MCC. The fiber-based MCC used with thermoelectric pre-cooling is the same device used in Chapter 5.3.3 to measure specific cooling power of the refrigerant mixtures. b) Cool-down profile allowing a minimum stable temperature of 184 K, with TE pre-cooling to 260 K.

The specific cooling (Δh) power of the refrigerant mix is measured as a function of cold-tip temperature at 273 K to compare with results using the same device with ice pre-cooling. Heat is applied to the cold-tip to determine the net cooling power. After net cooling power is found, background heat loads at that pre-cooling temperature are found according to the method described in chapter 3.5.5. The resulting specific cooling powers are shown in Figure 7.7.

A second fiber-based TE-JT MCC was assembled with a larger J-T valve gap to allow a higher flow-rate. In this case the flow-rate was 30 sccm. The specific cooling power of the 200K Mix in this device was measured at a pre-cooling temperature of 273 K. Figure 7.7 compares the

specific cooling power of this high-flow-rate device with that of the low-flow-rate TE J-T MCC, and that of the same low-flow-rate MCC without the TE pre-cooler, and instead with pulsating flows. The lines in Figure 7.7 show calculated specific cooling powers. The solid line is (Δh) calculated according to $(\Delta h|_T)_{min}$, and the dashed line is (Δh) calculated for puling flow according to Equation 5.8. Recall that this line accurately predicted the results for the low-flow-rate MCC with pulsating low in Chapter 5.4.4. The dotted line is (Δh) calculated for refrigerant after complete liquid hold-up at room temperature. Recall that this line accurately predicted the composition of the mixtures in Chapter 4. Note that the specific cooling power of the low-flow-rate MCC lies between the two calculated lines. It appears that TE-pre-cooling of the microchannels increases the cooling power compared to pulsating flow, but does not fully recover the cooling power of the mixture. Furthermore, the high-flow-rate MCC has cooling power between that of the pulsating refrigerant and the held-up refrigerant.

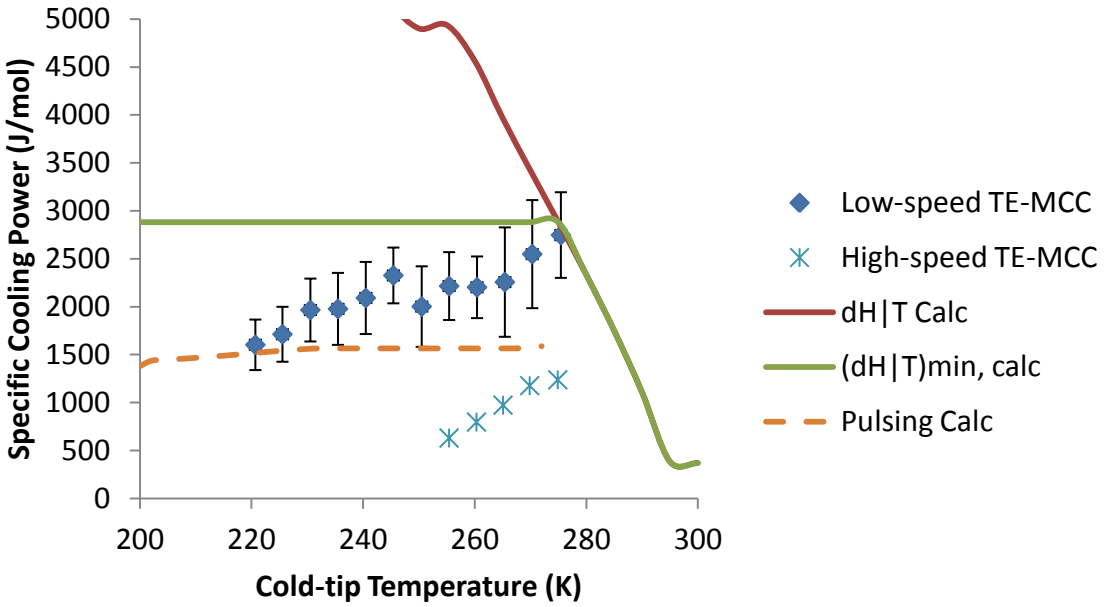

Figure 7.8: Specific cooling power measurement of the two MCCs assembled with integrated thermoelectric pre-cooling.

Further work with these devices will explore the cooling power as a function of pre-

cooling and find an optimal coefficient of performance. Further study of heat and mass transport of refrigerant mixtures in micro-channels and corresponding two-phase flow regimes is required to better understand the large difference in cooling powers of the same mixture in the two different thermoelectrically pre-cooled MCCs.

7.3.3: Study of Mixed Refrigerant Heat and Mass Transport in Micro-Channels

Heat and mass transport of mixed refrigerant in micro-channels must be better understood. Such better understanding can allow better heat exchanger design, better mixture designs for integrated pre-cooling, and a grasp of the VLL dynamics. One experiment to help this understanding involves a counter-flow heat exchanger (CFHX), in which cooled nitrogen is fed through one side, and warm mixed refrigerant is fed through the other, as in Figure 7.9. The nitrogen will chill the mixture, and the resulting 2-phase flow regime can be observed visually. The refrigerant exiting the micro-channel can be collected and its composition analyzed. In such a way, mass transport can be studied as a function of 2-phase flow pattern. Furthermore, measuring the change in Nitrogen temperature at a known Nitrogen flow-rate would give the enthalpy change of the refrigerant, from which the heat exchange parameter of the mixture can be measured. The refrigerant mixture can be designed to include a second liquid phase at the temperature range experienced within the CFHX, such that VLL dynamics can be observed, and VLL heat and mass transport can be measured.

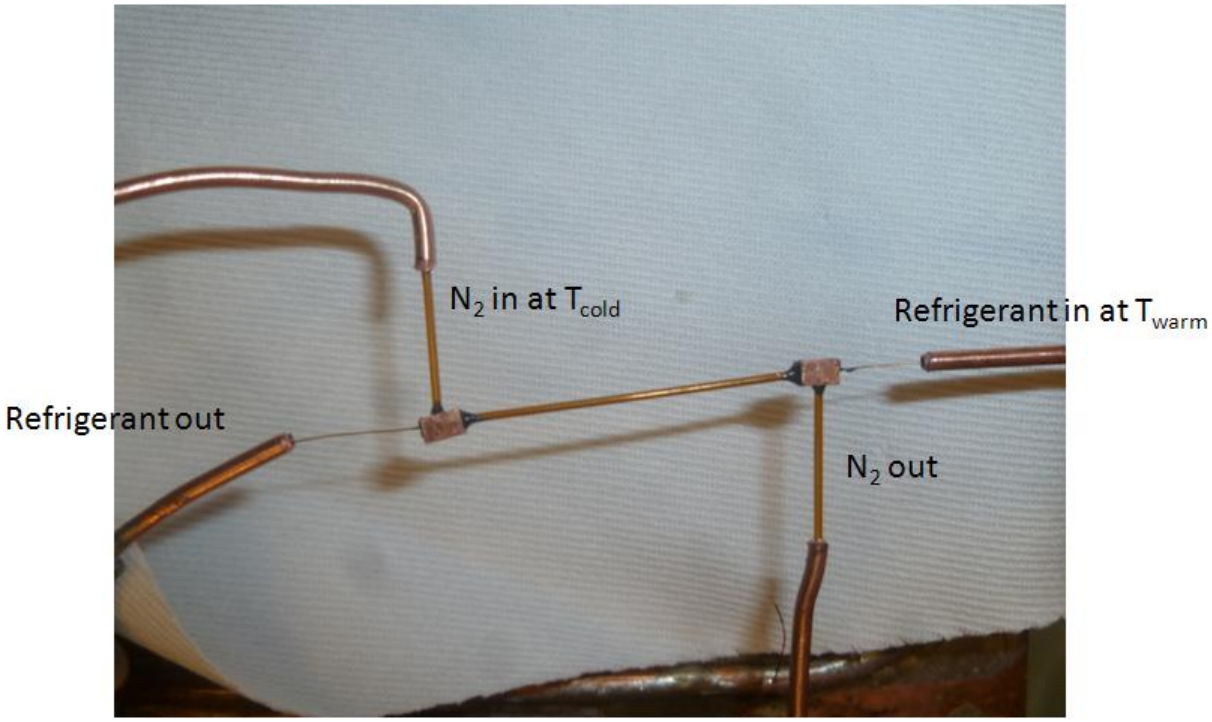

Figure 7.9: A test CFHX to measure heat and mass transport in micro-channels with mixed refrigerants.

7.3.5: Vapor Compression Cascade

The low cooling power with to steady flow and the time-varying cooling power with to pulsating flow are both due to changes in the refrigerant composition compared to the original mixture design. This can be avoided by using a pure-component refrigerant. As shown in Chapter 3.5.1 with isobutane, the mini-compressor and micro-cooler system make a very effective vapor-compression cooler, but the low-temperature is limited. The low-temperature can be reduced by adding a second cooler stage, with a second refrigerant that liquefies at the temperature of the 1st stage—in essence creating a vapor compression cascade cooler. With the micro compressor developed in Chapter 6, 20 stages can be integrated into a single device that is still small in scale, as in Figure 7.10a. The refrigerants in the first 7 stages are shown in Figure 7.10b. Sixteen stages can be used to cool to liquid hydrogen temperatures, and the remaining 4 stages can employ helium dilution to reach temperatures below 1 K, and be useful for such applications as quantum

computing [87].

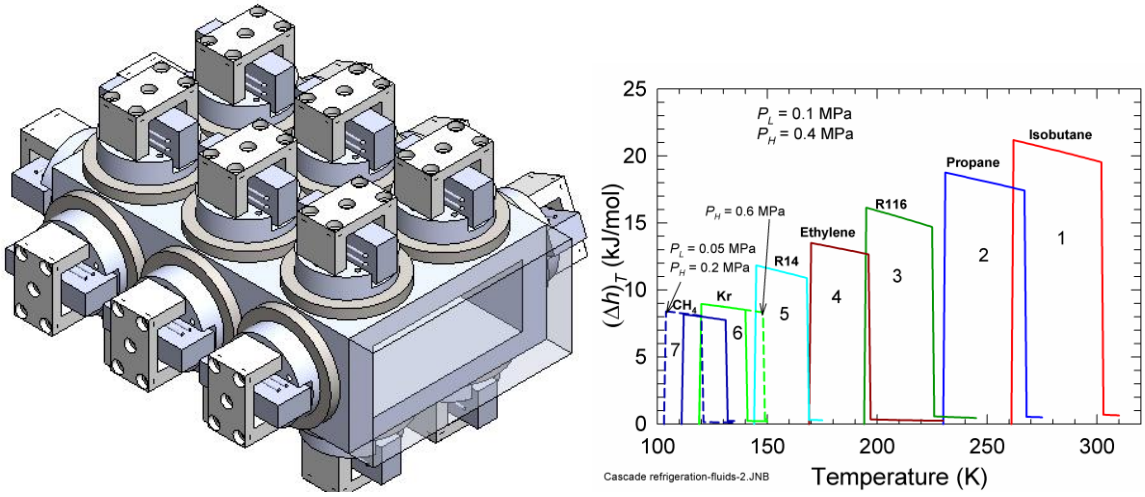

Figure 7.10: a) CAD drawing of a 20-stage vapor compression cascade, and b) isothermal enthalpy difference of the first 7 stages of the cascade.

REFERENCES

[1] R. Radebaough, “Cryocoolers: the state of the art and recent developments.”J. Phys. Condens. Mat. 21 (2009) 164219.

[2] JR Montague, KA Bertness NA Sandord, VM Bright, CT Rogers, “Capacitive readout technique for studies of dissipation in GaN nanowire mechanical resonators,” in Proceedings of the ASME 2011 International Mechanical Engineering Congress & Exposition (IMECE2011), November 11-17, 2011, Denver, Colorado, USA

[3] Y S. Song, SJ Moon, L Hulli, SK Hasan, E Kayaalp, and U Demirci, “Microfluidics for cryopreservation,” Lab Chip, 2009, 9, 1874–1881

[4] A.E. Mahdi, D.J. Mapps “High-*T* SQUIDs: the ultra sensitive sensors for non-destructive testing and biomagnetism,” Sens. Actuators A: Physical, 810367 (2000).

[5] P. H. Siegel, “Terahertz Technology” IEEE Transactions on Microwave Theory and Techniques, 50 (3) (2002), 910.

[6] Nature Physics 2, 794 - 796 (2006)

[7] See *The Engineer*, 1917; T. Finklestein, “Air engines,” *The Engineer* **207**, pp. 492-497, pp. 522-527,pp. 568-571, pp. 720-723, 1959.

[8] J. Herschel, *The Athenaeum*, 1834.

[9] Kirk, “On the mechanical production of cold, *Proc. Inst. Civil Eng. (London)* **37**, pp. 244-315, 1874.

[10] J. W. L. Köhler and C. O. Jonkers, “Fundamentals of the gas refrigeration machine,” *Philips Tech. Rev*. **16**(3), pp. 69-78, 1954; see also, “Construction of the gas refrigeration machine,” *Philips Tech. Rev*. **16**(5), pp. 105-115, 1954.

[11] R. Radebaugh, Fundamentals of alternate cooling, in G. Walker, *Cryocoolers part 2:*

Applications, Plenum Press, New York, pp. 129-175.

[12] R. Lewis, Y. Wang, J. Cooper, M.M. Lin, V.M. Bright, Y.C. Lee, P. Bradley, R. Radebaugh, and M. Huber, "Micro Cryogenic Coolers for IR Imaging," Infrared Technology and Applications XXXVII, Proc. of SPIE (2011).

[13] WA Little, "Heat transfer efficiency of Kleemenko cycle heat exchangers," Advances in Cryogenic Engieering: Transactions of the Cryogenic Engineering Conference—CEC 53 (2008) 606.

[14] N. Brauner, D. Moalem-Maron, Identification of the range of small diameter conduits, regarding two-phase flow pattern transition, Int. Comm. Heat Mass Transfer 19 (1992) 29-39.

[15] Garimella S, Killion JD, Coleman JW. An experimentally validated model for two-phase pressure drop in the intermittent flow regime for circular microchannels. ASME J. Fluids Eng. 2002; 124:205-15.

[16] Muhong Lin, "Fabrication, Assembly and Characterization of a Hollow-Core Fiber-Based Micro Cryogenic Cooler," PhD. Thesis, University of Colorado, Boulder, CO 2009.

[17] PW Bridgman, "Heat and Thermodynamics," in *Fundamental Formulas of Physics* D H Menzel (ed) Dover, New York, 1960.

[18] G. Venkatarathnam, *Cryogenic Mixed Refrigerant Processes*. The international Cryogenics Monograph Series, K.D. Timmerhaus, Carlo Rizzuto ed. Springer: New York, 2008.

[19] E. W. Lemmon, M. L. Huber, and M. O. McLinden, NIST Standard Reference Database 23: Reference Fluid Thermodynamic and Transport Properties-REFPROP, Version 9.0, National Institute of Standards and Technology, Standard Reference Data Program, Gaithersburg . 2010.

[20] R. Radebaugh, "Microscalse Heat Transfer at Low Temperatures," in *Microscale Heat Transfer -Fundamentals and Applications,* S. Kakac, *et al* (eds.), Springer, the Netherlands, 2005, pp. 93-124.

[21] Lin M-H, Bradley PE0, Wu H-J, Booth JC, Radebaugh R, Lee YC. Design, fabrication, and assembly of a hollow-core fiber-based micro cryogenic cooler. In: Solid-State Sensors, Actuators and Microsystems Conference, 2009. TRANSDUCERS 2009. International , Denver, Colorado, June 2009: 1114-7.

[22] WJ Podbielnak 1936 US Patent Specification 2,041,725

[23] WA Little, Proc. 5th Int. Conv. on Cryocoolers p 3.

[24] Radebaugh R., Recent Developments in Cryocoolers. 19th Int. Congress of Refrigeration, 1995; 973-89

[25] M.Q. Gong, E.C. Luo, J.F. Wu, Y. Zhou, "On the Temperature Distribution in the Counter Flow Heat Exchanger with Multicomponent Non-Azeotropic Mixtures," *Cryogenics,* Vol 42, 12, (2002) 795-804

[26] V. N. Alfeev, V. M. Yagodin, V. A. Nikol'skii (1972). Cooling articles to cryogenic temperatures. Soviet Union Patent 362,978

[27] W. A. Little, "Method for efficient counter-current heat exchange using optimized mixtures." U.S. Patent 5,644,502 (1997).

[28] A. Alexeev, H. Quack, "Refrigerant mixture for a mixture-throttling process." U.S. Patent 6,513,338 (2003).

[29] M. Gong, J. Wu, E Luo, Y Qi, Y Zhou, "Optimum Composition Calculation for Multicomponent Cryogenic Mixture used in Joule-Thomson Refrigerators." *Advaces in Cryogenic Engineering* 45 (2000), 283-290.

[30] F Dittus and L Boelter, Univ. Calf. (Berkeley) Publs. Eng. 2: 443 (1930).

[31] J Wu, M Shi, Y Chen, X Li, "Visualization study of steam condensation in wide rectangular silicon microchannels," Int. J. of Therm. Sci. 49 (2010) 922-930.

[32] Y Chen, R Wu, M Shi, J Wu, GP Peterson, "Visualization study of steam condensation in triangular microchannels," Int. J. of Heat and Mass Transfer 52 (2009) 5122-5129

[33] JC Chen, ASME paper 63-HT-34, National Heat Transfer Conference, Boston (1963)

[34] Lockhart, R.W., Martinelli, R.C.; Chem. Eng. Prog., Vol. 45. 1949, pp. 39–48

[35] G Nellis, C. Hughes, and J Pfotenhauser, "Heat transfer coefficient measurements for mixed gas working fluids at cryogenic temperatures" Cryogenics 45 (2005) 546-556

[36] MQ Gong, JF Wu, EC Luo YF Qi QG Hu and Y Zhou, "Research on the change of mixture compositions in mixed-refrigerant Joule-Thomson Cryocoolers," Advances in Cryogenic Engineering: Proceedings of the Cryogenic Engineering Conference, Vol 47 (2002) 881.

[37] MQ Gong, Z. Deng, J Wu, "Composition shift of a Mixed-gas Joule-Thomson Refrigerator driven by an Oil-Free Compressor," *Cryocoolers*, 14 (2007), pp. 453-458.

[38] N. Lakshmi Narasimhan, G. Venkatarathnam "A method for estimating the composition of the mixture to be charged to get the desired composition in circulation in a single stage JT refrigerator operating with mixtures" Cryogenics, 50 (2010), pp. 93–101

[39] W. A. Little "Microminerature refrigeration—Small is better." *Physica 109 & 110 B* (1982). 2001-2009

[40] S. Garvey, S. Logan, R. Rowe, and W.A. Little "Performance characteristics of a low-flow rate 25mW LN_2 Joule-Thompson refrigerator fabricated by photolithographic means." *Appl. Phys. Lett. (42)* 12. 1983.

[41] R. Paugh. “New class of microminerature Joule-Thompson refrigerator and vacuum package.” *Cryogenics 1990 Vol . 30.* 1079-83

[42] T. Ameel, I. Paputski, R. Warrington, R. S. Wagen, and M. K. Drost. “Miniaturization Technologies for advanced energy conversion and transfer systems.” *Journal of Propulsion and Power Vol 16*, No. 4 (2000). 577-582

[43] J. Burger, H. Holland, J. Seppenwoodle, E. Berenschot, H. ter Brake, J. Gardeniers, M. Elwenspoek, and H. Rogalla. “165K microcooler operating with a soprtion compressor and micromachined coldstage.” *Cryocoolers* 11, Dordrecht*/New York: Kluwer/Academic/Plenum* pg 551-60 (2001).

[44] J. Burger, H. Holland, E. Berenschot, J. Seppenwodde, M. Brake, J. Gardeniers and M. Elwenspoek. “165K microcooler operating with a soprtion compressor and micromachined coldstage.” *Proc. IEEE MEMS*, pp. 418-421, 2001.

[45] P.P.P.M. Lerou, T.T. Veenstra, J.F. Burger, H.J.M. ter Brake, H. Rogalla. “Optimization of counterflow heat exchanger geometry through minimization of entropy generation.” Cryogenics 45 (2005) 659–669.

[46] P. P. P. M. Lerou, H. J. M. ter Brake,H. J. Holland, J. F. Burger, and H. Rogalla, “Insight into clogging of micromachined cryogenic coolers,” *Appl. Phys. Lett.* **90**, 064102, (2007).

[47] M.-H. Lin, P. E. Bradley, M. L. Huber, R. Lewis, R. Radebaugh, Y. C. Lee, “Mixed refrigerants for a glass capillary micro cryogenic cooler.” *Cryogenics 50* (2010) 439-442.

[48] A Cozma and B Puers, “Characterization of the electrostatic bonding of silicon and Pyrex glass”, J. Micromech. Microeng. 5 (1995) 98-102

[49] JF Burger “Cryogenic Microcooling: A micromachined cold stage operating with a sorption compressor in a vapor compression cycle.” PhD. Thesis, University of Twente, Enschede,

The Netherlands, 2001.

[50] MJ Simon, "An analytical and numerical molde for a piezoelectric axially driven membrane microcompressor for optimum scaled down design," PhD. Thesis, University of Colorado, Boulder CO, 2011.

[51] R. Rapp, W.K. Schomburg, D. Maas, J. Schulz, W. Stark, LIGA micropump for gases and liquids, Sensors and Actuators A: Physical 119 (2005) 245-253.

[52] R. Linnemann, P. Woias, C.-D. Senfft, J.A. Ditterich, A self-priming and bubble tolerant silicon micro pump for liquids and gasses, Proceedings of the IEEE Micro Electro Mechanical Systems (1998) 532-537.

[53] Yoon, J. S., Choi, J. W., & Kim, M. S., Computational and Experimental Investigation on the Performance Characteristics of the Micro Gas Compressor, Microelectronic Engineering 86 (2009) 1975-1982.

[54] FLIR Commercial Visions Systems, Inc. http://www.flir.com/cvs/cores/view/?id=51942

[55] Lewis RJ, Lin M-H, Wang Y, Cooper J, Bradley P, Radebaugh R, Huber M, Lee YC. "Demonstration of a micro cryogenic cooler and miniature compressor for cooling to 200 K." In: Proceedings of the international mechanical engineering conference and exposition, Denver, Colorado, November; 2011; 63908

[56] M.N. Srinivas, C. Padmanabhan, "Computationally efficient model for refrigeration compressor gas dynamics," *International Journal of Refrigeration 25* (2002) 1083-1092.

[57] I. Garaway, M. Lewis, P. Bradley, R. Radebaugh, "Measured and Calculated Performance of a High Frequency, 4 K Stage, He-3 Regenerator." *Cryocoolers 16* (2011), pp. 405-410

[58] B. S. Field, "Visualization of Two-Phase Refrigerant and Refrigerant-Oil Flow in a Microchannel," *Proceedings of IMECE2007*, IMECE2007-43471, (2007)

[59] RJ Lewis, Y-D Wang, M-H Lin, ML Huber, R Radebaugh, YC Lee, "Enthalpy Change Measurements of a Mixed Refrigerant in a Micro Cryogenic Cooler in Steady and Pulsating Flow Regimes" *Cryogenics 52* (2012) 609-614

[60] RB Bird, WE Stewart, EN Lightfoot, *Thrasport Phenomena,* second etition. John Wiley and Sons, 2007.

[61] See for example Equation 11 from Thierry C, Tancogne S. Stability of bifluidic jets in microchannels Eur. J. Mech B-Fluid 2011; 30(4): 406-420.

[62] See for example Equation 18.24 in ZS Spakovszky, "Unified: Therodynamics and Propulsion,"
http://web.mit.edu/16.unified/www/FALL/thermodynamics/notes/node131.html

[63] Cussler, E. L. (1997). *Diffusion: Mass Transfer in Fluid Systems* (2nd ed.). New York: Cambridge University Press.

[64] Bonney, G.E. and Longsworth, R.C., "Considerations in using Joule-Thomson cryocoolers", Proceedings of the 6th International Cryocoolers Conference, Vol. 1, pp. 231–244, Plymouth, Massachusetts, (October 25–26, 1990), published by David Taylor Research Center as DTRC-91/002, January 1991.

[65] B.Z. Maytal, J.M. Pfotenhauer, "Transient Behavior," *Miniature Joule-Thomson Cryocooling*, 259-274. The international Cryogenics Monograph Series, Springer: New York, 2013.

[66] www.empactanalytical.com

[67] NIST Standard Reference Database 4. NIST Thermophysical Properties of Hydrocarbon Mixtures (SuperTrapp): Version 3.2, National Institute of Standards and Technology, Gaithersburg, MD; 2007.

[68] J W Coleman, S Garimella, Proc. Of the 34th National heat Transfer Conference, NHC2000-12115, ASME Heat Transfer Division HTD 366-4 (2000), 71.

[69] P Cheng, G Wang, X Quan, "Recent work on boiling and condensation in microchannels," Journal of Heat Transfer (2009) 043211

[70] A. Bhushan, D. Yemane, E. B. Overton, J. Goettert, M. C. Murphy, Faprication and preliminary results for LiGA fabricated nickel micro gas chromatograph columns, J. Microelect. Mech. Syst. 16 (2007) 383-393.

[71] A. A. Astle, H. S. Kim, L. P. Bernal, K. Najafi, P. D. Washabaugh, Theoretical and Experimental performance of a high-frequency gas micropump. Sensors and Actuators A: Physical 134 (2007) 245-256.

[72] J. Vican, B. F. Gajdeczko, F. L. Dryer, D. L. Milius, I. A. Aksay, R. A. Yetter, Development of a microreactor as a thermal source for microelectromechanical systems power generation, Proc. Combustion Institute 29 (2002) 909-916.

[73] G.Q. Lu, C.Y. Wang , T.J. Yen , X. Zhang, Development and characterization of a silicon-based micro direct methanol fuel cell, Electrochimica Acta 49 (2004) 821–828.

[74] S.-C. Yao, X. Tang, C.-C. Hsieh, Y. Alyousef, M. Vladimer, G. K. Fedder, C. H. Amon, Micro-electro-mechanical systems (MEMS)-based micro-scale direct methanol fuel cell development, Energy 31 (2006) 636–649

[75] J. D. Heppner, D. C. Walther, A. P. Pisano, The design of ARCTIC: A rotary compressor thermally insulated μcooler, Sensors and Actuators A: Physical 134 (2007) 47–56

[76] S. Jeong, How difficult is it to make a micro refrigerator, Int. J. Refrigeration 27, 3 (2004) 309-313

[77] W. A. Little, Microminiature refrigeration, Rev. Sci. Instrum., 55 (5), (1984).

[78] J. F. Burger, H. J. Holland, H. J. M. ter Brake, and H. Rogalla, “Construction and operation of a 165 K Microcooler with a sorption compressor and micromachined cold stage.” Cryocoolers 12 (2003) 643-649.

[79] P. P. P. M. Lerou, G. C. F. Venhorst, C. F. Berends, T. T. Veenstra, M. Blom, J. F. Burger, H. J. M. ter Brake and H. Rogalla. Fabrication of micro cryogenic coldstage using MEMS technology, J. Micromech. Microeng. 16 (2006) 1919-1925.

[80] R. Rapp, W.K. Schomburg, D. Maas, J. Schulz, W. Stark, LIGA micropump for gases and liquids, Sensors and Actuators A: Physical 119 (2005) 245-253.

[81] Jan. G. Smits, Piezoelectric micropump with 3 valves working peristaltically, Sensors and Actuators A: Physical 21 (1990) 203-206.

[82] D.S. Lee, J.S. Ko, Y.T. Kim, Bidirectional pumping properties of a peristaltic piezoelectric micropump with simple design and chemical resistance, Thin Solid Films 468 (2004) 285-290.

[83] M.N. Srinivas, C. Padmanabhan, Computationally efficient model for refrigeration compressor gas dynamics, Int. J. Refrigeration 25 (2002) 1083-1092.

[84] J. C.-H. Lin, F. Yu, and Y.-C. Tai, Cracking pressure control of parylene checkvalve using slanted tensile tethers, 2010 IEEE 23rd International Conference on Micro Electro Mechanical Systems (MEMS), vol. 2, no. 1, (2010) 1107-1110

[85] A. M. Cardenas-Valencia, J. Dlutowski, J. Bumgarner, C. Munoz, W. Wang, R. Popuri, L. Langebrake, Development of various designs of low-power, MEMS valves for fluidic applications, Sensors and Actuators A: Physical 136 (2007) 374-384.

[86] PE Bradley, R Radebaugh, RJ Lewis, M-H Lin, and YC Lee, “Temperature instability comparison of micro-and mesoscale Joule-Thomson Cryocoolers employing mixed

refrigerants," *Advances in Cryogenic Engineering*, AIP Conf. Proc. 1434, 690-697 (2012)

[87] "Cryogenics, Input/ Output, and Shielding" D Wave, *Deep Dive Document Series,* http://www.dwavesys.com/en/deep-dive.html

Appendix A: Analysis of the equality of $\Delta h|_{\iota}$ and $(\Delta h|_{T})_{\min}$ in an ideal heat exchanger.

Consider an ideal heat exchanger in which warm fluid enters at the warm-end, and cold fluid enters the cold-end. In an idea heat exchanger, the cold fluid will cool the hot fluid down such that at some point the temperatures will be equal. For the hot stream to become colder than the cold stream in this heat exchanger would require heat to spontaneously flow against a temperature gradient, in violation on the Clausius interpretation of the 2nd law of thermodynamics.

In this analysis, the enthalpy of the hot stream (h_h) or cold stream (h_c) will both be monotonic functions of temperature. That is to say $h_{c,h}(T)=Cp_{h,c}T$, where Cp is some positive constant-pressure specific heat. Consider a general heat exchanger with a hot-end temperature of T_{max} and a cold-end temperature of T_{min}, where the isothermal enthalpy difference between the hot and cold streams at T_0 is:

$$\Delta h|_T(T_0)=h_c(T_0)-h_h(T_0)$$

and has a minimum at a temperature T_0 (see Figure A.1) .

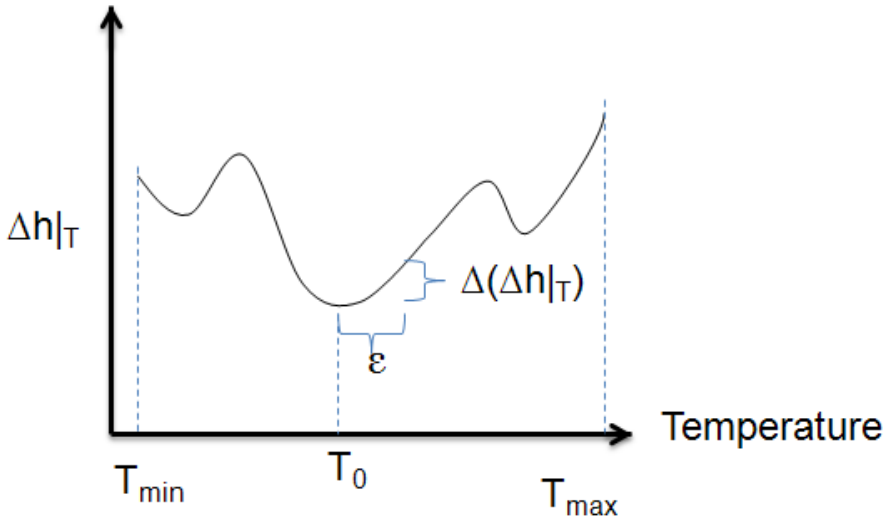

Figure A.1: General $\Delta h|_T$ curve between a hot fluid and cold fluid in a heat exchanger. The value

$\Delta h|_T$ is at a minimum at $T=T_0$, and the difference between $\Delta h|_T(T_0+\varepsilon)$ and $\Delta h|_T(T_0)$ is termed $\Delta(\Delta h|_T)$.

Now consider some temperature value ε, such that $T_{min}<T_0+\varepsilon<T_{max}$. At $T_0+\varepsilon$, isothermal enthalpy difference $\Delta h|_T(T_0+\varepsilon)$ will be larger than $\Delta h|_T(T_0)$. Call this difference:

$$\Delta(\Delta h|_T) \equiv \Delta h|_T(T_0+\varepsilon) - \Delta h|_T(T_0) > 0.$$

for all non-zero ε. As has been shown in Chapter 2.3.2, the difference between the enthalpy of the hot stream and the cold stream will be constant at all locations: $\Delta h|_l = const$. Consider a case where the iso-spatial enthalpy difference and the isothermal enthalpy difference coincide at some temperature other than T_0, in essence at a temperature $T_0+\varepsilon$:

$$\begin{aligned}\Delta h|_l &= \Delta h|_T(T_0+\varepsilon)\\ &= \Delta h|_T(T_0) + \Delta(\Delta h|_T)\\ &= h_c(T_0) - h_h(T_0) + \Delta(\Delta h|_T).\end{aligned}$$

We can move along the heat exchanger to a new location where the cold stream is at T_0. The hot stream will be at some new temperature T_h, and the iso-spatial enthalpy remains the same:

$$h_c(T_0) - h_h(T_h) = \Delta h|_l = h_c(T_0) - h_h(T_0) + \Delta(\Delta h|_T)$$

or

$$h_h(T_h) = h_h(T_0) - \Delta(\Delta h|_T)$$

Because $\Delta(\Delta h|_T)$ is strictly positive, $h_h(T_h)<h_h(T_0)$, and because h_h is monotonic with T, $T_h<T_0$. But where the hot stream is at T_h, the cold stream is at T_0, and this corresponds to a point where the hot stream is colder than the low stream, which violates the 2nd law of thermodynamics. The way to resolve this violation is if $\Delta(\Delta h|_T) = 0$, which occurs when ε=0, and $\Delta h|_l = \Delta h|_T(T_0) = (\Delta h|_T)_{\min}$.

Appendix B: Development of a model of charging time.

This model covers the slow increase in high-pressure in the high-pressure channels of the MCC test set-up, by considering a conservation of mass in both the high-pressure and low-pressure channels.

The pressure in the high-pressure channels is a function of the number of vapor-phase moles in the high-pressure channels ($n_{hi,v}$) and their compressibility (Z_{vap}). In this analysis, the volume occupied by the vapor in the high-pressure channels is considered constant (V_{hi}). Although some of the volume will be occupied by liquid, that volume is negligible in this analysis. The high pressure is given by:

$$P_{hi}(t) = n_{hi,v}(t) \cdot \frac{RT}{V_{hi}} Z_{vap}(t) \qquad (B.1)$$

where R is the ideal gas constant (0.082057 L-atm/mol-K), T the high-pressure temperature (295 K), and *t* time. The compressibility Z_{vap} is a function of the vapor composition in the high-pressure channels, which are determined by the high pressure. Thus $Z_{vap}=f(P_{hi})$. For the "200K mix", this function is linear in the pressure range of interest: $Z_{vap}=0.9831-0.0805(\text{bar}^{-1})P_{hi}$. The number of vapor-phase moles in the high-pressure channels varies with time according to a conservation of mass:

$$\frac{dn_{hi,v}}{dt} = \dot{n}_{compr} - \dot{n}_{liq} - \dot{n}_{MCC} \qquad (B.2)$$

where $\dot{n}_{compr}$ is the flow-rate through the compressor, $\dot{n}_{liq}$ the liquefaction rate, and $\dot{n}_{MCC}$ the flow-rate through the MCC. The flow-rate through the MCC is roughly linear with pressure drop across it:

$$\dot{n}_{MCC} = \alpha(P_{hi}(t) - P_{low}), \qquad (B.3)$$

where the constant α is characteristic of the particular MCC under question, and can vary from

0.7 μmol/bar (3 sccm at 3:1 pressure), to 23 μmol/bar (100 sccm at 4:1 pressure). The flow-rate through the compressor is a function of both a function of the pressure across the compressor, and the compressibility of the refrigerant. When compressing an ideal gas, the compressor flow-rate is roughly linear between zero-flow at a high-pressure of 6.19 bar, and a maximum flow of 497 sccm at 1 bar of high pressure. With a non-idea gas, a compression reduction factor (ZZ) is introduced that reduces the pressure generated at a given flow-rate. The flow-rate through the compressor is then given by:

$$\dot{n}_{compr} = -95.7\left(\frac{sccm}{bar}\right)\frac{P_{hi} - P_{low}}{ZZ} + 497sccm \qquad (B.4)$$

The compression reduction factor is a function of the low-pressure gas composition ($x_{i,low}$). In particular, in terms of the pentane concentration ($x_{5,low}$), it is modeled in the first order as:

$$ZZ\text{=-}1.5342\ x_{5,low}\text{+}1.0367, \qquad (B.5)$$

which is a fit of the maximum pentane concentration 28 % giving 3.37 bar at 0 sccm flow, and the minimum pentane concentration 8.4 % for which no liquid forms at the high-pressure side at 6.19 bar.

The rate of liquefaction will be the product of the flow-rate through the compressor and the liquid fraction (X_l) of the mix that is exiting the compressor. The composition of the mix that exits the compressor will be the low-pressure gas composition ($x_{i,low}$), and the liquid fraction of that mix can be found by imposing vapor-liquid equilibrium at the high pressure, (for example with REFPROP). The rate of liquefaction will then be:

$$\dot{n}_{liq} = \dot{n}_{compr} \cdot X_l\left(P_{hi}, x_{i,low}\right) \qquad (B.6)$$

Note that $X_l\left(P_{hi}, x_{i,low}\right)$ denotes that X_l is a function of the high pressure and low-side composition. The composition of the low-pressure will vary over time as original mix is fed

through the charging line (connecting to a low-pressure supply bottle regulated at 0.100 MPa), and vapor is fed from the MCC, and both combine with what is already in the low-pressure lines. The time-evolution of the composition of the ith gas component in the low-pressure line ($x_{i,low}$) is given by:

$$\frac{d}{dt}\left(x_{i,low}\right) = \frac{1}{n_l}\left(x_{i,vap,hi} \cdot \dot{n}_{MCC} + x_{i,feed} \cdot \dot{n}_{feed} - x_{i,low}\dot{n}_{compr}\right). \qquad (B.7)$$

Here $x_{i,vap,hi}$ is the molar fraction of the ith vapor component in the high side, which can be determined by imposing VLE at the high pressure: $x_{i,vap,hi}=f(P_{hi})$. The functionality of f can be determined for example by REFPROP. Here $x_{i,feed}$ is the molar fraction of the ith component of the original mix, as fed through the charging line, and $\dot{n}_{feed}$is the molar flow-rate through the charging line into the low-pressure volume. The low-pressure volume is maintained at 0.1 MPa, and the compressibility of the gas in the low-pressure volume does not change appreciably at that pressure when the composition changes, so the number of moles in the low-pressure volume can be considered constant. Then a conservation of mass gives

$$\dot{n}_{feed} = \dot{n}_{compr} - \dot{n}_{MCC}. \qquad (B.8)$$

Equations B1-B8 form a closed set of coupled, 1st order, nonlinear differential equations which can be integrated with time, starting with an initial composition given by the original mixture, and an initial high-side pressure of 0.1 MPa. A MATLAB code to do such integration is listed as follows:

```
%%%%%%%%%%%%%%%%%%%%%%%%%%%%%%%%%%%%%%%%%%%%%%%%%%%%%%%%%%%%%%%%%%%%%%%%%%%%
%%%% Model of "charging time" of MCC's, based on conservation of mass %%%%%
%%%% (moles) in the high- and low-pressure channels.                  %%%%%
%%%%                                                                  %%%%%
%%%% A number of simplifying assumptions and correlations have been   %%%%%
%%%% made in order to speed up the code. The results should be con-   %%%%%
%%%% sidered as a rough analysis, rather than a high accuracy pre-    %%%%%
%%%% diction.                                                         %%%%%
%%%%                                                                  %%%%%
%%%% (c) R. Lewis, 2012                                               %%%%%
%%%%%%%%%%%%%%%%%%%%%%%%%%%%%%%%%%%%%%%%%%%%%%%%%%%%%%%%%%%%%%%%%%%%%%%%%%%%


V_h=20000;%15*pi*1^2+5*.5^2*pi; %mm^3=uL. V=pi*r^2*h for a cylinder
%V_h=100*V_h;
V_l=1*V_h; % Low pressure volue. We'll say it's the same for now.
d_h=1; %mm. Minimum hydraulic diameter in coupling lines


dt=V_h/10000; %s -- want to make sure it's small enough
t=0:dt:V_h/5; %run for some time
nt=numel(t);
P_h=2+0*t; %pre-allocate P_h (high-side pressure), start at 2 atm
P_l=1; %atm
x_f=[.08 .46 .14 .04 .28]'; %feed molar composition of C1-C5 alkanes
x_h=x_f; %high-side composition.
x_l=x_f; %low-side composition
RT=295*0.082057; %L-atm/mol-K
Mix=ones(5,numel(t)); %pre-allocating vector which shows low-side composition vs time
n_lh=0; %moles of liquid in high-side
LiqF=0; LiqF_=ones(1,nt);


n_l=P_l*V_l/RT*1e-6; %atm*uL/(L-atm/mol-K * K)*1e-6
n_h=P_h(1)*V_h/RT*1e-6;


mwc1=refpropm('M','T',300,'P',100,'methane.fld');
mwc2=refpropm('M','T',300,'P',100,'ethane.fld');
mwc3=refpropm('M','T',300,'P',100,'propane.fld');
mwc4=refpropm('M','T',300,'P',100,'butane.fld');
mwc5=refpropm('M','T',300,'P',100,'pentane.fld');
MW=[mwc1,mwc2,mwc3,mwc4,mwc5]'; % array of component Molecular weight
MWt=MW'*x_f; %Total molecular weight
x=x_f.*MW/MWt; %mass fractions


A=[ -292860     0 8.2445    -0.8951 59.8465 0
    -687248.25  0 7.90694   -0.88600 49.02654 0
    -970688.5625 0 7.15059  -0.76984 0 6.90224
    -1280557    0 7.94986   -0.96455 0 0
    -1524891    0 7.33129   -0.89143 0 0]; %DePriester coefficients for C1-
%C5. From Wankat [1]


a=69.5673+22.595*exp(0.2586*d_h); b=-59.9899+176.8137*exp(0.3826*d_h);
%Garimella a and b coefficients [2];
L_crit=1;


k=1;
for k=1:nt %while k<nt && LiqF<L_crit
    if P_h(k)<2.1
        ZZ=1;
    else
        ZZ=-1.5342*x_l(5)+1.0367;
        %compression reduction factor, as a function of pentane
        %concentration at inlet
    end
    n_comp=(-95.714*(P_h(k)-P_l)/ZZ+497.14)/22400/60;
    %(mL/min)*(1mol/22400mL)*(1min/60s)=mol/s
    n_JT=(6)/4*(P_h(k)-P_l)/22400/60;
%mol/s--the value in first parenthesis is the 4:1 flow in sccm
    n_feed=n_comp-n_JT; % conservation of mass on low side dictates feed flowrate, mol/s
```

```
    Z_vap=-0.0805*P_h(k)+.9831;
%compressibility of high-side vapor as a function of high-pressure

%     MWt=MW'*x_l; %Total molecular weight of mix going through compressor
%     x=x_l.*MW/MWt; %mass fractions
%     Q=refpropm('Q','T',295,'P',P_h(k),'methane','ethane','propane','butane','pentane',x');
%     %quality of compressor outlet. Given in mass. will need it in moles
%     %is also super slow, so commented out for speed. Instead use Rachford-Rice [1]
    K=exp(A(:,1)/295^2+A(:,2)/295+A(:,3)+A(:,4)*log(P_h(k))+A(:,5)/P_h(k)+A(:,6)/P_h(k)^2);
    %DePreister correlation for Vapor-Liquid equilibrium constants of C1-C5 [1]
    q=(K.*x_l./x_h-1)./(K-1); q(isnan(q))=1; %form Rachford Rice Eqn for vapor fraction
    Q=sum(q)/5; %average over 5 quantities that should be the same.
    Q(Q>1)=1; Q(isnan(Q))=1; %maximum quality that makes sense, also remove NaNs


    n_cond=n_comp*(1-Q)*3;
    %(1-Q) of what came out of the compressor last time gets. The 3 is a
    %correction factor, found by trial-and-error to make the actual liquid
    %condensation agree to what REFPROP predicts, once the system has
    %equalized.
    n_lh=n_lh+n_cond*dt; %mol in liquid phase currently in high-side phase
    LiqF=n_lh/(n_lh+n_h); %mol fraction of above
    LiqF_(k)=LiqF;


    n_h=n_h + (n_comp - n_JT - n_cond)*dt;
    P_h(k+1)=RT/(V_h*1e-6)*Z_vap*n_h;


    %[y x_h]=refpropm('X','T',295,'P',P_h(k),'methane','ethane','propane','butane','pentane',x');
    %comment the above out to increase speed


    x_h=[(-0.0809*(P_h(k)/10)^2+0.1484*(P_h(k)/10)+0.0549)
        (-0.5916*(P_h(k)/10)^2+0.8385*(P_h(k)/10)+0.324)
        (-0.2089*(P_h(k)/10)^2+0.2071*(P_h(k)/10)+0.1103)
        (0.0012372*(P_h(k)/10)^2-0.03587*(P_h(k)/10)+0.0484678)
        (0.8801*(P_h(k)/10)^2-1.1582*(P_h(k)/10)+0.462)];
    %Composition of vapor in high-side, based on correlation from REFPROP
    %data . . . for general script, will want to calculate these
    %coefficients from REFPROP beforehand.
    x_h=x_h/(sum(x_h)); %just in case correlations are off and x_h above does not add to 1


    x_l=x_l+ (x_h*n_JT + x_f*n_feed - x_l*n_comp)*dt/n_l;% new composition of low-side
    Mix(:,k)=x_l;
    %ASSUMING instantaneous and homogenous mixing of vapor phase


    G=(n_JT*(MW'*x_h)/1000) / (pi*(d_h/1000)^2/4); %mass flux through thin portion of high-side
    L_crit=1-(a/(G+b));


    %k=k+1;
end
%[1] P. C. Wankat, Separation Process Engineering: Includes Mass Transfer
%Analysis (3rd Edition), August 10, 2011 | ISBN-10: 0131382276 | ISBN-13:
%978-0131382275,
%[2] J W Coleman, S Garimella, Proc. Of the 34th National heat Transfer
%Conference, NHC2000-12115, ASME Heat Transfer Division HTD 366-4 (2000),
```

Appendix C: Papers and Presentations based on this work

Published journal or conference papers:

1. **Ryan Lewis,** Yunda Wang, Mu-Hong Lin, Marcia L. Huber, Ray Radebaugh, Y.C. Lee, "Enthalpy Change Measurements of a Mixed Refrigerant in a Micro Cryogenic Cooler in Steady and Pulsating Flow Regimes" Cryogenics 52, 609-614 (2012).
2. **Ryan Lewis,** Collin Coolidge, Paul Schroder, Y.C. Lee, Victor Bright, "Fabrication, assembly, and testing of a MEMS-enabled micro gas compressor for a 4:1 pressure ratio," Sensors and Actuators A: Physicsal, in press
3. **Ryan Lewis,** Hayley Schneider, Yunda Wang, Ray Radebaugh, Y.C. Lee, "Two-phase Flow Patterns and Cooling Power of Mixed Refrigerant in Micro Cryogenic Coolers" ASME ICNMM2012, July 2012.
4. **Ryan Lewis,** Yunda Wang, Jill Cooper, M.-H Lin., Victor Bright, Y.C. Lee, Peter Bradley, Ray Radebauth, and Marcia Huber "Micro Cryogenic Coolers for IR Imaging", SPIE 2011., 2011, pp 8012-75
5. **Ryan Lewis,** M.-H. Lin, Jill Cooper, Yunda Wang, Marcia Huber, Peter Bradley, Ray Radebaugh and Y.C. Lee "Demonstration of an Integrated Micro Cryogenic Cooler and Miniature Compressor for Cooling to 200K," Proc. IMECE2011, Denver, CO, Nov. 11-17, 2011.
6. Yunda Wang, **Ryan Lewis,** M.-H. Lin, Ray Radebaugh and Y.C. Lee "Wafer-level Processing for Polymer –based Planar Micro Cryogenic Coolers", Proc. of IEEE MEMS'12, Paris, France, Jan. 29 - Feb. 2, 2012 pp.341-344

7. Yunda Wang, **Ryan Lewis**, M.-H. Lin, Ray Radebaugh Peter Bradley and Y.C. Lee "A Monolithic Polyimide Micro Heat Exchanger with a Suspended 3D Parallel Channels Structure for Cryogenic Application," Proc. IMECE2011, Denver, CO, Nov. 11-17, 2011.
8. P. Bradley, R. Radebaugh, **R.J. Lewis,** M.-H. Lin, and Y.C. Lee, "Temperature instability comparison of micro- and meso-scale Joule-Thomson cryocoolers employing mixed refrigerants." Presented at: *CEC/ICMC 2011*, Spokane, WA (June 14, 2011).
9. Lin, M.-H., Bradley, P.E., Huber, M.L., **Lewis, R.,** Radebaugh, R., Lee, Y.C., "Mixed refrigerants for a glass capillary micro cryogenic cooler," Cryogenics 50, 439–442 (2010).

Papers under review:

10. **Ryan Lewis**, Yunda Wang, Peter E. Bradley, Marcia L. Huber, Ray Radebaugh, Y.C. Lee, "Experimental Investigation of Low-pressure Refrigerant Mixtures for Micro Cryogenic Coolers" Submitted to Cryogenics, October 2012
11. **Ryan Lewis,** M.-H. Lin, Jill Cooper, Yunda Wang, Marcia Huber, Peter Bradley, Ray Radebaugh and Y.C. Lee "Demonstration of an Integrated Micro Cryogenic Cooler and Miniature Compressor for Cooling to 200K," Accepted at Journal of Thermal Science and Engineering Applications, Sept 2012.
12. **Ryan Lewis,** Yunda Wang, Ray Radebaugh, Marcia L. Huber, "Study of Mixed Refrigerant Undergoing Pulsating Flow in Micro Coolers with Pre-cooling," being prepared for Cryogenics, October 2012.
13. Yunda Wang, **Ryan Lewis**, M.-H. Lin, Ray Radebaugh and Y.C. Lee "The Development of Polymer-Based Planar Micro Cryogenic Coolers" Accepted to IEEE/ASME J. of MEMS, 2012

14. Yunda Wang, **Ryan Lewis,** M.-H. Lin, Ray Radebaugh and Y.C. Lee "Design and fabrication of All-Polymer Planar Micro Cryogenic Coolers" Submitted to for IEEE/ASME J. of MEMS, 2012